Hydrodynamics of indirect excitons in coupled quantum wells

Joe Wilkes

A Thesis submitted to
Cardiff University
for the degree of
Doctor of Philosophy

September 2012

Declaration: This work has not been submitted in substance for any other degree or award at this or any other university or place of learning, nor is being submitted concurrently in candidature for any degree or other award.

Signed: _____
Candidate

Date: _____

Statement 1: This thesis is being submitted in partial fulfillment of the requirements for the degree of Doctor of Philosophy.

Signed: _____
Candidate

Date: _____

Statement 2: This thesis is the result of my own independent work/ investigation, except where otherwise stated. Other sources are acknowledged by explicit references. The views expressed are my own.

Signed: _____
Candidate

Date: _____

Statement 3: I hereby give consent for my thesis, if accepted, to be available for photocopying and for inter-library loan, and for the title and summary to be made available to outside organisations.

Signed: _____
Candidate

Date: _____

In memory of Prof Alexei Ivanov.

Acknowledgments

I wish to express my gratitude to my supervisor, Dr Egor Muljarov, for all the guidance, kind patience and support I have received from him during my studies. Also, throughout my undergraduate years and in the beginning of my PhD, I had the honour and privilege of being taught by Prof Alexei Ivanov who is sadly no longer with us. This thesis, therefore, is dedicated to his memory which will undoubtedly continue to inspire all those who knew him.

I am very grateful for collaborations with Prof Leonid Butov and his group at the University of California at San Diego. I am thankful to his past and present students Dr Aaron Hammack, Dr Alex Winbow, Jason Leonard and Yuliya Kuznetsova who I have enjoyed the pleasure of working with. Much of the work presented in this thesis is the fruition of this collaboration.

I also would like to express my gratitude to Dr Leonidas Mouchliadis for numerous enlightening discussions and in particular for his guidance at the start of my PhD. Many thanks to my office mates, Rhys, Joanna, Kanchana and Mark.

Finally, I would like to thank my family, friends and band mates in Tidal. Most of all, thanks to my wife Marie, for her constant encouragement and support over the last four years.

Abstract

This thesis comprises a theoretical study of the dynamics of indirect excitons in coupled quantum wells at low lattice temperatures. The results of numerical simulations of the exciton photoluminescence pattern are presented and compared to available experimental data.

The in-plane transport of quantum well excitons created by laser excitation is modeled using a non-linear drift-diffusion equation. Combined with a model of exciton relaxation thermodynamics, a complete description of the evolution of the exciton density and temperature is built. The optical decay of indirect excitons is included in the modeling. This is used to make predictions of the spatial photoluminescence patterns which have been observed experimentally.

The transport of dipole orientated excitons via externally applied electrostatic potentials is also studied. The drift-diffusion equation is adapted to include the in-plane electric field. This is done for some specific forms of the potential landscapes such as a linear potential energy gradient and a propagating lattice. These correspond to some recent experiments for which results are available. The combined theoretical and experimental studies reveal a deeper insight into the transport properties of indirect excitons.

Finally, the external ring structure in the indirect exciton emission pattern is studied. Its formation is modeled using a set of coupled transport equations for electrons, holes and indirect excitons. The Coulomb interactions between all three species are incorporated in the model. It is shown that these interactions lead to an instability in the external ring and are responsible for its fragmentation into a periodic array of islands which has been observed experimentally.

Publications

J. Wilkes, E. A. Muljarov and A. L. Ivanov. Drift-diffusion model of the fragmentation of the external ring structure in the photoluminescence pattern of indirect excitons in coupled quantum wells. Phys. Rev. Lett. **109**, 187402 (2012).

J. R. Leonard, M. Remeika, Y. Y. Kuznetsova, A. A. High, L. V. Butov, J. Wilkes, M. Hanson, and A. C. Gossard. Transport of indirect excitons in a potential energy gradient. Appl. Phys. Lett. **100**, 231106 (2012).

Y. Y. Kuznetsova, J. R. Leonard, L. V. Butov, J. Wilkes, E. A. Muljarov, K. L. Campman and A. C. Gossard. Excitation energy dependence of the exciton inner ring. Phys. Rev. B **85**, 165452 (2012).

A. G. Winbow, J. R. Leonard, M. Remeika, Y. Y. Kuznetsova, A. A. High, A. T. Hammack, L. V. Butov, J. Wilkes, A. A. Guenther, A. L. Ivanov, M. Hanson and A. C. Gossard. Electrostatic conveyer for excitons. Phys. Rev. Lett. **106**, 196806 (2011).

J. Wilkes, L. Mouchliadis, E. A. Muljarov, A. L. Ivanov, A. T. Hammack, L. V. Butov and A. C. Gossard. Dynamics of the inner ring in photoluminescence of GaAs/AlGaAs indirect excitons. J. Phys.: Conf. Series **210**, 012050 (2010).

A. T. Hammack, L. V. Butov, J. Wilkes, L. Mouchliadis, E. A. Muljarov, A. L. Ivanov and A. C. Gossard. Kinetics of the inner ring in the exciton emission pattern in coupled GaAs quantum wells. Phys. Rev. B **80**, 155331 (2009).

Presentations

J. Wilkes, A. A. Guenther, A. L. Ivanov, A. G. Winbow, J. R. Leonard, M. Remeika, Y. Y. Kuznetsova, A. A. High, A. T. Hammack, L. V. Butov, M. Hanson and A. C. Gossard. Electrostatic Conveyer for Excitons. *Conference on Cold Atoms, Semiconductor Polaritons and Nanoscience*, Crete (2-6 May 2011).

J. Wilkes, E. A. Muljarov and A. L. Ivanov. Classical dynamics vs. quantum coherence: External ring segregation in the indirect exciton photoluminescence pattern. *5th International Conference on Spontaneous Coherence in Excitonic Systems*, Lausanne (7-11 February 2011).

J. Wilkes, L. Mouchliadis, E. A. Muljarov, A. L. Ivanov, A. T. Hammack, L. V. Butov and A. C. Gossard. Photoluminescence dynamics of GaAs/AlGaAs indirect excitons. *Condensed Matter and Materials Physics*, Warwick (15-17 December 2009).

J. Wilkes, L. Mouchliadis, E. A. Muljarov, A. L. Ivanov, A. T. Hammack, L. V. Butov and A. C. Gossard. Dynamics of the inner ring in photoluminescence of GaAs/AlGaAs indirect excitons. *11th International Conference on Optics of Excitons in Confined Systems*, Madrid (7-11 September 2009).

Contents

List of Figures

1 Introduction

Since the first theoretical predictions that excitons - bound states of electrons and holes - may undergo Bose-Einstein condensation (BEC) [1], intensive studies have sought to realize the phenomena experimentally [2, 3]. BEC has been observed in atomic systems [4] and more recently in a system of microcavity polaritons [5, 6]. The arduous journey to observe BEC in an exciton system has inspired a diverse array of experiments and investigations [7–12]. Novel structures and techniques have been employed which, regardless of their success or failure, have deepened our understanding of the excitonic properties of semiconductors.

In past years, quasi-two-dimensional excitons in single and coupled quantum wells have been studied as candidates for observing BEC [13–15]. In particular, indirect excitons in coupled quantum wells (CQWs) are an attractive system for investigation due to their greatly extended lifetime over regular excitons. The long lifetime allows indirect excitons to be cooled below their quantum degeneracy temperature before decaying optically which has been an important step towards observing BEC of excitons.

Although the challenge of observing exciton BEC has been the primary motive behind research in this field, it is not discussed directly in this thesis. Instead, the dynamics of the transport of excitons confined to CQWs is studied theoretically. The main aim is to account for several striking features in the photoluminescence (PL) pattern originating from the optical decay of CQW excitons. Images of these patterns were first published a decade ago by two independent research groups [7, 8]. A summary of the observed features is shown in Fig. 1.1. They included a central bright spot which can be several times larger than the laser excitation spot. Within the

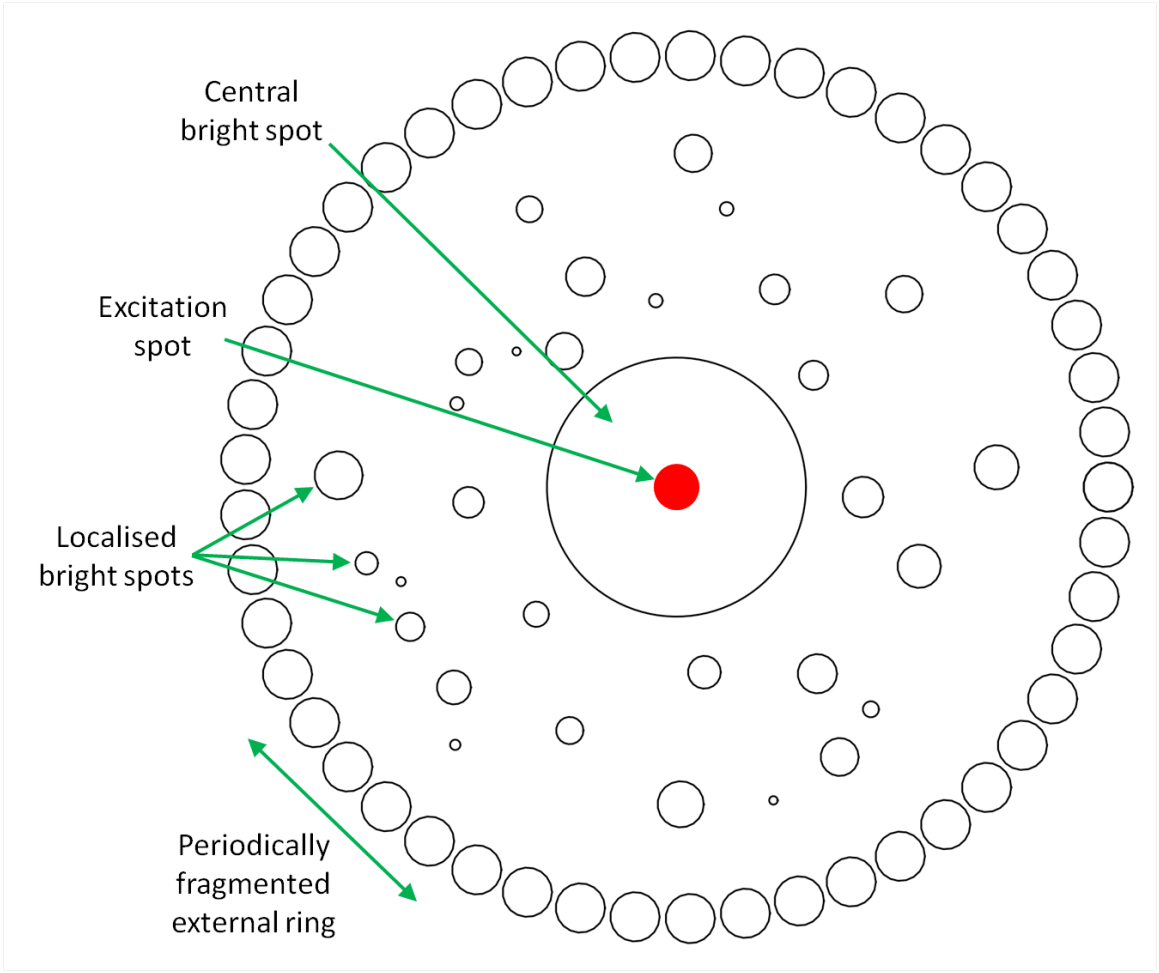

Figure 1.1: Overview of the features of the real space PL pattern originating from the optical decay of excitons in CQW heterostructures.

central bright spot is a ring, known as the *inner ring*, which surrounds the excitation spot. In a predominantly dark region beyond the edge of the inner ring, localised bright spots appear. These have been explained by current filaments between QW layers caused by defects in the sample structure [16, 17]. Even further from the excitation spot, an *external ring* was observed. This ring can be greater than 100 μm in diameter and encloses the other PL features. Under the correct conditions, the external ring is found to fragment into a periodic array of islands.

A drift-diffusion equation is used to analytically and numerically model the spatial density distribution of photoexcited excitons. In addition, the thermalisation kinetics of two-dimensional excitons is studied. Where appropriate, the relevant heating and cooling mechanisms are included into the description. The optical decay of excitons is also considered. This enables calculation of the spatial PL patterns which are observed in experiments.

Where experimental data was available, numerical simulations of those experiments were performed and quantitative comparisons of the observed and simulated exciton PL pattern were made. In particular, features of the exciton PL pattern such as the inner and external rings are successfully reproduced by the models used. The dynamics of excitons in artificially created potential landscapes is also investigated. All of these properties contribute to a deeper insight of exciton physics and may be key to achieving BEC in an exciton system. In addition, it lays the groundwork for understanding how to utilize excitons for applications in optical devices of the future.

1.1 Overview

Chapter one introduces the physics of excitons. It contains the background information necessary for the remainder of the thesis. Indirect excitons in CQWs are explained and brief descriptions of their transport, thermalisation and PL properties are given. Information on the relevant samples and experiments with which comparisons are made later is also shown.

Chapter two entitled "Transport and thermalisation kinetics in the exciton inner ring" is about the inner ring in the indirect exciton emission pattern. It details its origin and the evolution of its formation and collapse in terms of a model based on exciton transport and cooling. The inner ring's dependence on external parameters

such as laser excitation power and energy are discussed. Also, a remarkable feature of experiments known as the PL-jump is described. Quantitative comparisons are made between the results of numerical simulations and experimental data.

Chapter three entitled "Indirect excitons in applied in-plane potentials" is a study of the transport of indirect excitons in the presence of externally applied electric fields. Such electric fields can be used to confine and transport excitons in a controlled way. Analytic solutions to the relevant drift-diffusion equations for linear potential energy gradients are discussed. Comparison of numerical solutions for exciton transport with experimental data are made for a ramp - a linear potential energy gradient, and a conveyer - a moving electrostatic lattice.

Chapter four entitled "Fragmentation of the external exciton ring" presents a model to explain the physical mechanism which causes the external ring in the indirect exciton emission pattern to fragment into a periodic array of islands. A coupled set of drift-diffusion equations for electrons, holes and excitons is used. Terms accounting for the Coulomb interaction between charges are included and are found to be responsible for the fragmentation. The main conclusions and prospects for future research are summarised in chapter five.

1.2 EXCITONS IN SEMICONDUCTORS

In semiconductors, photon absorption promotes an electron from the valence band to the conduction band, creating a hole in the valence band. The electron and hole may form a bound complex known as an exciton. Excitons have a hydrogenic structure. Its internal constituents, the electron-hole pair, orbit each other about a common center of mass whilst the exciton as a whole is free to roam the semiconductor lattice. This can be shown in the effective mass approximation by the electron-hole Hamiltonian,

$$\hat{H} = -\frac{\hbar^2}{2m_{\mathrm{e}}}\Delta_{\mathrm{e}} - \frac{\hbar^2}{2m_{\mathrm{h}}}\Delta_{\mathrm{h}} + E_g + V(\mathbf{r}_{\mathrm{e}}, \mathbf{r}_{\mathrm{h}}), \tag{1.1}$$

where $m_{\mathrm{e(h)}}$ is the electron (hole) effective mass and $\Delta_{\mathrm{e(h)}}$ is the Laplacian operator in the electron (hole) coordinate frame, $\mathbf{r}_{\mathrm{e(h)}}$. E_g is the semiconductor band gap energy. In bulk semiconductors, the Coulomb interaction potential is $V(\mathbf{r}_{\mathrm{e}}, \mathbf{r}_{\mathrm{h}}) = -e^2/(4\pi\varepsilon_0\varepsilon_r|\mathbf{r}_{\mathrm{e}} - \mathbf{r}_{\mathrm{h}}|)$ where ε_r is the background permittivity. The Hamiltonian

splits into two parts which results in the following two Schrödinger equations,

$$-\frac{\hbar^2}{2M_{\mathrm{x}}}\Delta_{\mathbf{R}}\psi = E_k\psi, \tag{1.2}$$

$$\left[-\frac{\hbar^2}{2\mu}\Delta_{\mathbf{r}} - \frac{e^2}{4\pi\varepsilon_0\varepsilon_r|\mathbf{r}|}\right]\varphi = E_b\varphi. \tag{1.3}$$

The coordinate frames $\mathbf{R}$ and $\mathbf{r}$ are the center of mass and relative coordinates respectively. $M_{\mathrm{x}} = m_{\mathrm{e}} + m_{\mathrm{h}}$ is the exciton mass and $\mu = (1/m_{\mathrm{e}} + 1/m_{\mathrm{h}})^{-1}$ is the reduced mass. E_k is the kinetic energy associated with the exciton's center of mass motion and E_b is the binding energy. Equation (1.2) has plane wave solutions for the exciton center of mass motion and equation (1.3) describes its internal structure which reveals the exciton binding energy and Bohr radius. In bulk gallium-arsenide (GaAs), the exciton binding energy is 4 meV and its Bohr radius is 13.5 nm, much greater than the GaAs unit cell size of 0.56 nm.

Excitons are unstable particles with an optical lifetime typically less than 1 ns. The overlap between the electron and hole wave functions means that there is a finite probability per unit time of electron-hole recombination. Therefore, the presence of excitons is observed in various semiconductors indirectly by the light emitted during their decay. Excitons modify the emission and absorption spectra of semiconductors and cause a peak in the PL intensity at energies just below the band gap energy at the exciton resonance [18]. This peak is strongly defined for high-purity semiconductors at temperatures well below room temperature where broadening due to impurities and phonon interactions is small. In this case, spectrally resolved measurements make it possible to distinguish the exciton PL signal from other optical transitions.

1.3 Excitons in coupled quantum wells

Quantum wells (QWs), commonly fabricated using molecular beam epitaxy, consist of a thin semiconductor layer sandwiched between semiconductor layers with a higher band gap energy. Electrons and holes are confined to the QW layers, the thickness of which can be less than the particles' de Broglie wavelength. Such confinement causes quantization of energy in the growth direction. Excitons in QWs have the advantage of being more tightly bound than in bulk materials which stabilizes them against ionisation. Solving equations (1.2-1.3) in two-dimensional geometry shows a reduction of the Bohr radius and an increase in binding energy. This leads to

an enhancement of the optical effects of excitons in two-dimensional heterostructures compared to that of bulk materials.

One of the main challenges preventing Bose-Einstein condensation of excitons in bulk materials and in single QWs is their short radiative lifetime. To achieve condensation, one first needs a cold exciton gas. However, photo-excited excitons which are initially hot tend to decay optically before they can thermalise to the lattice temperature. Increasing the exciton lifetime so as to enable effective thermalisation before optical decay can be achieved by using indirect excitons in coupled quantum wells (CQWs). CQWs consist of two single QWs separated by a barrier layer of higher band gap energy (See Fig. 1.2a). The barrier layer is sufficiently thin to allow charges to tunnel between the QW layers.

In CQWs, there are direct and indirect excitons. A direct exciton is a bound complex of an electron and a hole in the same quantum well (Fig. 1.2b). An indirect exciton is a bound complex of an electron and a hole in adjacent quantum wells. To encourage all excitons to be of the latter variety, an electric field is applied perpendicular to the QW plane. This shifts the electron and hole energy levels so that the ground state exciton is indirect (Fig. 1.2c). Electrons and holes will relax into their respective wells by tunneling through the narrow barrier layer. This results in indirect excitons being the dominant type.

The exciton lifetime increases as the overlap between electron and hole wave functions decreases. The indirect exciton lifetime can be orders of magnitude longer than the direct exciton lifetime [19]. Due to the exponential decay of the wave functions in the barrier region, the indirect exciton lifetime is highly sensitive to the barrier width. Moreover, the wave function overlap can be controlled by adjusting the electric field. In experiments, this allows the lifetime to be varied over a few orders of magnitude by adjustment of the gate voltage. The lifetime can easily exceed the time required for excitons to cool to the temperature of the lattice.

Indirect excitons in CQWs present a unique system for studying a two dimensional degenerate Bose gas in solids. Through experimental and theoretical studies, a rich variety of physical properties of indirect excitons have been uncovered [20, 21]. Some of the main concepts which are relevant throughout this thesis are outlined in the following sections.

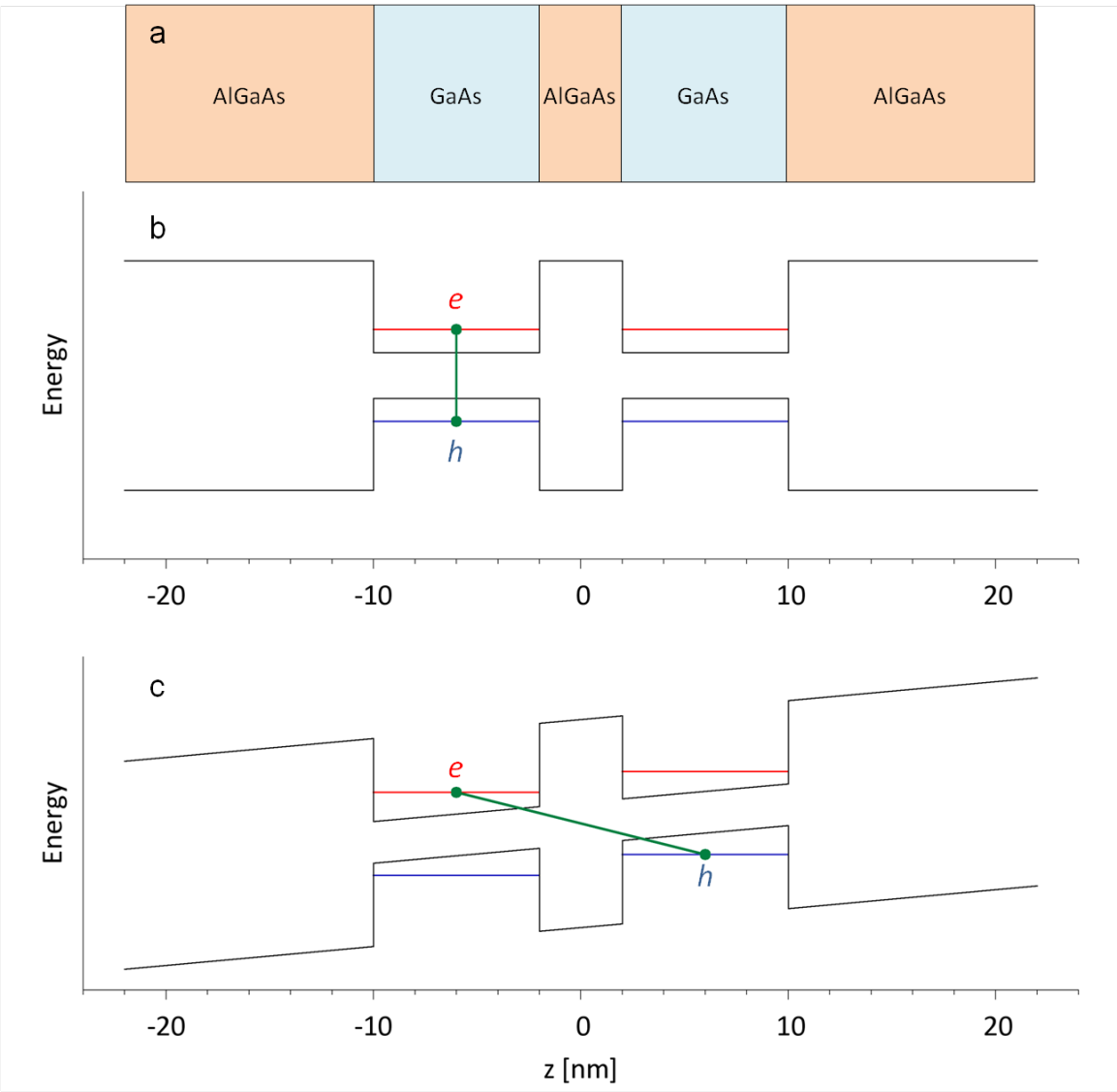

Figure 1.2: (a) Schematic of the CQW sample structure. (b) CQW band diagram without an applied electric field. The red and blue lines correspond to electron and hole states respectively. (c) Band diagram modified due to an electric field in the z-direction. Green lines show a direct exciton in (b) and an indirect exciton in (c).

1.4 TWO-DIMENSIONAL TRANSPORT

The transport of a given gas can, quite generally, be modeled by the following kinetic equation:

$$\frac{\partial n}{\partial t} = -\nabla \cdot \mathbf{J} + \Lambda(t, \mathbf{r}) - \frac{n}{\tau}. \tag{1.4}$$

This equation describes the rate of change of density $n = n(t, \mathbf{r})$ at each coordinate $\mathbf{r}$ and time t. The first term on the right hand side of equation (1.4) originates from the continuity equation. It accounts for particle transport via a flux $\mathbf{J}$ and guarantees the conservation of particles during transport. In the two dimensional geometry relevant to quantum wells, the gradient operator is $\nabla = \partial/\partial x\ \hat{\mathbf{e}}_x + \partial/\partial y\ \hat{\mathbf{e}}_y$ where $\hat{\mathbf{e}}_x$ and $\hat{\mathbf{e}}_y$ are the orthogonal in-plane unit vectors. The second and third terms describe the creation and decay of particles respectively. $\Lambda(t, \mathbf{r})$ corresponds to the time varying profile of the particles' source and τ is their lifetime.

Throughout this thesis, equation (1.4) is adapted several times to model the creation, transport and decay of excitons and, in some cases, free electrons and holes. Through modifying the flux $\mathbf{J}$ appropriate to each context, a variety of physical mechanisms can be included enabling the modeling of a broad range of exciton experiments. The effects of externally applied potentials and particle-particle interactions between one or more species are easily included.

1.5 INDIRECT EXCITON MACROSCOPIC DIPOLE MOMENT

Due to the separation of electrons and holes into their respective QWs, indirect excitons are dipoles aligned perpendicular to the CQW plane. The dipole-dipole repulsion between indirect excitons stabilizes them against droplet formation [22]. Also, at high density, it significantly modifies the in-plane exciton transport [23].

The indirect exciton potential resulting from dipole interaction is approximately proportional to the two-dimensional indirect exciton density, n_{x} [24]. During optical decay, when the electron-hole pair recombines to emit a photon, the photon acquires the interaction energy. This has been observed in experiments as a blue shift in the PL spectrum which increases with exciton density [25–27]. The blue shift has maxima in the regions of laser excitation and in the minima of externally applied potentials - areas where the exciton density is peaked.

Indirect excitons drift due to the gradient in the dipole-dipole interaction potential. This mechanism enhances their diffusion from regions of high to low density as they distribute themselves in the QW plane so as to achieve the lowest energy configuration. In the simplest approximation, this interaction potential is given by $u_0 n_x$ with u_0 approximated by the plate capacitor formula [24],

$$u_0 = \frac{4\pi e^2 d_z}{\varepsilon_r}. \tag{1.5}$$

Here, d_z is the separation between the electron and hole layers. One outcome of the dipolar nature of excitons is their ability to screen QW disorder. Such disorder potentials are intrinsic to any QW structures and are due to alloy fluctuations and variations in the thickness of the wells and the barrier between them [28]. For low intensity optical excitation where a dilute gas is created, excitons become localized in the minima of the random disorder potential. However, at higher densities, more excitons accumulate in the potential minima and the resulting effective exciton potential is flattened by the exciton-exciton interaction [29]. As density is increased further, additional excitons are completely unaffected by the random potential and so the QW disorder is screened. This facilitates a *localisation-delocalisation* transition where the spatial width of the exciton cloud has a threshold dependence on the generation rate.

Combined with their long lifetimes, a high density indirect exciton cloud can extend well beyond the region of a focused laser excitation spot. This is in contrast to the situation of no electric field perpendicular to the QW plane where direct excitons are found only within the vicinity of the laser due to short lifetimes and reduced transport distances.

1.6 Control of exciton transport by external electric fields

Compared to direct or bulk excitons which possess no macroscopic dipole moment, indirect exciton transport can be very effectively controlled via externally applied electric fields. Although excitons are neutral particles, patterned electrodes on the sample surface create an in-plane potential landscape which influences their transport. This is because for a negatively charged electrode, the attracted hole part of the exciton is closer to the electrode than the repulsed electron part meaning

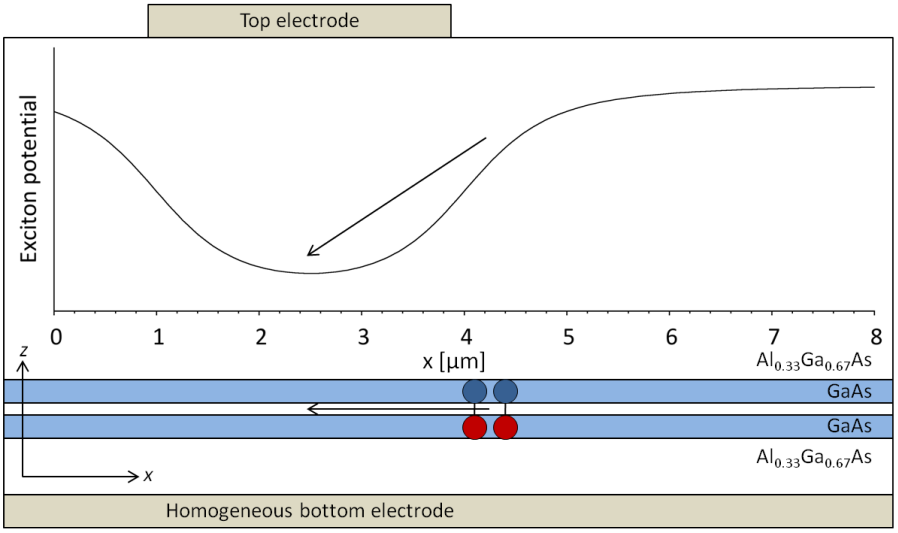

Figure 1.3: CQW structure with patterned electrodes. The red and blue circles depict electron and hole parts of indirect excitons respectively. Inset: the exciton potential due to the shaped electrode attached to the upper surface of the sample.

that the net force is an attractive one. Indirect excitons will tend to accumulate underneath patterned electrodes where the applied potential has a minimum [30]. An example of this is shown in Fig. 1.3 where the exciton potential due to the shaped upper electrode is calculated using a rigid dipole approximation of the exciton.

Nowadays, the ease with which electrodes can be patterned on QW samples presents a freedom for experimentalists to create almost any potential landscape they choose. Several experiments have been done to investigate indirect exciton transport in various potentials including traps [31–34], elevated traps [35], lattices [36–38], moving lattices [39], ramps [40, 41] and narrow channels [42, 43]. In many of these experiments, localisation-delocalisation transitions have been observed. These are similar to effect described above where excitons screen QW disorder. However, in this case a dense enough exciton gas can screen the applied potential and delocalise from its minima.

1.7 Optical decay of QW excitons

Due to the spatial confinement of excitons to the QW layers, there is an absence of momentum conservation in the direction perpendicular to the QW plane. The in-plane momentum is still conserved. Therefore, in the optical decay of two-dimensional excitons, the emitted photon acquires the in-plane momentum of the

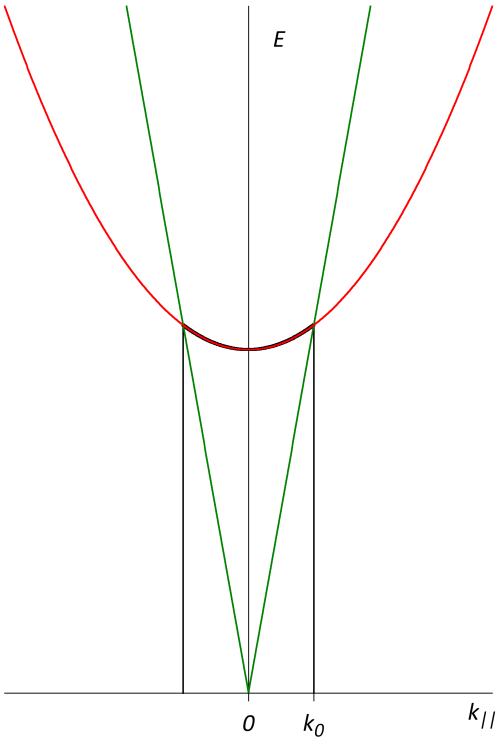

Figure 1.4: Exciton (red) and photon (green) dispersion relations. The optically active exciton states are shown by the black part of the exciton dispersion

exciton. However, the component the photon momentum in the growth direction is unrestricted. Combining this idea with the photon and exciton dispersion relations, one arrives at a selection rule for the optical decay of quantum well excitons. The dispersion relations are plotted in Fig. 1.4 and are given by,

$$E_{\mathrm{x}} = E_g - E_b + \frac{\mathbf{p}_{||}^2}{2M_{\mathrm{x}}}, \tag{1.6}$$

$$E_\omega = \frac{c|\mathbf{p}_\gamma|}{\sqrt{\varepsilon_r}}. \tag{1.7}$$

E_{x} and E_ω are the exciton and photon energies respectively. E_g if the band gap energy and E_b is the exciton binding energy. Equating (1.6) and (1.7) and substituting the in-plane momentum conservation law, one finds that for optical decay, $\mathbf{p}_{||}$ must satisfy $|\mathbf{p}_{||}| \leq |\mathbf{p}_\gamma|$. This means that only excitons inside the light cone with in-plane momentum below a critical value can decay optically (See Fig. 1.4). This has the following implications for the PL and thermalisation kinetics of QW excitons:

1. Initially high energy photo-excited excitons must relax to the lowest energy

states before they may recombine to emit light. Typically, this occurs via the emission of longitudinal-acoustic (LA) phonons.

2. Increasing the temperature of a two dimensional exciton gas suppresses optical decay. Laser induced heating or an increase in the lattice temperature reduces the fraction of excitons with momentum inside the light cone.

3. The temperature of a two dimensional exciton gas is increased by optical decay. This is because the lowest energy particles are continually removed from the system resulting in a higher energy per particle.

The above is in contrast to the case of bulk excitons where only the state with zero translational kinetic energy may couple to the light field.

1.8 THERMALISATION KINETICS OF QW EXCITONS

In CQWs, non-resonant optical excitation creates unbound high energy electron - hole pairs. Within the short exciton formation time, emission of optical phonons releases energy from the electron-hole pairs to the lattice which then bind to form excitons. At this stage, the exciton temperature still greatly exceeds the lattice temperature. Following this, cooling of the exciton gas towards the lattice temperature is done by the emission of LA-phonons.

Similar to the case described above for photon emission, the emission and absorption of LA phonons is modified by the spatial confinement of excitons in the growth direction. Excitons with energy greater than a critical energy, E_0 can emit LA-phonons to relax in energy (See Fig. 1.5). The coupling of excitons to a continuum of phonon states greatly enhances the thermalisation compared to the bulk case where only excitons with energy E_0 may emit a phonon.

In the absence of any heating, CQW excitons will rapidly cool to a temperature of roughly E_0/k_{B} provided that the lattice temperature, T_b, is below this. This cooling occurs within a few nanoseconds, well within the indirect exciton lifetime. If T_b is much less than E_0/k_{B}, the cooling rate of excitons at temperatures $T < E_0/k_{\mathrm{B}}$ becomes greatly reduced. This is because excitons with energy less than E_0 cannot emit LA phonons. The only way to cool further is to first absorb a LA-phonon

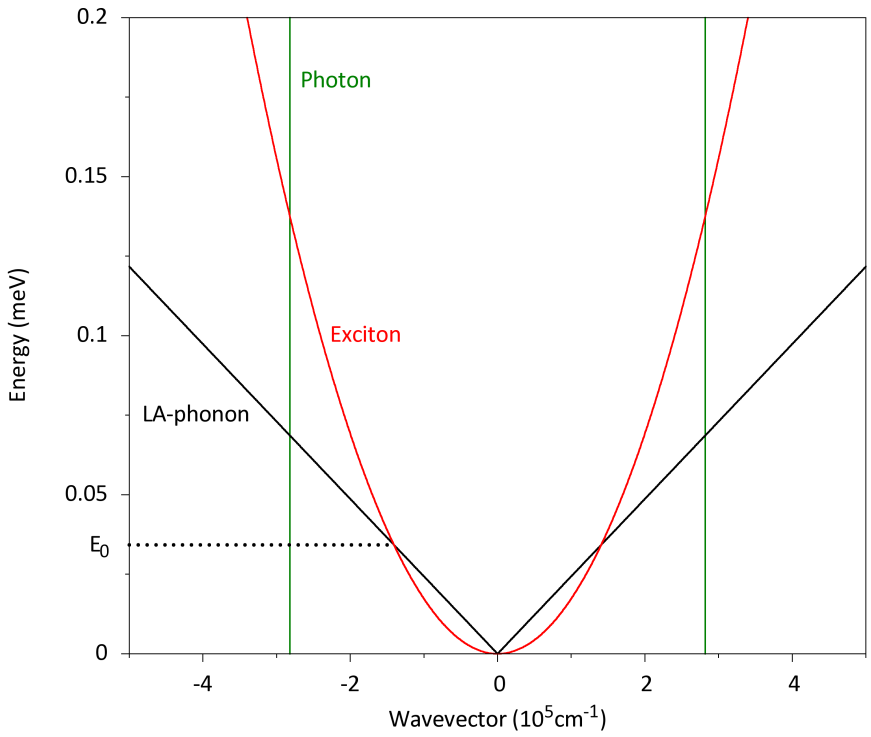

Figure 1.5: Exciton (red), acoustic phonon (black) and photon (green) dispersion relations. The energy E_0 which marks the crossover of the exciton and LA-phonon dispersions is shown by the dotted line.

of energy $\approx E_0$ and then to re-emit one of greater energy. The probability of this decreases exponentially as the lattice temperature is reduced further because of the reduction in the density of LA-phonons. The time required for excitons to thermalise with the lattice therefore grows exponentially with decreasing T_b below E_0/k_{B} and can easily exceed the indirect exciton lifetime [44]. This slowing of the thermalisation time has posed an obstacle for achieving BEC in a system of indirect excitons.

The non-resonant excitation at energies well above the indirect exciton ground state energy creates excitons with large in-plane translational kinetic energy. The exciton-exciton scattering time is short and rapid thermalisation to a higher effective temperature occurs. This *laser induced heating* maintains an elevated temperature only in the vicinity of the excitation spot as excitons which travel away from that region then begin to cool towards the lattice temperature by emission of LA-phonons.

1.9 Sample structure and parameters

The samples considered throughout this thesis are those used by the group of Prof Leonid Butov at the University of California at San Diego. The structures were grown by molecular beam epitaxy. Two GaAs QWs, each 8 nm thick, are separated by a 4 nm $Al_{0.33}Ga_{0.67}As$ barrier. These layers sit within an undoped 1 μm thick $Al_{0.33}Ga_{0.67}As$ layer which is capped at each end by an n^+-GaAs electrode layer with $n_{\mathrm{Si}} = 10^{18}\,\mathrm{cm}^{-3}$. A schematic of the structure is shown in Fig. 1.6. Throughout this thesis, the physical parameters used in the modeling of CQW excitons are those corresponding to the samples described here and the conditions of the relevant experiment. A list of the parameters used and their values is given in table 1.1.

1.10 Summary

In this chapter, the basic underlying physics which is used throughout the remainder of this thesis has been outlined. The main concepts discussed are

- In-plane transport of indirect excitons which is driven by diffusion and drift. The drift current arises due to a well defined indirect exciton dipole moment

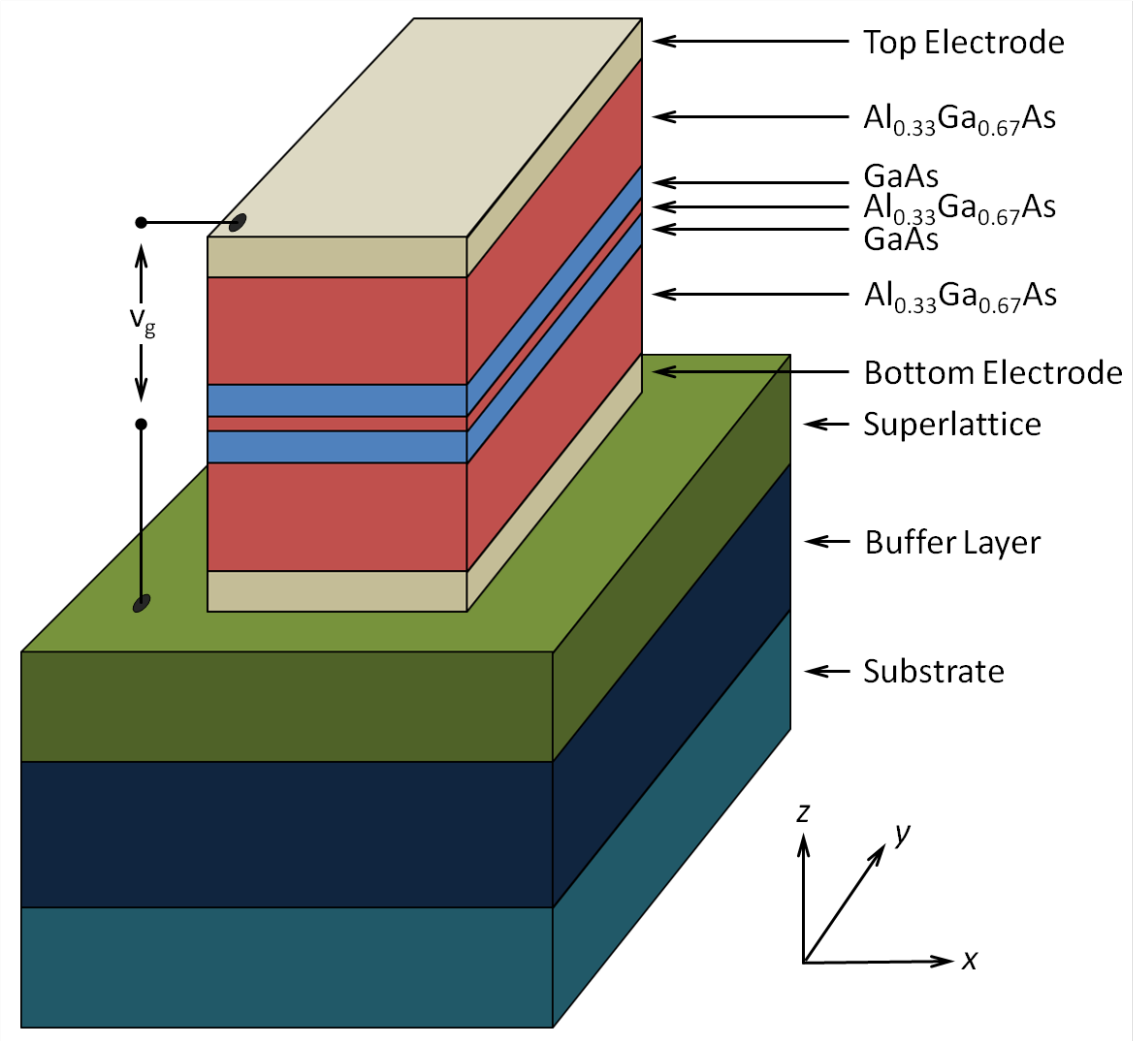

Figure 1.6: Schematic of the investigated CQW samples.

which cause exciton-exciton repulsion and enables control of exciton transport by patterned electrodes on the sample surface.

- Thermalisation kinetics of a quasi-two-dimensional Bose gas. Indirect excitons thermalise with the lattice by absorption and emission of bulk LA-phonons. Non-resonant excitation of excitons leads to laser induced heating of the exciton gas. The rate of cooling of initially hot two dimensional excitons is more efficient than that of bulk excitons.

- Optical decay of indirect excitons is strongly dependent on the exciton effective temperature. Only excitons with energy inside the light cone may decay optically. This gives an enhancement of the PL signal from CQW excitons over excitons in bulk materials. It also leads to evaporative heating of the exciton gas.

Much of the description given in this chapter is a simple qualitative one in order to familiarise the reader with the main concepts. In the following chapters, a quantitative analysis of these physical mechanisms will be shown. From the more detailed quantitative picture, numerical simulations have been constructed. Results from these simulations will be presented and, where appropriate, comparisons with available experimental data will be made.

Table 1.1: List of Parameters

Symbol	Value	Description
m_{e}	$0.067\,m_0$	Effective electron mass
m_{h}	$0.215\,m_0$	Effective hole mass
E_g	1.42 eV	GaAs band gap energy
ε_r	12.9	GaAs relative permittivity
M_{x}	$0.22\,m_0$	Exciton mass
E_b	4 meV	Exciton binding energy
a_{x}	13.5 nm	Exciton Bohr radius
d_z	12.5 nm	Spacing between electron and hole layers
d_{elec}	$1\,\mu$m	Spacing between CQWs and patterned electrodes
u_0	1.6×10^{-10} meV cm^2	Exciton interaction energy per unit of density
U_0	0.7-1.5 meV	Amplitude of the CQW disorder potential
$D_{\mathrm{x}}^{(0)}$	30 cm^2 s^{-1}	Indirect exciton diffusion coefficient in the absence of the CQW disorder potential
E_0	$34.2\,\mu$eV	Energy at the intersection between exciton and LA-phonon dispersion relations
ν_s	3.7×10^5 cm s^{-1}	Sound velocity in GaAs
ρ_c	5.3 g cm^{-3}	GaAs crystal density
D_{dp}	8.8 eV	Deformation potential
d_{QW}	8 nm	Quantum well thickness
E_γ	$138\,\mu$eV	Energy at the intersection between exciton and photon dispersion relations
τ_r	20 ns	Intrinsic radiative lifetime
θ_c	30°	Collection angle of imaging device
D_{e}	30 cm^{2}s^{-1}	Electron diffusion coefficient
D_{h}	15 cm^{2}s^{-1}	Hole diffusion coefficient
w	10^3 cm^{2}s^{-1}	Binding rate of free electron-pairs into excitons per unit density
τ_{e}	50 ns	Electron re-population time
$n_{\mathrm{e}}^{(0)}$	0.5-1.2 $\times 10^9$cm^{-2}	Background electron density in CQWs

2 Transport and thermalisation kinetics in the exciton inner ring

A prerequisite for achieving Bose-Einstein condensation of excitons is the creation of a cold and dense exciton gas. Many studies of the exciton thermodynamics have been done in an effort to identify a means to realise a system where the exciton temperature is below the temperature of quantum degeneracy. For a two dimensional gas of excitons, the quantum degeneracy temperature, T_0 is given by

$$T_0 = \frac{2\pi\hbar^2}{gM_{\mathrm{x}}k_{\mathrm{B}}}n_{\mathrm{x}}. \tag{2.1}$$

For excitons in GaAs QWs, the spin degeneracy factor is $g = 4$ and the exciton mass is $M_{\mathrm{x}} = 0.22m_0$ where m_0 is the free electron mass. n_{x} is the two-dimensional density of indirect excitons. T_0 =0.63 K for $n_{\mathrm{x}} = 10^{10}\,\mathrm{cm}^{-2}$.

In this chapter, two features of the exciton photoluminescence (PL) pattern known as the *inner ring* and the *PL-jump* are studied. These phenomena have been identified as signatures of the heating induced by the non-resonant optical excitation of electron hole pairs [45, 46]. Therefore, their study provides a means to gain insight into the thermalisation of excitons with a semiconductor lattice at very low bath temperatures ($T_b = 1 - 2\,\mathrm{K}$). For a complete description necessary to make quantitative comparisons with experimental data, a model of exciton creation, transport, thermalisation and photoluminescence is used [47, 48].

2.1 Background

Many previous experimental and theoretical works on the optical properties of GaAs/AlGaAs CQWs have involved the study of the spatial PL pattern originating from optically decaying indirect excitons. Excitons were created by a laser excitation of the medium focused to a single point in the QW plane. In the resulting PL pattern, a bright ring appears surrounding the excitation spot [48–50]. The origin of this inner ring has been interpreted as follows [45, 51, 52]. First, the non-resonant optical excitation creates free electron hole-pairs. These rapidly bind to form indirect excitons which are high in energy. A very short equilibration time means that the high energy injected excitons cause heating of the exciton gas at the excitation spot. The excitons diffuse away from the laser spot and their transport is assisted by the dipole-dipole repulsion. As they travel away from the heat source, they begin to cool to the lattice temperature. The cooling time is longer than the equilibration time but still rapid in comparison to the long lifetime and so excitons reach the lattice temperature well before decaying. The key ingredient of the interpretation is that, as discussed in chapter one, only low energy excitons with momentum inside the light cone may decay to emit light. Therefore, the lifetime of excitons inside the region of the excitation spot is much greater than the lifetime outside. Consequently the exciton decay rate and hence the PL signal is suppressed by laser excitation causing a reduction in PL signal. This leads to the appearance of the inner ring.

In the time domain, the counterpart of the inner ring is the PL-jump. During the continuous laser induced heating, a large population of excitons is sustained because of the extended exciton lifetime. When the laser is switched off, the exciton temperature rapidly drops and the entire population rapidly cools and becomes optically active. This causes an abrupt jump in the PL signal [53, 54] as the exciton optical lifetime decreases. This effect is known as the PL-jump.

2.2 Creation of excitons

The laser beam creates free electron-hole pairs which, on a sub-nanosecond time scale, bind to form excitons. As the pumping is continuous, at every moment all three species - namely electrons, holes and excitons - are present. In other works [55–57], it has been suggested that in the PL experiments considered here, the underlying

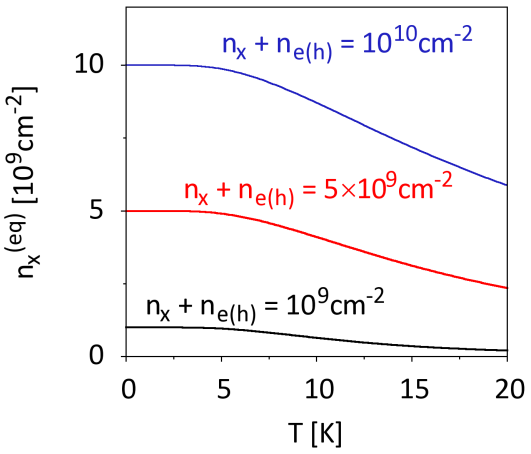

Figure 2.1: Fraction of electron-hole pairs in the bound exciton state as a function of temperature. Each curve is for a fixed number of electrons and holes with $n_e = n_h$.

physical picture is that of ambipolar diffusion of unbound electrons and holes. However, a quantum mass action law can be used to determine the number of electron-hole pairs in the unbound and bound exciton states [58]. The quantum mass action law is derived in appendix A. It states that the equilibrium exciton density, $n_x^{(eq)}$, satisfies the following relation,

$$n_x^{(eq)} = \frac{k_B M_x T}{2\pi\hbar^2} \ln[1 - e^{-E_b/k_B T}(e^{T_0^e/T} - 1)(e^{T_0^h/T} - 1)]. \tag{2.2}$$

Equation (2.2) describes the equilibrium balance between the concentrations of excitons and free electron-hole pairs. $T_0^{e(h)} = \pi\hbar^2 n_{e(h)}/(m_{e(h)}k_B)$ is the electron (hole) quantum degeneracy temperature where $n_{e(h)}$ and $m_{e(h)}$ are the electron (hole) density and effective mass respectively. Solutions of the transcendental equation (2.2) are shown in Fig. 2.1 for equal numbers of electrons and holes ($n_e = n_h$) and a fixed number of pairs ($n_{e(h)} + n_x$ = constant). The equilibrium exciton density, $n_x^{(eq)}$ is plotted as a function of temperature with each curve corresponding to a fixed number of charges in the system. The exciton density range relevant to the considered experiments has been determined by the blue shift in the exciton line. See, for example, Refs. [25–27, 58]. The plot shows that for these densities and temperatures below 5K, excitons completely dominate in number over free electron hole-pairs. This suggests the PL signal observed in the experiments considered here originates from the optical decay of excitons rather than the recombination of free carriers. Further, an exciton system may be distinguished from an electron-hole plasma by examining the PL line width. The line width for a neutral two-dimensional electron-hole plasma is approximately

the sum of the electron and hole Fermi energies, $\Delta_{\mathrm{EHP}} \approx k_{\mathrm{B}}T_0^e + k_{\mathrm{B}}T_0^h$. The smallest density for an electron-hole plasma is determined by the exciton Mott transition, which occurs due to the phase-space filling and screening at electron hole densities greater than $1/a_{\mathrm{x}}^2$ where a_{x} is the exciton Bohr radius [59]. For the CQW structures considered here, one finds that the smallest line width that would be observed for an electron-hole plasma is about 10 meV. This is much greater than the observed line width which is typically below 2 meV for the investigated range of densities [48, 49]. The small emission line width, which is determined by the homogeneous and inhomogeneous broadening, is a signature of an exciton system rather than an electron-hole plasma.

2.3 In-plane exciton transport equation

In chapter one, the equation for in-plane transport of indirect excitons was introduced and is repeated here for clarity

$$\frac{\partial n_{\mathrm{x}}}{\partial t} = -\nabla \cdot \mathbf{J} + \Lambda - \frac{n_{\mathrm{x}}}{\tau_{\mathrm{opt}}}. \tag{2.3}$$

Here, the exciton flux has two components [24]; $\mathbf{J} = \mathbf{J}_{\mathrm{diff}} + \mathbf{J}_{\mathrm{drift}}$. The first is a diffusive term which is due to random scattering of excitons,

$$\mathbf{J}_{\mathrm{diff}} = -D_{\mathrm{x}}\nabla n_{\mathrm{x}}. \tag{2.4}$$

D_{x} is the density and temperature dependent exciton diffusion coefficient. The second term is the drift flux caused by the exciton-exciton interaction potential,

$$\mathbf{J}_{\mathrm{drift}} = -\mu_{\mathrm{x}} n_{\mathrm{x}} \nabla(u_0 n_{\mathrm{x}}). \tag{2.5}$$

μ_{x} is the exciton mobility and $u_0 n_{\mathrm{x}}$ is the interaction energy. The remaining terms on the right hand side of equation (2.3) account for the creation and decay of indirect excitons. The source term $\Lambda(\mathrm{r}, t)$ is calculated using equation (2.2). The time dependent Gaussian profile of the laser determines the injection rate of electron-hole pairs. Then, the quantum mass action law determines the number of pairs in the bound exciton state which, in turn, determines Λ. τ_{opt} is the optical lifetime of excitons.

2.3.1 THERMIONIC MODEL OF THE DIFFUSION COEFFICIENT

Intrinsic to the CQW structure is a random disorder potential caused by defects and imperfections in the sample growth. The random disorder potential, $U_{\text{rand}}(\mathbf{r})$, acts to impede exciton in-plane transport since low energy excitons become localised to potential minima. However, as the exciton density increases, the localised states in the disorder potential become occupied. Due to the dipole-dipole repulsion of indirect excitons, the disorder potential is then flattened so that additional excitons may transport as if the disorder were absent. This *screening* of the disorder leads to greatly enhanced exciton transport at high densities. This effect, which strongly modifies the transport dynamics, is included in the theory by modification of the diffusion coefficient, D_{x}. A thermionic model [24] for D_{x} can be derived from equation (2.3) to give

$$D_{\text{x}} = D_{\text{x}}^{(0)} \exp\left[\frac{-U_0}{u_0 n_{\text{x}} + k_B T}\right]. \tag{2.6}$$

Here, $D_{\text{x}}^{(0)}$ is a fit parameter and corresponds to the diffusion constant in the absence of disorder and $U_0/2 =< |U_{\text{rand}}(\mathbf{r}) - < U_{\text{rand}}(\mathbf{r}) > | >$ is the amplitude of the disorder potential. Equation (2.6) also includes the temperature dependence of the excitons' ability to transport through a disorder potential. Excitons with high in-plane kinetic energy are less likely to become trapped in the disorder potential. Therefore, increasing the temperature of the exciton gas has the same effect as screening of the disorder.

2.3.2 EXCITON MOBILITY

Another addition to the transport equation (2.3) is the generalized Einstein relation for the exciton mobility. The mobility of a degenerate gas of excitons is given by

$$\mu_{\text{x}} = \frac{D_{\text{x}}}{k_{\text{B}} T_0}(e^{T_0/T} - 1). \tag{2.7}$$

A full derivation of this can be found in Ref. [60]. Essentially, it takes into account the increase of particle flux due to applied fields as the exciton gas becomes more degenerate. In the classical limit, when $T_0/T << 1$ the mobility returns to the well-known Einstein relation for a classical gas obeying Maxwell-Boltzmann statistics:

$$\mu_{\text{clas}} = \frac{D_{\text{x}}}{k_{\text{B}} T}. \tag{2.8}$$

In both cases, what is described is that lowering the temperature reduces random scattering and therefore enhances drift currents over diffusive ones. At low temperature, exciton transport is driven more strongly by particle-particle interactions and external fields.

2.3.3 Geometry and boundary conditions

In the remainder of this chapter, only a radially symmetric laser profile is considered. This means that the resulting exciton cloud will be radially symmetric about the center of the laser excitation spot and therefore the transport equation is best solved using cylindrical geometry. The gradient operator is

$$\nabla = \frac{\partial}{\partial r}\hat{\mathbf{e}}_r + \frac{1}{r}\frac{\partial}{\partial \theta}\hat{\mathbf{e}}_\theta, \tag{2.9}$$

and the Laplace operator is

$$\nabla^2 = \frac{1}{r}\frac{\partial}{\partial r} + \frac{\partial^2}{\partial r^2} + \frac{1}{r^2}\frac{\partial^2}{\partial \theta^2}. \tag{2.10}$$

For the case of radial symmetry, one uses $\partial/\partial\theta = 0$. The Laplace operator appears to diverge for $r \to 0$. However, by considering a Taylor expansion of a cylindrically symmetric function about the origin, one finds

$$(\nabla^2)_{r=0} = 2(\frac{\partial^2}{\partial r^2})_{r=0}. \tag{2.11}$$

Finally, due to the finite lifetime of excitons, we anticipate that $n_\mathrm{x} \to 0$ as $r \to \infty$.

2.3.4 Analytic solutions of the transport equation

In the absence of source and decay terms (a fixed population of excitons) and neglecting the QW disorder potential so that $D_\mathrm{x} = D_\mathrm{x}^{(0)}$, one can derive analytic solutions to equation (2.3) in two limiting cases. The first case is where transport is governed only by diffusion so that $\mathbf{J}_\mathrm{drift} = 0$. For indirect excitons, this corresponds to the case of high temperature or low density where random scattering dominates

over the exciton-exciton interaction. The transport equation in this case is,

$$\frac{\partial n_{\mathrm{x}}}{\partial t} = D_{\mathrm{x}} \nabla^2 n_{\mathrm{x}}. \tag{2.12}$$

This has a well known solution of a Gaussian profile which shows transport of excitons from regions of high to low concentration:

$$n_{\mathrm{x}} = \frac{N}{2D_{\mathrm{x}}t} \exp\left(\frac{-r^2}{4D_{\mathrm{x}}t}\right), \tag{2.13}$$

where $N = \int_0^\infty r n_{\mathrm{x}}(r) dr$ is the total exciton population. The distribution originates from a delta function at $t = 0$.

The second limit is where the transport is driven by the dipole-dipole interactions and diffusion is absent. This corresponds to low temperatures where thermal scattering is negligible or high densities where the inter-particle interactions are strong. In the latter case the transport equation becomes,

$$\frac{\partial n_{\mathrm{x}}}{\partial t} = \mu_{\mathrm{clas}} u_0 (n_{\mathrm{x}} \nabla^2 n_{\mathrm{x}} + (\nabla n_{\mathrm{x}})^2). \tag{2.14}$$

The solution of equation (2.14) is a parabola which, like the solution to the diffusive equation (2.12), acts to minimise particle density.

$$n_{\mathrm{x}} = \begin{cases} \sqrt{\frac{N}{2\mu_{\mathrm{clas}} u_0 t}} - \frac{r^2}{8\mu_{\mathrm{clas}} u_0 t} & \text{if } r < \sqrt{32 N \mu_{\mathrm{clas}} u_0 t}, \\ 0 & \text{otherwise.} \end{cases} \tag{2.15}$$

Plots of these solutions are given in Figs. 2.2a and 2.2b for $N = 100$, $D_{\mathrm{x}} = 10\,\mathrm{cm^2 s^{-1}}$, $u_0 = 1.6 \times 10^{-10}\,\mathrm{meV\,cm^2}$ and $T = 10\,\mathrm{K}$. The size of the exciton cloud is quantified by the second moment of the density distributions, $M_2(t) = \int r^2 n_{\mathrm{x}}(r,t) dr$. This is shown in Fig. 2.2c for the drift and diffusion regimes. It is seen that in the high density limit, an initial rapid expansion of the exciton gas occurs due to the dipolar interactions [23]. Then, at lower density, the transport becomes diffusive in nature.

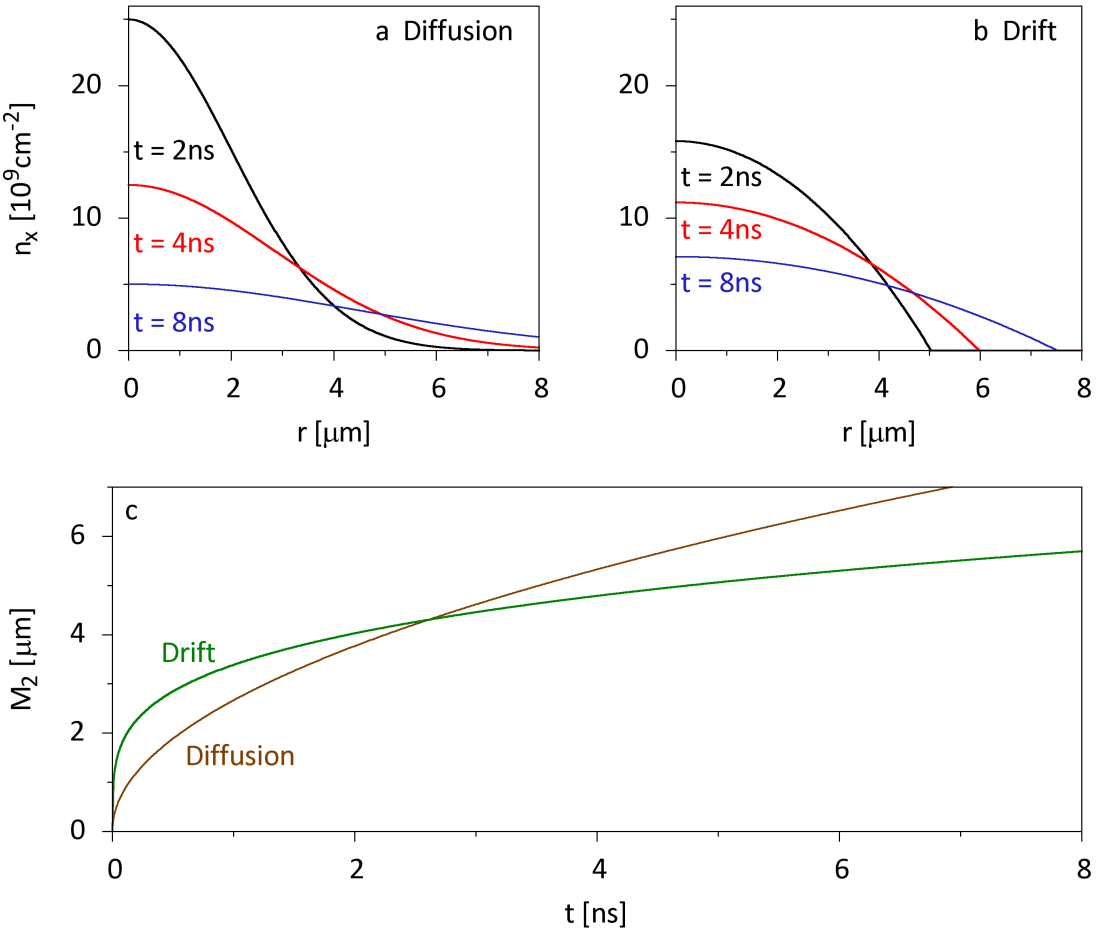

Figure 2.2: Analytic solutions to the diffusion equation (a) and drift equation (b). Parameters are given in the main text. The width of the exciton cloud as quantified by M_2 as a function of time for the diffusive and drift regimes (c).

2.4 THERMALISATION KINETICS OF INDIRECT EXCITONS

As summarised in chapter one, the evolution of the indirect exciton temperature at each point in the QW plane, $T(\mathbf{r}, t)$ is governed by three processes; (i) heating induced by the injection of high energy excitons, (ii) cooling via a bath of bulk LA-phonons and (iii) evaporative heating due to the optical decay of low energy excitons. The latter turns out to be the weakest of these so that the temperature is controlled mainly by the balance between incoming energy from the laser and energy dissipated to the lattice. The thermalisation kinetics are modeled by the following equation,

$$\frac{\partial T}{\partial t} = S_{\rm pump}(n_{\rm x}, T, E_{\rm ex}, \Lambda) + S_{\rm ph}(n_{\rm x}, T, T_b) + S_{\rm opt}(n_{\rm x}, T), \tag{2.16}$$

where $S_{\rm pump}$, $S_{\rm ph}$ and $S_{\rm opt}$ are rates of heating via optical excitation, LA-phonon interactions and optical decay respectively. Equation (2.16) describes the evolution of $T(\mathbf{r}, t)$ from an initial temperature $T(\mathbf{r}, t = 0)$. This initial temperature is assumed to be $E_{\rm ex}/k_{\rm B}$ in the vicinity of the laser excitation spot and zero elsewhere. The parameter $E_{\rm ex}$ is the excess energy acquired by excitons during their creation from unbound electron-hole pairs and is dependent on the laser excitation energy.

2.4.1 LASER INDUCED HEATING

To model the heating induced by the laser, it is assumed that the excitons which are deposited into the CQWs are constant in energy. This energy is $E_{\rm ex}$ and relates directly to the laser energy. The rapid equilibration of injected particles with the rest of the population means that the exciton gas can always be treated as being in equilibrium. In this framework, the laser induced heating is given by [45, 48],

$$S_{\rm pump} = \frac{E_{\rm ex} - k_{\rm B}TI_2}{2k_{\rm B}TI_1 - k_{\rm B}T_0I_2}\Lambda_{T_0}. \tag{2.17}$$

Here, $\Lambda_{T_0} = [(\pi\hbar^2)/(2M_{\rm x})]\Lambda(t, \mathbf{r})$ where $\Lambda(t, \mathbf{r})$ is exciton generation rate used in equation (2.3). The integrals $I_{1,2} = I_{1,2}(T, T_0)$ are given by

$$I_1 = (1 - e^{-T_0/T}) \int_0^\infty \frac{z dz}{e^z + e^{-T_0/T} - 1}, \tag{2.18}$$

$$I_2 = e^{-T_0/T} \int_0^\infty \frac{z e^z dz}{(e^z + e^{-T_0/T} - 1)^2}. \tag{2.19}$$

The role of S_{pump} in equation (2.16) is that it acts to restore the temperature to E_{ex}/k_B.

2.4.2 LA-PHONON ASSISTED COOLING

The energy relaxation of QW excitons via a bath of bulk LA-phonons is given by [61–64],

$$S_{\text{ph}} = -\frac{2\pi T^2}{\tau_{\text{sc}} T_0}(1 - e^{-T_0/T}) \int_1^\infty \varepsilon \sqrt{\frac{\varepsilon}{\varepsilon - 1}} |F_z(a\sqrt{\varepsilon(\varepsilon - 1)})|^2 \times \frac{e^{\varepsilon E_0/k_{\text{B}}T_b} - e^{\varepsilon E_0/k_{\text{B}}T}}{e^{\varepsilon E_0/k_{\text{B}}T} + e^{-T_0/T} - 1} \frac{1}{e^{\varepsilon E_0/k_{\text{B}}T_b} - 1}. \tag{2.20}$$

where τ_{sc} is the characteristic scattering time,

$$\tau_{\text{sc}} = \frac{\pi^2 \hbar^4 \rho_c}{D_{\text{dp}}^2 M_{\text{x}}^3 \nu_{\text{s}}}. \tag{2.21}$$

Here, ρ_c is the GaAs crystal density, D_{dp} is the deformation potential and ν_{s} is the sound velocity. The form factor F_z originates from an infinite rectangular QW confinement potential:

$$F_z(x) = \frac{\sin(x)}{x} \frac{e^{ix}}{1 - (x/\pi)^2}. \tag{2.22}$$

The dimensionless parameter $a \approx 1$ is given by $a = d_{\text{QW}} M_{\text{x}} \nu_{\text{s}}/\hbar$ where d_{QW} is the quantum well thickness. The derivation of equation (2.20) can be found in Ref. [61].

2.4.3 EVAPORATIVE HEATING

The final term in the thermalisation equation (2.16) is the heating rate due to the decay of low energy excitons from within the light cone. As discussed in the first chapter, only excitons that are low in energy are optically active. The result is an evaporative heating effect - removal of the low energy particles increases the temperature. This is analogous to evaporative cooling which occurs in a variety of systems where usually it is only the highest energy particles that may escape from the main body of the gas. The rate of evaporative heating is given by [45, 48],

$$S_{\text{opt}} = \frac{k_{\text{B}} T I_2/\tau_{\text{opt}}}{2k_{\text{B}} T I_1 - k_{\text{B}} T_0 I_2} T_0. \tag{2.23}$$

The integrals I_1 and I_2 are given in equations (2.18-2.19) and $\tau_{\rm opt}$ is the optical lifetime used in equation (2.3). The effect of evaporative heating is included here for completeness but is generally found to be a rather minor correction to the thermalisation process.

2.5 Optical lifetime and photoluminescence of QW excitons

Since only QW excitons with momentum inside the light cone may decay optically, the optical lifetime $\tau_{\rm opt}$ needs to be calculated accordingly. The temperature and density dependent effective decay rate, $\Gamma_{\rm opt} = 1/\tau_{\rm opt}$ is derived in appendix B. It is given by [61, 63, 65, 66],

$$\Gamma_{\rm opt} = \frac{E_\gamma}{2\tau_r k_{\rm B} T_0} \int_0^1 \frac{1+z^2}{A e^{-z^2 E_\gamma / k_{\rm B} T} - 1}, \tag{2.24}$$

where

$$A = \frac{e^{E_\gamma / k_{\rm B} T}}{1 - e^{-T_0/T}}. \tag{2.25}$$

Here, τ_r is the intrinsic radiative lifetime of ground state QW excitons with zero in-plane momentum. Therefore τ_r depends only on the structure, its composing materials and the electric field applied perpendicular to the QW plane [67, 68]. These are constant for the experiments considered in this chapter. The energy E_γ is the intersection of the exciton and photon dispersion relations and marks the upper bound in energy for which two-dimensional excitons may decay to emit light. To illustrate, Fig. 2.3 shows the effective optical lifetime $\tau_{\rm opt}$ plotted as a function of temperature for various densities. The lifetime is only weakly density dependent. Above 1 K, it decreases linearly with decreasing temperature but saturates to $2\tau_r = 40$ ns at low temperatures. The PL intensity, $I_{\rm PL}$ which results from decaying excitons is given by

$$I_{\rm PL} = \Gamma_{\rm opt} n_{\rm x}. \tag{2.26}$$

The spatial profile of $I_{\rm PL}$ is directly comparable with experimental measurements of the indirect exciton emission.

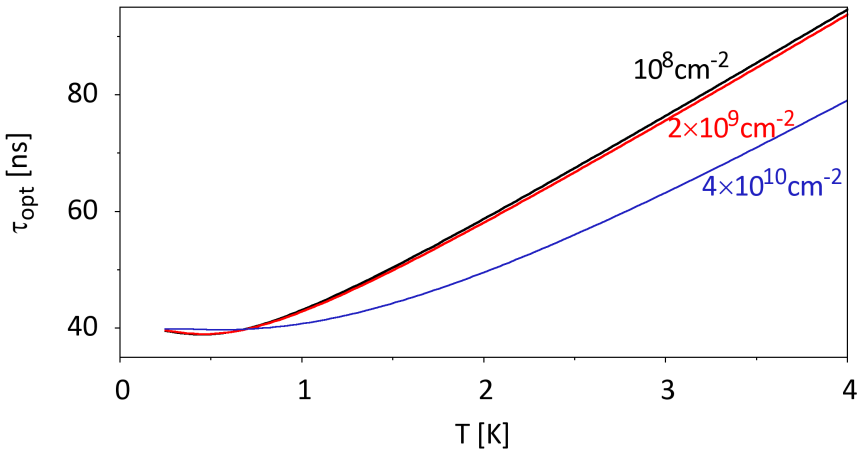

Figure 2.3: Indirect exciton lifetime as a function of temperature for various exciton densities.

2.6 Numerical methods for solving the coupled transport and thermalisation equations

The set of coupled equations to be solved is

$$\frac{\partial n_{\mathrm{x}}}{\partial t} = \nabla G \cdot \nabla n_{\mathrm{x}} + G\nabla^2 n_{\mathrm{x}} + \Lambda - \Gamma_{\mathrm{opt}}(n_{\mathrm{x}}, T) n_{\mathrm{x}}, \tag{2.27}$$

$$\frac{\partial T}{\partial t} = S_{\mathrm{pump}}(n_{\mathrm{x}}, T; \Lambda, E_{\mathrm{ex}}) + S_{\mathrm{ph}}(n_{\mathrm{x}}, T; T_b) + S_{\mathrm{opt}}(n_{\mathrm{x}}, T), \tag{2.28}$$

where the function $G = G(n_{\mathrm{x}}, T)$ is given by

$$G = D(n_{\mathrm{x}}, T) + u_0 \mu(n_{\mathrm{x}}, T) n_{\mathrm{x}}. \tag{2.29}$$

The system of equations was solved numerically using a finite difference scheme. This is done by discretising the transport equation onto a grid of uniformly spaced points. At each point, the derivatives are approximated using a low order Taylor expansion as follows:

$$n(r+\delta r) = n(r) + \delta r \frac{\partial n}{\partial r} + \frac{\delta r^2}{2}\frac{\partial^2 n}{\partial r^2} + ..., \tag{2.30}$$

$$n(r-\delta r) = n(r) - \delta r \frac{\partial n}{\partial r} + \frac{\delta r^2}{2}\frac{\partial^2 n}{\partial r^2} + ... \tag{2.31}$$

Subtracting equation (2.31) from (2.30), one gets

$$\left(\frac{\partial n}{\partial r}\right)_{r=r_i} \approx \frac{n_{i+1} - n_{i-1}}{2\delta r}, \tag{2.32}$$

and adding,

$$\left(\frac{\partial^2 n}{\partial r^2}\right)_{r=r_i} \approx \frac{n_{i+1} + n_{i-1} - 2n_i}{\delta r^2}. \tag{2.33}$$

where $n_i = n(r_i)$ and $r_i = i\delta r$ with $i \in \aleph$. The first and second derivatives of a radially symmetric function $f(r)$ may be written in matrix form:

$$\frac{\partial f}{\partial r} = \frac{\mathrm{D}^{(1)}}{\delta r}\mathbf{f}, \qquad \frac{\partial^2 f}{\partial r^2} = \frac{\mathrm{D}^{(2)}}{(\delta r)^2}\mathbf{f}. \tag{2.34}$$

where

$$\mathrm{D}^{(1)} = \begin{pmatrix} 0 & 0 & 0 & 0 & \cdots & 0 \\ -1 & 0 & 1 & 0 & \cdots & 0 \\ 0 & -1 & 0 & 1 & \cdots & 0 \\ \vdots & \vdots & \ddots & \ddots & \ddots & \vdots \\ \vdots & \vdots & & -1 & 0 & 1 \\ 0 & 0 & \cdots & 0 & 0 & 0 \end{pmatrix} \text{ and } \mathrm{D}^{(2)} = \begin{pmatrix} -4 & 4 & 0 & 0 & \cdots & 0 \\ 1 & -2 & 1 & 0 & \cdots & 0 \\ 0 & 1 & -2 & 1 & \cdots & 0 \\ \vdots & \vdots & \ddots & \ddots & \ddots & \vdots \\ \vdots & \vdots & & 1 & -2 & 1 \\ 0 & 0 & \cdots & 0 & 2 & -2 \end{pmatrix} \tag{2.35}$$

2.6.1 STEADY STATE SOLUTION

For simulations where only the final steady state solution is sought, the time derivatives on the left hand side of (2.27) and (2.28) are set to zero. Then, using the finite difference approximations of the spatial derivatives, the transport equation can be expressed in matrix form as

$$A(\mathbf{n}_\mathrm{x})\mathbf{n}_\mathrm{x} = -\mathbf{\Lambda}, \tag{2.36}$$

where

$$A_{ij} = (\mathrm{D}^{(1)}\mathbf{G}(\mathbf{n}_\mathrm{x}, \mathbf{T}))_i \mathrm{D}^{(1)}{}_{ij} + (\mathrm{G}(\mathbf{n}_\mathrm{x}, \mathbf{T}))_i (\frac{\mathrm{D}^{(1)}{}_{ij}}{r_i} + \mathrm{D}^{(2)}{}_{ij}) - \Gamma_i \delta_{ij}. \tag{2.37}$$

$\mathbf{n}_\mathrm{x} = (n_0, n_1, ..., n_N)$ and $\mathbf{\Lambda} = (\Lambda_0, \Lambda_1, ..., \Lambda_N)$ are the densities and generation rates at each grid point respectively and $(\mathbf{G}(\mathbf{n}_\mathrm{x}, \mathbf{T}))_i = G(n_i, T_i)$. For a given temperature profile $T(r)$, equation (2.36) may be solved for the density distribution n_x using a standard Newton-Raphson library routine. Next, n_x is plugged into equation (2.28) which is solved as a transcendental equation at each grid point for $T_i = T(r_i)$. This process is repeated - equation (2.36) is solved again using the new temperature profile to find a new density profile and so on. Iterating a few tens of times allows the density and temperature profiles to converge to high accuracy. Convergence is quantified by the following two error functionals:

$$e_1 = \Sigma_{i=0}^{N} \left| (A(\mathbf{n}_\mathrm{x})\mathbf{n}_\mathrm{x})_i + \Lambda_i \right|, \tag{2.38}$$

$$e_2 = \Sigma_{i=0}^{N} \left| S_\mathrm{pump}(n_{\mathrm{x}_i}, T_i; \Lambda_i, E_\mathrm{ex}) + S_\mathrm{ph}(n_{\mathrm{x}_i}, T_i; T_b) + S_\mathrm{opt}(n_{\mathrm{x}_i}, T_i) \right|. \tag{2.39}$$

The convergence criteria used was that both e_1 and e_2 were required to be less than 10^{-5}.

2.6.2 Dynamic solution

Where it was required that the time evolution of the density and temperature distributions was known (in the modeling of the PL-jump for example), an explicit finite difference scheme in the time domain was used [69]. To do this, the time derivative is approximated by

$$\frac{\partial n}{\partial t} \approx \frac{n(t + \delta t, r) - n(t, r)}{\delta t}. \tag{2.40}$$

For sufficiently small δt, the density and temperature profiles can be evolved to a time t from some initial conditions at $t = 0$ by iterating the following equation,

$$\mathbf{n}_\mathrm{x}^{(\mathbf{k+1})} = \mathbf{n}_\mathrm{x}^{(\mathbf{k})} + \frac{\delta t}{(\delta x)^2} \left[\nabla G(\mathbf{n}_\mathrm{x}^{(\mathbf{k})}, \mathbf{T}^{(\mathbf{k})}) \cdot \nabla \mathbf{n}_\mathrm{x}^{(\mathbf{k})} + G(\mathbf{n}_\mathrm{x}^{(\mathbf{k})}, \mathbf{T}^{(\mathbf{k})}) \nabla^2 \mathbf{n}_\mathrm{x}^{(\mathbf{k})} \right] \tag{2.41}$$

$$+ \delta t \left[\mathbf{\Lambda} - \Gamma_\mathrm{opt}(\mathbf{n}_\mathrm{x}^{(\mathbf{k})}, \mathbf{T}^{(\mathbf{k})}) \mathbf{n}_\mathrm{x}^{(\mathbf{k})} \right]. \tag{2.42}$$

Here, the index $k \in \aleph$ refers to the time domain (i.e. $t = k\delta t$). Each successive density and temperature profile is found from the previous iteration. The accuracy and stability of the solution is determined by the dimensionless constant $D_\mathrm{x}^{(0)} \delta t / (\delta x)^2$. A value of 10^{-3} was used throughout the following results section. The method of finding the dynamic solution is much simpler to implement than the method used

to find steady state solutions. However, the computation required for the dynamic solution is significantly greater. This is due to the very small time step, δt that is needed for stability. Further, the computation time scales with $1/(\delta x)^3$.

Other methods were tried including the Crank-Nicolson implicit method [69]. The idea behind that scheme is that a much greater time step may be used by making a more accurate approximation of the time derivative. However, in the case of such strongly non-linear terms found in this set of equations, a small time step is always needed. This causes the Crank-Nicolson method to be even slower in this case due to the increased work needed on each time step.

2.6.3 NUMERICAL INTEGRATION

To compute the integrals in equations (2.18), (2.19), (2.20) and (2.24), an adaptive Simpson algorithm was used. This method of quadrature uses an estimate of the error from calculating a definite integral by the standard Simpson's rule. Where the error exceeds a given tolerance, the interval of integration gets subdivided into two and the algorithm gets applied again to each subinterval. This recursive method is much faster and more efficient for evaluating integrals as it uses fewer function evaluations in places where the integrand is well approximated by a cubic function.

2.7 RESULTS

The results obtained in these studies are presented in three parts. First, the formation of the inner ring following activation of the laser is discussed. The density, temperature and PL dynamics during the few tens of nanoseconds taken for the inner to form are shown. The inner ring has been studied previously but only by examining the steady state PL pattern [45]. No studies of the dynamics of its formation had been done previously. Next, the excitation energy dependence of the inner ring is calculated for the steady state. Finally the dynamics of the PL-jump are examined in detail. In contrast to the results presented here, previous studies of the PL-jump were done without spatial resolution [70]. In all cases, quantitative comparisons are made with the available experimental data.

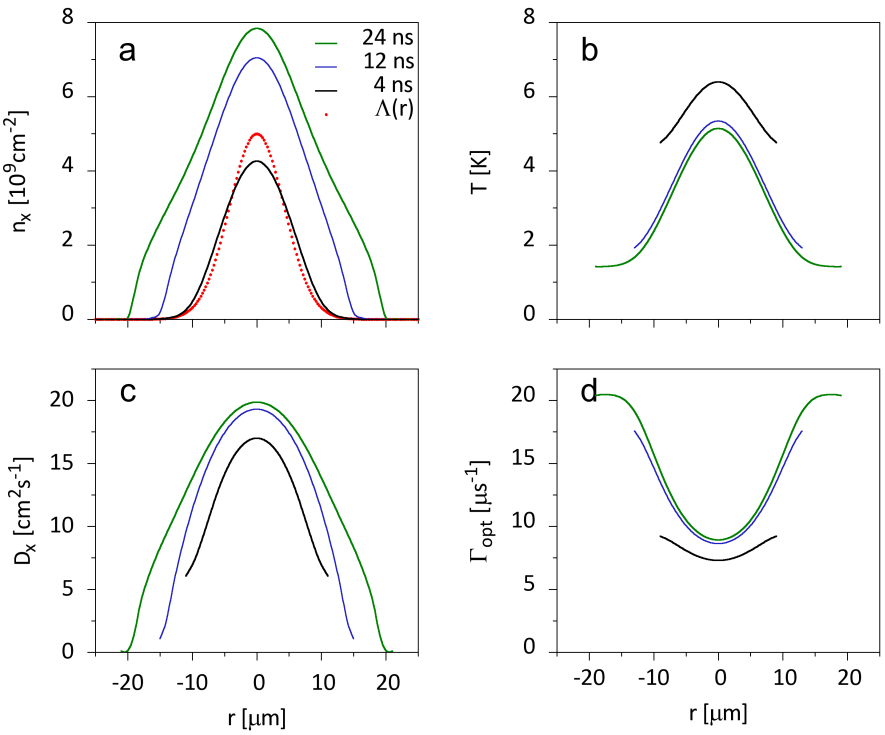

Figure 2.4: Simulations of the formation of the exciton inner ring. Spatial profiles at various time delays following laser onset of the indirect exciton density (a), temperature (b), diffusion coefficient (c) and decay rate (d). The laser excitation profile is shown by the dotted line in (a).

2.7.1 Formation of the inner ring

Fig. 2.4 shows numerical solutions to the coupled transport and thermalisation equations (2.27) and (2.28) subject to a point laser excitation. In Fig. 2.4a, the exciton density distribution is shown. It can be seen that within 30 ns, excitons diffuse tens of micrometers away from the excitation spot. Such rapid diffusion occurs because for high densities, QW disorder is strongly screened by exciton-exciton interaction leading to a larger diffusion coefficient. The diffusion coefficient is plotted in Fig. 2.4c. The sharp contrast in density for large values of r is a consequence of the reduction in diffusion coefficient as QW disorder is not as effectively screened for lower densities. Temperature profiles of the system are given in Fig. 2.4b. Inside the excitation spot, the profile closely follows that of the generation rate Λ (red dotted line in Fig. 2.4a). Outside the excitation spot, excitons are in thermal equilibrium with the lattice which is at the helium bath temperature $T_b = 1.4\,\mathrm{K}$. The effect of temperature on the exciton decay rate, Γ_{opt} is seen in Fig. 2.4d. At the excitation spot, heating due to the laser suppresses decay and hence the PL intensity is reduced. The absence of

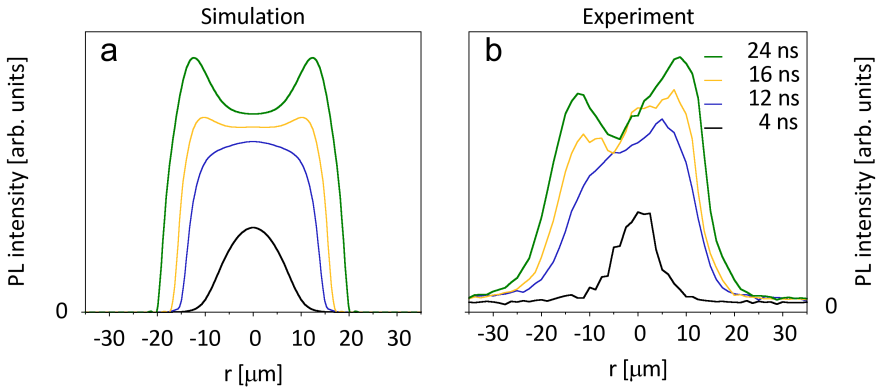

Figure 2.5: Simulated (a) and observed (b) profiles of the inner ring in the exciton PL pattern during its formation.

T and Γ_{opt} data for large r is because these quantities are not defined for $n_{\text{x}} = 0$. Suppression of the optical decay results in the formation of a bright ring in the PL pattern around the excitation spot as shown in Fig. 2.5a. Data obtained from experiment [48] is presented for comparison in Fig. 2.5b. The light emitted from the CQWs was collected with 4 ns time resolution. All basic parameters of the model were chosen to match experimental conditions and the fit parameters were used to give the best agreement between experimental and simulated data. A good agreement between Figs. 2.5a and 2.5b is clearly seen.

To further clarify the physics of the inner PL ring, the time dependence of the same quantities are plotted in Fig. 2.6. Each curve shows the simulated dynamics and corresponds to different radial positions. Following the onset of the laser excitation at $t = 0$, Fig. 2.6c illustrates the rapid thermalisation of initially hot indirect excitons. The gradual build-up of the density is shown in Fig. 2.6a. The exciton density saturates as the rate at which excitons optically decay, which is proportional to the density, becomes equal to the generation rate. The monotonic decrease in time of the optical lifetime τ_{opt} is because of the cooling of indirect excitons (compare Figs. 2.6b and 2.6d). The final steady-state value of the optical lifetime decreases with increasing r because the laser induced heating of the exciton system decreases with the radial distance from the laser spot center. The initial rapid decrease in the diffusion coefficient D_{x} originates from the thermalisation of the exciton system. Initially hot excitons are not bound by the QW disorder potential. As they cool, a large fraction become localised in potential minima and do not contribute to transport. Following the thermalisation transient, the exciton density n_{x} increases leading to screening of the disorder potential and a corresponding increase in the diffusion coefficient.

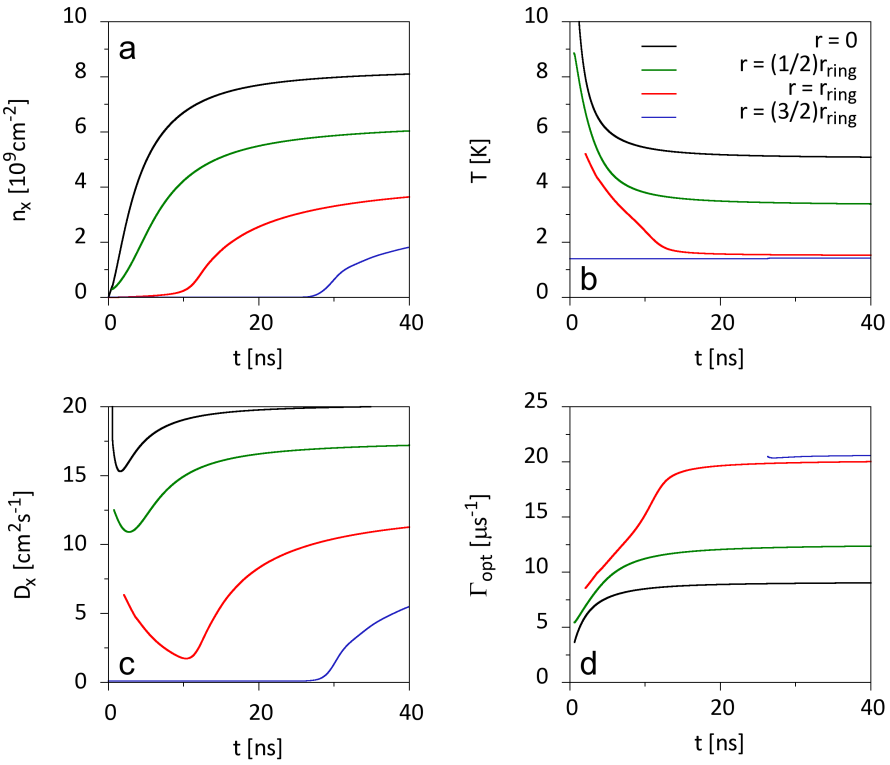

Figure 2.6: Dynamics of the inner ring formation. The time dependence of the indirect exciton density (a), temperature (b), diffusion coefficient (c) and decay rate (d) are plotted for different radial positions.

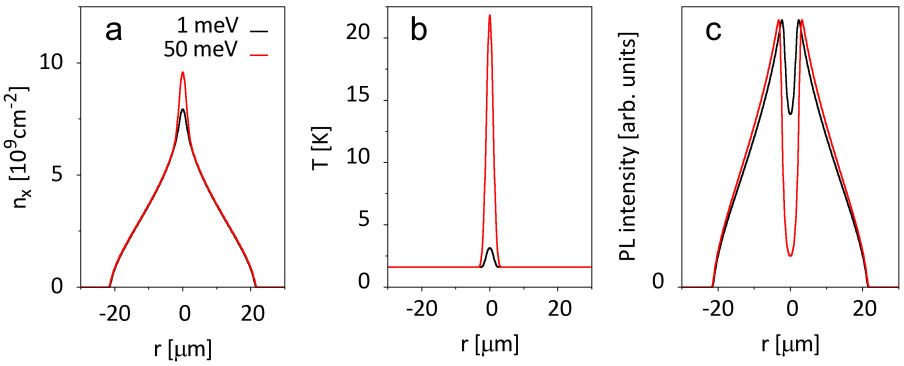

Figure 2.7: Simulated density (a), temperature (b) and PL signal (c) of excitons subject to laser excitation at two different energies.

2.7.2 EXCITATION ENERGY DEPENDENCE OF THE INNER RING

As discussed, the PL intensity reduction at the center of the inner ring is due to a higher indirect exciton temperature in the region of laser excitation. This, in turn, causes a reduction in the radiative decay rate and leads to the formation of the inner ring. The laser induced heating, which is determined by the excess in-plane kinetic energy of photo excited excitons, controls the contrast of the inner ring. Therefore, studying the excitation energy dependence of the inner ring contrast provides a means to measure the laser induced heating dependence on excitation energy. Here, this dependence is calculated and compared to experimental observations.

In the presented model, the excitation energy is included via E_{ex} which appears in the laser induced heating term S_{pump} (See equation (2.17)). The energy E_{ex} is the excess energy acquired by an exciton during its creation from an unbound electron-hole pair. Following its creation, the exciton relaxes in energy by the emission of LA-phonons and through exciton-exciton scattering. On the sub-ns timescales during its formation, an exciton may also relax via the emission of longitudinal-optical (LO) phonons. This is provided that its initial energy exceeds the LO-phonon energy of $E_{\mathrm{LO}} = 36\,\mathrm{meV}$. Energy relaxation via LO-phonon emission is rapid and can be thought of as part of the initial exciton formation process. Therefore, we may assert an upper limit on the excess exciton energy, $E_{\mathrm{ex}} \leq E_{\mathrm{LO}}$.

Fig. 2.7 shows two steady-state solutions of equations (2.27) and (2.28) for different excitation energies. The excitation geometry is the same as in the previous section. The density distribution (Fig. 2.7a) is mostly unaffected by the change in the E_{ex}. This is because the heating is restricted to within the excitation spot. Outside

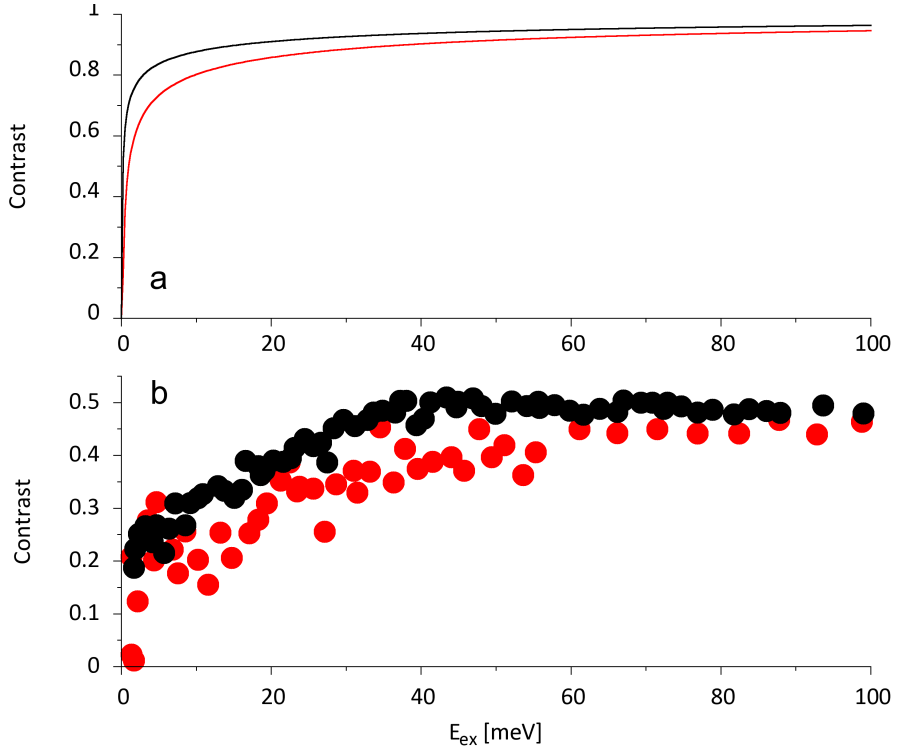

Figure 2.8: Simulated (a) and measured (b) excitation energy dependence of the contrast of the exciton inner ring.

the excitation spot, the exciton gas is in thermal equilibrium with the lattice. The density at the center of the excitation spot is slightly increased because of an increase in the exciton lifetime.

The temperature profile, plotted in Fig. 2.7b, shows a great increase at the excitation spot due to the laser induced heating. The temperature increase suppresses further the optical decay and enhances the contrast of the inner ring in the PL pattern, plotted in Fig. 2.7c. A greater excess energy of photo excited excitons increases the contrast of the inner ring. The inner ring contrast may be quantified by $C = (I_{\max} - I_{\min})/I_{\max}$ where $I_{\max}$ and $I_{\min}$ are the PL intensities at the ring position and the center of the excitation spot respectively. In Fig. 2.8a, the contrast is plotted against E_{ex} for two different exciton generation rates. Fig. 2.8b shows the experimentally measured contrast of the inner ring [49] for two excitation powers. The laser excitation energy, E_ω relates to the excess energy by $E_\omega = E_{\text{ex}} + E_g - E_b$ and $E_{\text{ex}} = 0$ corresponds to the heavy-hole direct exciton energy.

Fig. 2.8 shows a qualitative agreement between the measured and simulated

dependence of the inner ring contrast on excitation energy. In both cases, the contrast increases with photon energy due to the increasing exciton temperature within the excitation spot. However, in the experimental data, the contrast saturates at a lower value of about 0.5 compared to about 0.9 in simulations. To make a more quantitative comparison requires some additions to the theory like, for example, the exciton relaxation by emission and absorption of optical phonons is required. This study shows that tuning the laser to the heavy-hole direct exciton resonance drastically reduces the laser induced heating of the exciton gas. It was also seen in the experimental data that this resonance coincided with a peak in the indirect exciton population (not shown here). Therefore, it can be concluded that this is the optimal laser energy for creating a degenerate exciton gas since it achieves the highest density and lowest temperature.

2.7.3 The PL-jump

The temporal counterpart of the inner ring is the PL-jump. Just as the indirect exciton PL intensity increases with increasing spatial separation from the laser, it also increases for separation in time. A massive increase in the PL intensity occurs in the few nanoseconds following termination of the laser. Therefore, this effect is called the PL-jump.

Fig. 2.9 shows the exciton kinetics after laser termination. Without heating by the laser ($S_{\text{pump}} = 0$), the population is allowed to thermalize with the lattice (see Fig. 2.9a). Although the system is heated by exciton decay as discussed earlier in the chapter, its effect is relatively weak compared to the highly efficient cooling by phonon interactions. Within 2 ns, the temperature at the excitation spot drops close to the lattice temperature. Consequently, the decay rate, Γ_{opt} shown in Fig. 2.9c, increases considerably and the large population of excitons at the excitation spot begins a fast optical decay shown in Fig. 2.9b. The resulting PL-jump is seen in Fig. 2.9d. The intensity approximately doubles in magnitude before beginning exponential decay.

Some previous experiments which revealed the PL-jump were performed without spatial resolution. The comparisons with the time-resolved imaging presented here confirm the prediction of the theory that the PL jump is observed predominantly within the excitation spot where the laser induced heating is at its maximum. Fig. 2.10 a and b show the spatial PL profiles during the PL-jump from theory and

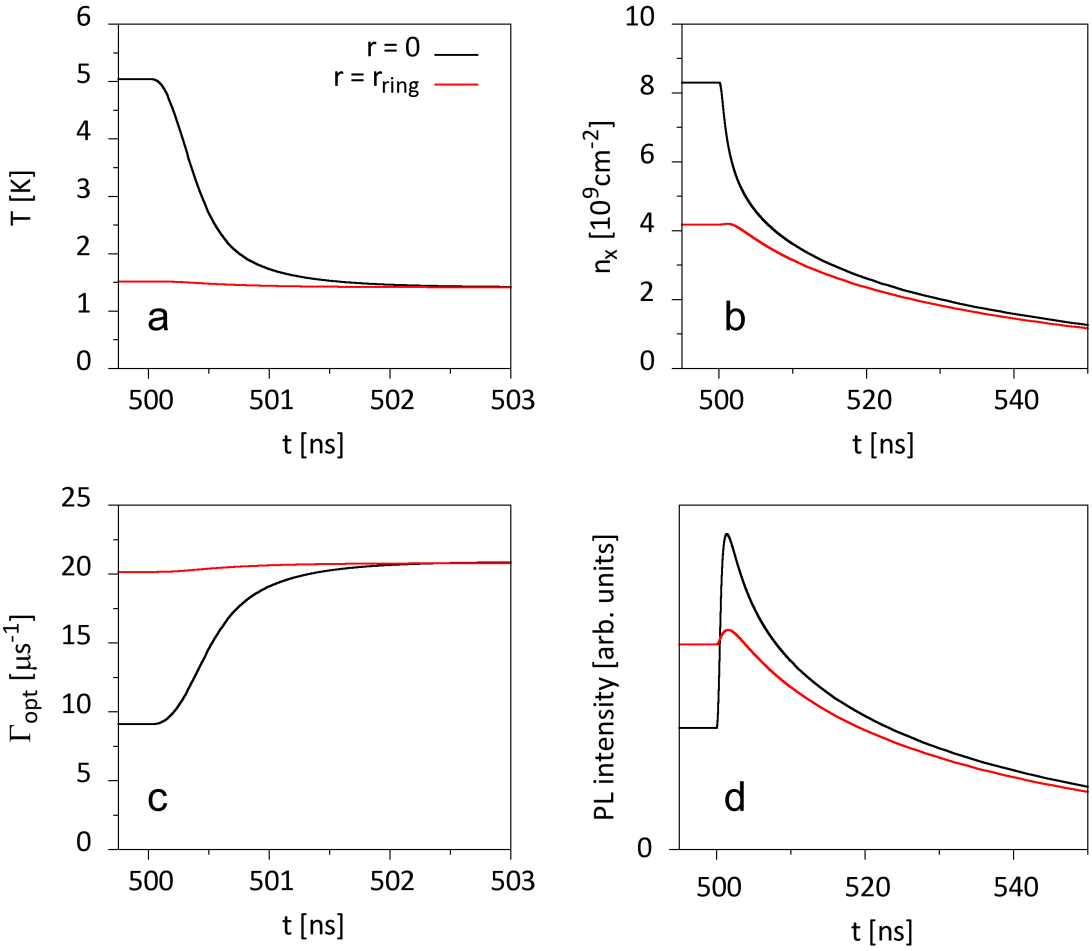

Figure 2.9: Dynamics of the PL-jump. Time dependence of the indirect exciton temperature (a), density (b), decay rate (c) and PL intensity (d) following termination of the laser at $t = 500\,\text{ns}$. The black and red curves correspond to the excitation spot and ring position respectively.

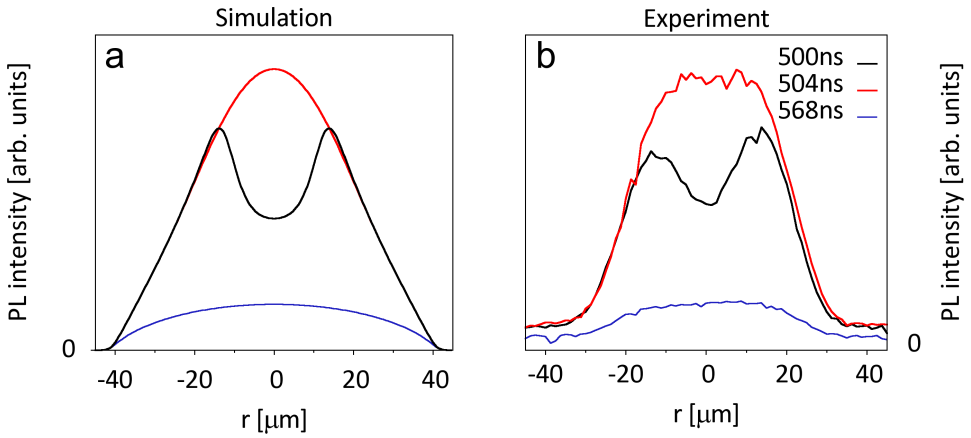

Figure 2.10: Simulated (a) and observed (b) cross sections of the exciton inner ring at different time delays following laser termination.

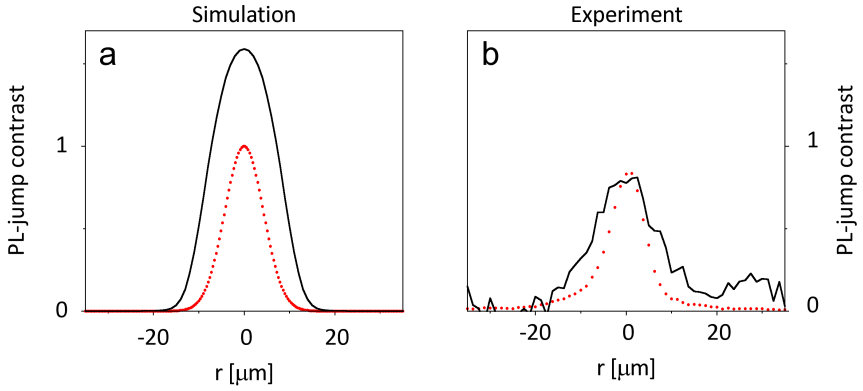

Figure 2.11: Simulated (a) and measured (b) spatial dependence of the PL-jump contrast. The laser excitation profile is shown by the red dotted line.

experiment respectively. Within the 4 ns time resolution of the experiment, excitons cool to the lattice temperature $T_b = 1.4$ K and the PL intensity reaches its maximum. The difference in the PL signal from just before and just after laser termination is greatest at the excitation spot. Far from the laser where the excitons are already well thermalised to the lattice temperature, the difference in the PL signal is negligible. Both the experimental data and calculations demonstrate that the exciton cooling time to the lattice temperature is much shorter than the exciton lifetime. This feature is further clarified by plots of the spatial dependence of the PL-jump contrast shown in Fig. 2.11. The PL-jump contrast is defined as $(I_{max} - I_{on})/I_{on}$ for each radial position r where I_{max} is the maximum PL intensity during the PL-jump and I_{on} is the PL intensity before laser termination. The discrepancy between theoretical (Fig. 2.11a) and measured (Fig. 2.11b) results is due to the limited temporal resolution of the imaging device. The experimental data is consistent with the model used.

2.7.4 FIT PARAMETERS

Numerical simulations using the model based on transport, thermalisation and photoluminescence of indirect excitons quantitatively reproduces the experimental data. This is true for the following fitting parameters which can be inferred from this study: $U_0 = 0.7\,\mathrm{meV}$, $D_{\mathrm{x}}^{(0)} = 30\,\mathrm{cm^2 s^{-1}}$, $\Lambda_0 = 2 \times 10^9\,\mathrm{cm^{-2} ns^{-1}}$ and $E_{\mathrm{ex}} = 12.9\,\mathrm{meV}$. Although four fitting parameters were used, the procedure is well justified: (i) the whole set of the experimental data, measured at various r and t are modeled with the same values of the control parameters and (ii) the fitting parameters influence different aspects of the transport and PL processes in a separate way and are inferred independently. The pump rate Λ_0 yields a maximum concentration which can be evaluated from the blue shift of the PL line. The average energy of incoming, hot indirect excitons, E_{ex}, governs the contrast of the inner ring and PL-jump. The input diffusion coefficient, $D_{\mathrm{x}}^{(0)}$, determines the time-dependent radius of the inner PL ring. Finally, the amplitude, U_0, of the long-range correlated disorder potential is responsible for the spatial pinning of the PL signal at ring edges. Note that the above values of the control parameters are consistent with those used in previous works on the steady-state inner ring [45] and laser-induced traps [9] studied for the same CQW structures. Table 1.1 in the introduction lists all other basic known parameters used in the model.

2.8 SUMMARY

In this chapter, a study of the kinetics of the inner ring and the PL-jump in the exciton emission pattern were presented. A theoretical model concerning the creation, transport, thermalisation and optical decay of excitons was described. The model includes the non-classical, quantum-statistical effects in its description. All the main features of the inner ring and PL-jump are described within this model.

The appearance of the inner ring was attributed to the relaxation in energy of excitons as they drift away from the region of laser induced heating at the excitation spot. The model quantitatively predicts the experimentally measured time-dependent PL profiles of the formation of the inner ring following the onset of laser excitation.

The excitation energy dependence of the inner ring contrast was also studied. Increasing the excess energy of photoexcited excitons leads to increased heating at the

excitation spot. This enhances the inner ring contrast which is an observable quantity. The monotonic increase in contrast with increasing excess energy is confirmed by the experimental data. There, the excess energy increases with energy of photons injected into the CQWs.

Finally, the PL-jump was explained by rapid cooling of a dense exciton gas following the termination of the laser excitation. Within 2 ns, the excitons reach thermal equilibrium with the lattice and become optically active. The sharp decrease in optical lifetime leads to the sharp jump in emission intensity and subsequent rapid decay of the exciton density. The contrast of the PL-jump is found to be at its maximum in the region of laser excitation. The results from simulation are in good agreement with the available experimental data.

3 Indirect excitons in applied in-plane potentials

3.1 Background

As discussed in the introduction, an inhomogeneous charge distribution above the quantum well layers exerts a force on dipole orientated excitons. Although the overall charge of an indirect exciton is zero, the charge in the upper layer closest to the electrode will experience a stronger attractive force than the repulsive force felt by the charge in the lower layer. This means that where there is an electrode, there will be a minimum in the exciton potential in the QW plane beneath it. Therefore, indirect excitons tend to accumulate beneath the electrodes [30].

Quite complex electrode patterns attached to CQW samples are now routinely achieved [38]. Further, many electrodes at different voltages can be realised. The voltage at each electrode, which controls the depth of the exciton potential, may also be time varying so as to create dynamic potentials [39]. Such flexibility has enabled a range of experiments in which the transport properties of excitons can be probed. This has motivated the theoretical studies presented in this chapter. An outline of the progress thus far in this avenue of research is given here.

3.1.1 TRAPS

Motivated by the desire to observe exciton BEC, several groups have engineered methods to spatially confine indirect excitons to potential traps. Without trapping, an indirect exciton gas rapidly expands due to the strong dipole-dipole repulsion. Since the exciton quantum degeneracy temperature is proportional to density, it can be elevated by means of a potential trap. Then, a degenerate exciton gas becomes accessible for cryostat temperatures of a few Kelvin.

Trapping of indirect excitons by spatial modulation of the gate voltage has been demonstrated in Refs. [31, 71–73]. An obstacle for effective trapping of excitons is that of exciton ionization which is induced by high in-plane electric fields. For an in-plane field $F_{||} > E_b/a_x$ where E_b and a_x are the exciton binding energy and Bohr radius respectively, an exciton is torn apart as its electron and hole constituents are pulled in opposite directions. Ionization is particularly likely to occur near the electrode edges where gradients in the exciton potential are greatest. A simple solution to this problem was achieved by placing the CQWs much closer to the homogeneous bottom electrode than the shaped top electrode [31]. This has the effect of smoothing the potential landscape to prevent ionization whilst at the same time preserving the approximate shape of the potential as well as its depth.

More accurate control over the form of the potential was shown in Ref. [32] where a parabolic trapping was demonstrated by using a diamond-shaped electrode. Also, in Ref. [33] a '*chute trap*' was developed to pre-cool excitons as they traveled towards the center of the trap. In more recent work [14, 15], spontaneous coherence of indirect excitons is claimed to have been observed in a parabolic trapping potential.

Another technique for creating electrostatic excitonic traps is by patterning SiO_2 layers between the electrode layer and the GaAs heterostructure as was done in Refs. [34, 43, 74]. Indirect excitons became trapped in the CQWs along the perimeter of the SiO_2 layers. The confinement was explained via the electrostatic influence of surface states in the GaAs/SiO_2 interface.

Confining potentials for excitons are also realised by stress traps [75, 76, 76–78]. An inhomogeneous force is applied to the samples, normal to the QW plane. The stretching of the sample causes a reduction in the exciton potential. Excitons therefore accumulate beneath point of contact between the sample and a stressor.

Other methods of trapping excitons to high density include natural traps [11] where excitons are confined to the defects intrinsic to CQWs, optical traps [79, 80] where excitons are confined by light and magnetic traps [81]. A commonly observed effect in many of these experiments is the localisation-delocalisation transition [36]. For moderate densities, excitons are localised to trap centers. However, for high enough densities, it has been found that excitons can screen the trapping potential because of the dipole-dipole repulsion. Then, a large fraction of the exciton population is delocalised - they are not confined to the trap but instead can diffuse across the QW plane unimpeded by the applied potential.

3.1.2 Narrow channels

Electrostatic traps like those described in the previous section have also been engineered to cause strong confinement of excitons in one dimension only. This has been done by the patterning of thin electrodes onto the CQW sample [42] and also using SiO_2 layers [34, 43]. In either case, one has narrow potential channels or wires along which excitons propagate. In Ref. [43], it was found that exciton diffusion is greatly enhanced in a narrow channel over regular two-dimensional diffusion. The ability to channel energy between point locations in the QW plane by using indirect excitons in narrow channels also has great potential for optical device applications. A study of this was done in Ref. [42] where control of exciton fluxes in narrow channels was utilized to form a simple integrated circuit.

3.1.3 Elevated traps

Some attempts to create an exciton condensate have been made by following similar methods to those used in atomic physics. The study of cold Bosonic atoms led to the first observation of a BEC in 1995 [4]. Many of the landmarks leading to the discovery came from new techniques developed to remove energy from an atomic gas so as to lower its temperature below the critical BEC temperature. One method to do this, which has since been employed in an attempt to reduce the exciton temperature below the cryostat temperature, is evaporative cooling. This has been done by placing excitons in an elevated trap [35]. In an elevated trap, only the highest energy excitons can diffuse beyond the edges of the trap. The excitons which

escape are then accelerated away from the trap leaving behind only the lowest energy excitons and thus reducing the temperature of the remaining population.

3.1.4 RAMPS

An excitonic ramp is a linear slope in the exciton potential energy. It presents a means to probe the exciton drift current and can be used to experimentally determine the exciton mobility. In Refs. [37, 41], results from time-of-flight experiments are done for exciton transport along a ramp. In that work, the ramp was created by a resistive electrode with a voltage drop across it and was tens of micrometers in length. However, the voltage difference between the ends of the electrode induced a current which can heat the lattice and, in turn, the exciton gas. This factor can strongly affect estimates of the temperature dependent exciton mobility. Ramps can also be created simply by using a shaped electrode at constant voltage. A narrower electrode contains fewer charges per unit of distance along the ramp and therefore creates a shallower trapping potential. As the electrode widens, the trapping potential increases and the exact shape of the electrode can be chosen to give a linear gradient in the exciton potential. However, a ramp made in this way can only be quite small in length which therefore makes time-of-flight experiments difficult to perform. Numerical studies of exciton transport on a ramp created by a patterned electrode are presented later in this chapter and also in Ref. [40].

3.1.5 LATTICES

Further insight into the transport characteristics of indirect excitons is gained by studying excitons in electrostatic lattices. In this context, the electrostatic lattice is an applied electric potential that is periodic in one or both of the in-plane coordinates. In Ref. [36], a one-dimensional lattice was studied. Similar to the trap potentials discussed above, a localisation-delocalisation transition was observed for high exciton density or low amplitude of the lattice potential. In Ref. [37], a similar one-dimensional lattice was investigated and an ac voltage was applied to the electrodes to demonstrate shuttling of excitons back and forth as the positions of minima in the lattice potential oscillated. Various two-dimensional lattices were also studied in Ref. [38]. Shown later in this chapter are theoretical studies of exciton transport in

one-dimensional moving lattice - a *conveyer* [39]. In a conveyer, excitons localise to the minima of the lattice potential and are then dragged several tens of micrometers from the excitation spot as the conveyer propagates across the QW plane. The conveyer realises highly controlled transport of excitons similar to how a charge coupled device realises controlled transport of electrons.

3.1.6 Switches

Although much of the motivation that drives the research of exciton physics comes from the potential to study BEC, there is now also the possibility to utilize excitons for device applications. In the quest to achieve BEC in an exciton system, a wealth of knowledge has accumulated. With some ingenuity, this can be used in device applications. An example of this are excitonic optoelectronic transistors [82, 83] where the electrically controlled on/off switching of an optical signal is mediated by indirect excitons. Another example is an all-optical excitonic transistor [84] where the switching of light is controlled using only light by taking advantage of excitons as an operating medium. In all of these devices, the exciton transport is controlled via applied in-plane electrostatic potentials which is the focus of this chapter.

3.2 In-plane exciton potential due to patterned electrodes

In order to make a good estimate of the indirect exciton in-plane potential, excitons may be treated as point-like rigid dipoles. In this case, the potential $u = u(x, y)$ due to a single electron on the sample surface is given by

$$u(x,y) = \frac{e^2}{2\pi\varepsilon_0\varepsilon_r}\left[\frac{1}{\sqrt{x^2+y^2+d_{\text{elec}}^2}} - \frac{1}{\sqrt{x^2+y^2+(d_{\text{elec}}+d_z)^2}}\right], \tag{3.1}$$

where d_{elec} is the distance between the QWs and the electrode layers and d_z is the dipole length. x and y are the in-plane coordinates. The total potential $V(x, y, t)$ is given by the integral over the entire electrode pattern:

$$V(x,y,t) = \int\int u(x-x', y-y')\rho(x', y', t)dx'dy', \tag{3.2}$$

where $\rho(x, y, t)$ is the time-dependent charge density distribution in the electrodes. The potential is included into the exciton transport equation via the drift term. The transport equation is

$$\frac{\partial n_{\mathrm{x}}}{\partial t} = \nabla \cdot [D_{\mathrm{x}} \nabla n_{\mathrm{x}} + \mu_{\mathrm{x}} n_{\mathrm{x}} \nabla (u_0 n_{\mathrm{x}} + V)] + \Lambda - \frac{n_{\mathrm{x}}}{\tau_{\mathrm{opt}}}. \tag{3.3}$$

This equation describes the in-plane transport of a gas of dipolar excitons under the influence of an external electric field applied via patterned electrodes on the sample surface above the QWs.

3.3 EXCITON LIFETIME DEPENDENCE ON VELOCITY

As discussed in chapters one and two, only excitons with energies inside the photon cone may decay optically. A high drift velocity, which can potentially be caused by the applied in-plane electric fields, can affect the optical lifetime of two-dimensional excitons. The momentum distribution may be shifted such that a smaller fraction of excitons sit within the photon cone and are optically active. These effects can be included into the model using the following expression for the optical lifetime of excitons which is a modified form of equation (2.24), derived in appendix B,

$$\frac{1}{\tau_{\mathrm{opt}}} = \frac{E_\gamma}{4\pi\tau_r k_{\mathrm{B}} T_0} \int_{z_{\mathrm{a}}}^{1} dz \int_0^{2\pi} d\phi \frac{1+z^2}{A \exp[E_\gamma (1 - z^2 + y - 2\sqrt{y(1-z^2)}\cos\phi)/k_{\mathrm{B}}T] - 1}. \tag{3.4}$$

Here, E_γ is the energy marking the crossover between the exciton and photon dispersions, τ_r is the intrinsic exciton lifetime and $A = (1 - e^{T_0/T})^{-1}$. The dimensionless parameter, y, in the integral is calculated from v_g, the group velocity of the excitons, $y = E_d/E_\gamma$ with $E_d = \frac{1}{2} M_{\mathrm{x}} v_g^2$. To calculate optical decay, $z_{\mathrm{a}} = 0$ is used for the lower limit of integration in equation (3.4). The PL pattern collected by the detector is also calculated using equation (3.4) but with $z_{\mathrm{a}} = \sqrt{1 - \sin^2(\theta_c/2)}$ where θ_c is the collection angle of the detector.

In Fig. 3.1, τ_{opt} is plotted as a function of the exciton group velocity for different exciton densities. Within the range of velocities relevant to the experiments considered here ($< 10\mu$m/ns), the correction to the optical lifetime is rather minor. Therefore, it is neglected in the subsequent calculations. Note that for higher group velocities, $v_g = 10{-}30\mu$m/ns and exciton densities $10^9{-}10^{11}$cm^{-2}, the exciton lifetime

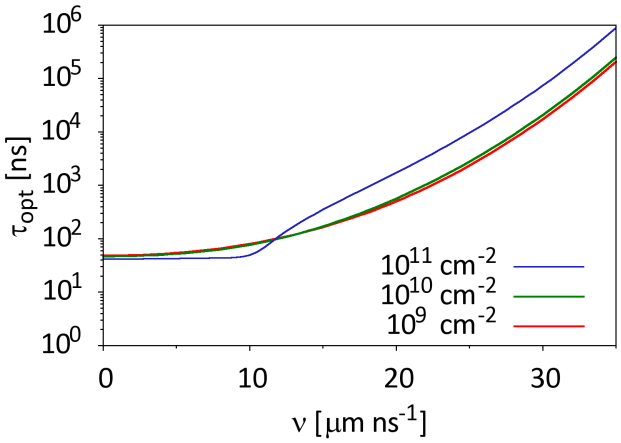

Figure 3.1: Exciton optical lifetime against group velocity for various exciton densities.

increases from the intrinsic lifetime of a few tens of nanoseconds up to milliseconds as the exciton momentum distribution moves further out of the radiative zone.

3.4 Electrostatic ramps

As discussed in section 3.1.4, the study of indirect excitons in linear potential energy gradients (ramps) can reveal information about the exciton transport properties. This information is useful in understanding the dynamics of excitons confined to trapping potentials. Also, this fundamental insight is necessary if indirect excitons are to be utilised for optoelectronic device applications. In this section, analytical and numerical studies of the transport equation are presented. The transport equation is modified to include the externally applied ramp potential. The modeling was done in the context of an experiment where excitons were created in a narrow potential energy channel so that only transport along one dimension was permitted. The floor of the narrow channel had a region of constant slope in energy. The exciton PL signal in this region was the focus of the study.

3.4.1 ANALYTIC RESULTS

The contribution to the drift current as the result of a potential ramp is

$$J_{\text{ramp}} = -\mu n \frac{\partial}{\partial x}(V_0 - Ex). \tag{3.5}$$

Here, E is the magnitude of a constant electric field pointing in the x-direction and V_0 is the potential at $x = 0$. A rather general homogeneous transport equation with solution $n(x, t)$ which has no source or decay terms may be written as

$$\frac{\partial n}{\partial t} = F(n, \frac{\partial n}{\partial x}, \frac{\partial^2 n}{\partial x^2}), \tag{3.6}$$

where F is the rate of change in $n(x, t)$ due to all other currents besides J_{ramp}. With the addition of the ramp, the density distribution $n'(x, t)$ satisfies

$$\frac{\partial n'}{\partial t} = F(n', \frac{\partial n'}{\partial x}, \frac{\partial^2 n'}{\partial x^2}) - \mu E \frac{\partial n'}{\partial x}. \tag{3.7}$$

By direct substitution, one finds that the solution n' in the presence of a constant electric field is the same as the solution n but with the distribution having a constant velocity in the positive x-direction:

$$n'(x, t) = n(x - x_0 - v_{\text{drift}} t, t), \tag{3.8}$$

where $v_{\text{drift}} = \mu E$ is the drift velocity and x_0 is the center of the distribution at $t = 0$. For example, in a diffusive regime transport on a ramp is given by

$$\frac{\partial n}{\partial t} = D \frac{\partial^2 n}{\partial x^2} - \mu E \frac{\partial n}{\partial x}. \tag{3.9}$$

This is just the standard diffusion equation (2.12) in one dimension with a term added to include drift via the ramp. It's solution is

$$n = \frac{N}{\sqrt{4\pi D(t + t_0)}} \exp\left[-\frac{(x - x_0 - \mu E t)^2}{4D(t + t_0)}\right]. \tag{3.10}$$

For dipole orientated excitons on a ramp at low temperature, the transport equation is

$$\frac{\partial n}{\partial t} = \mu u_0 \left(n \frac{\partial^2 n}{\partial x^2} + \left(\frac{\partial n}{\partial x}\right)^2\right) - \mu E \frac{\partial n}{\partial x}, \tag{3.11}$$

which has solution

$$n = \left(\frac{3N^2}{32\mu u_0(t+t_0)}\right)^{1/3} - \frac{(x - x_0 - \mu E t)^2}{6\mu u_0(t+t_0)}. \tag{3.12}$$

The solutions (3.10) and (3.12) are comparable in form to the two-dimensional solutions for the diffusive and drift regimes shown in (2.12) and (2.14) of chapter two.

The full transport equation for indirect excitons on a ramp, including source and decay terms, is given by

$$\frac{\partial n_{\mathrm{x}}}{\partial t} = \frac{\partial}{\partial x}\left[D_{\mathrm{x}}\frac{\partial n_{\mathrm{x}}}{\partial x} + \mu n_{\mathrm{x}}(u_0\frac{\partial n_{\mathrm{x}}}{\partial x} - E)\right] + \Lambda - \frac{n_{\mathrm{x}}}{\tau}. \tag{3.13}$$

For this equation, it is assumed that there is no transverse exciton transport (i.e., $\partial/\partial y = 0$). This is correct in certain situations. For example when the ramp is along the floor of a narrow channel in the exciton potential landscape or when the excitation geometry is homogeneous in the y-direction.

One can transform equation (3.13) into an equation for the first moment of the density distribution $M_1 = \int x n_{\mathrm{x}} dx / \int n_{\mathrm{x}} dx$. This is done by multiplying it by x/N and integrating over $x \in \Re$. Here $N = N(t)$ is the total number of excitons in the system and approaches constant value for large t. Some simplifications may be made by using the classical limit for the exciton mobility given in equation (2.8) and neglecting the effects of QW disorder. In this case, and with a symmetric laser focused at the origin, M_1 is a solution to the following,

$$\frac{\partial M_1}{\partial t} = \frac{1}{N}\int \mu_{\mathrm{clas}} n_{\mathrm{x}} E dx - \frac{M_1}{\tau}. \tag{3.14}$$

The steady state solution of equation (3.14) is $M_1 = \mu E \tau$. The displacement of excitons from the excitation spot is equal to the product of the in-plane electric field strength, exciton mobility and lifetime. This provides a means to experimentally determine the exciton mobility from the extension of the exciton cloud along the ramp. The optical lifetime can be measured from the exciton decay time after laser termination and is controlled by the electric field in the growth direction. Therefore, studying the first moment of n_{x} as a function of electric field enables estimation of the mobility. Experimentally, one can study the first moment of the PL signal which is approximately proportional to n_{x}.

3.4.2 NUMERICAL SIMULATIONS

In this section, simulation results for exciton transport via a ramp are shown. The data is compared to experimental results where a ramp created by a shaped electrode at constant voltage was used. Fig. 3.2a shows the potential landscape as a result of a shaped electrode which is designed to create a ramp. The outline of the electrode is shown by the overlaying black line. The long narrow electrode creates a potential energy channel to which excitons are confined and may only travel along the x-axis. The constant voltage over the entire electrode implies a constant charge density. This means that for a wider electrode, a greater charge per unit length in the x-direction is present and therefore the energy channel will have a greater depth. Shown here is an electrode with width that changes linearly with x from $10 - 20\,\mu$m. The potential along the line $y = 0$ is shown in Fig. 3.2b. The energy of indirect excitons is constant in the flat-energy channels where the electrode width is constant. Narrowing the electrode increases the exciton energy which creates a ramp in the potential.

The smoothing of the potential near the electrode edges is achieved by placing the CQWs $1\,\mu$m below the top shaped electrode. If the CQWs are much closer to the electrodes, the result is a high in-plane electric field E at the edges of the electrode as the step in the potential from inside to outside the electrode area is greater. This causes exciton ionisation. Similar studies of exciton transport via a ramp have been done previously where the ramp potential was created by a voltage gradient in the top electrode. This, however, causes an electric current through the electrode which heats the sample. Heating by electric currents is greatly suppressed by using the shaped-electrode-method.

In the experiment considered here, the electrode shape was designed to obtain a ramp with a constant potential energy gradient. The height of the ramp, which is proportional to the electrode voltage, is controllable in experiments. The transport of excitons along the flat energy channels and ramp are modeled using a transport equation similar to equations (2.3) and (3.13):

$$\frac{\partial}{\partial x}\left[D_{\mathrm{x}}\frac{\partial n_{\mathrm{x}}}{\partial x} + \mu_{\mathrm{x}} n_{\mathrm{x}} \frac{\partial}{\partial x}(u_0 n_{\mathrm{x}} + V_{\mathrm{ramp}})\right] + \Lambda - \frac{n_{\mathrm{x}}}{\tau_{\mathrm{opt}}} = 0. \tag{3.15}$$

The first and second terms in the square brackets account for exciton diffusion and drift, respectively. The difference here from the equations given in chapter two is that

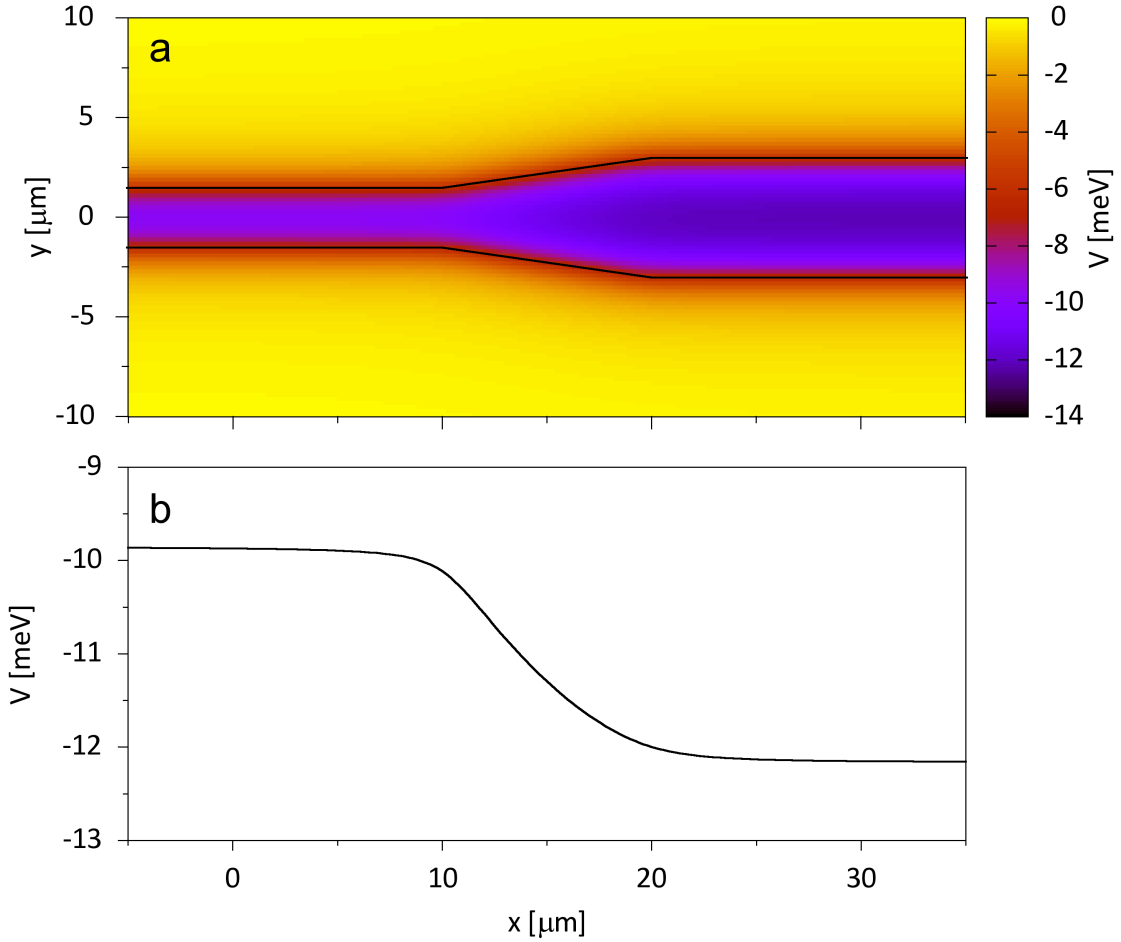

Figure 3.2: (a) Potential landscape due to a shaped electrode above the CQWs. The electrode outline is shown by the black lines. (b) The profile of the applied exciton potential along the line $y = 0$.

in the one-dimensional geometry relevant to the experiment, $\nabla = \partial/\partial x$. Also, the ramp potential V_{ramp} is included in the drift term. In this work, the dynamics of the ramp were not studied. Hence $\partial n_{\mathrm{x}}/\partial t = 0$ gives the right hand side of equation (3.15). The decay rate of excitons, $1/\tau_{\mathrm{opt}}$, is given by equation (2.24). The exciton generation rate $\Lambda = \Lambda(x)$ is approximated as homogeneous in the y-direction. The diffusion coefficient D_{x} and mobility μ_{x} are given by equations (2.6) and (2.7) respectively. For the fit parameter U_0, where $U_0/2$ is the amplitude of disorder potential in the structure, $U_0 = 1.5\,\mathrm{meV}$ was used.

The thermalisation equation to account for energy relaxation of photo excited excitons is

$$S_{\mathrm{ph}}(T_0, T) + S_{\mathrm{pump}}(T_0, T, \Lambda, E_{\mathrm{ex}}) = 0. \tag{3.16}$$

Again, the time derivative is set to zero for steady-state calculations which gives the right hand side of equation (3.16). S_{ph} and S_{pump} are given by equations (2.20) and (2.17) respectively. S_{ph} is the cooling rate due to bulk longitudinal acoustic phonon emission, and S_{pump} is the heating rate due to the laser excitation. The excess energy of photo excited excitons used here is $E_{\mathrm{ex}} = 17\,\mathrm{meV}$. Note that the heating due to the optical evaporation of low energy excitons used in chapter two is neglected here since it was previously found to be a minor correction (a few percent) to the temperature profile. All other parameters of the model are given in table 1.1.

The results from simulations of indirect excitons on a ramp using equations (3.15-3.16) are presented in Fig. 3.3. The steady-state solution algorithm described in section 2.6 was used. Figs. 3.3a and 3.3b show the temperature profiles along the narrow channel with and without a gradient in the applied potential. The total effective indirect exciton potential, $V_{\mathrm{x}} = V_{\mathrm{ramp}} + u_0 n_{\mathrm{x}}$, is shown by the brown curve in Fig. 3.3b. At the bottom end of the ramp, the applied potential is partly screened by indirect excitons. Figs. 3.3c and 3.3d show the corresponding density (black curves) and PL intensity profiles (green curves). The one-dimensional equivalent of the inner ring is seen in Fig. 3.3c. The symmetric density distribution in Fig. 3.3c is shifted in the positive x-direction in Fig. 3.3d due to the ramp. Excitons accumulate at the bottom of the ramp causing a peak in density. In both cases, the emission intensities I_{PL} show suppression of the optical decay due to laser induced heating.

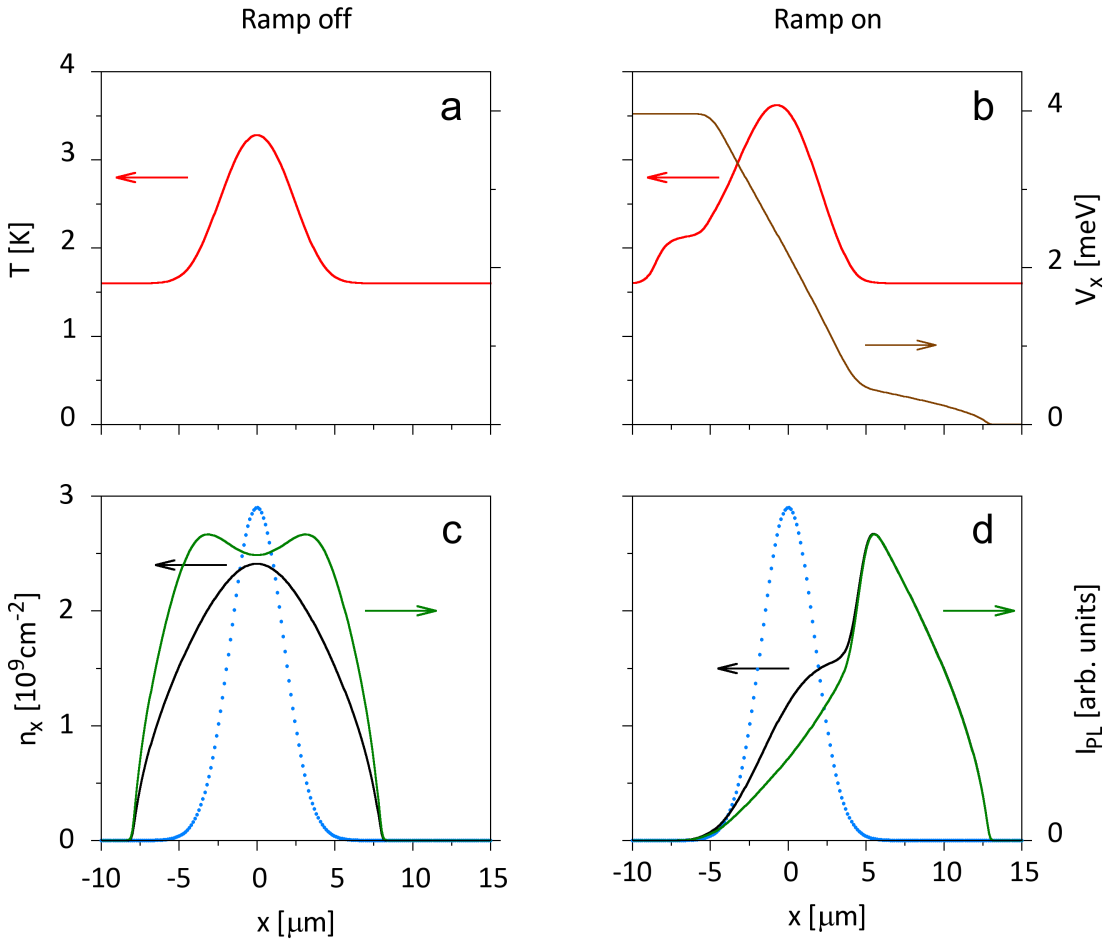

Figure 3.3: Simulations of indirect exciton transport with (b and d) and without (a and c) the presence of a ramp potential. The density (black) and PL intensity profiles (green) are shown in (c) and (d). The corresponding temperature profiles are shown by the red curves in (a) and (b). The brown line in (b) is the total effective exciton potential due to the ramp plus the dipole-dipole interactions.

3.4.3 COMPARISON WITH EXPERIMENT

To make a quantitative comparison, the ramp potential and the parameters of the model were chosen to match experimental conditions [40]. Fig. 3.4a shows the effectiveness of the ramp as a function of the exciton generation rate for different temperatures. The effectiveness of the ramp is quantified by the average transport given by the first moment of the PL intensity, M_1. At low densities, excitons are localised to minima of the disorder potential and are not effectively transported by the ramp. At higher densities, excitons screen the disorder potential and transport down the ramp. The effect of QW disorder also explains the temperature dependence of the data. In a higher temperature exciton gas, the fraction of excitons with low enough in-plane kinetic energy to become localised in the disorder potential is smaller. Therefore, at a higher temperature, excitons move more freely under the action of the ramp. Fig. 3.4b shows the equivalent data from experiment. P_{laser} is the laser excitation power which is assumed to scale linearly with the exciton generation rate, Λ. Qualitatively, the same trends are seen in the experimental data as is seen in simulations. The abrupt drop in M_1 for higher P_{laser} is attributed to a photoexcitation-induced reduction of the electric field in the device [40].

3.5 THE ELECTROSTATIC CONVEYER

In this section, transport of indirect excitons in a moving electrostatic lattice (conveyer) is studied. The principle of operation of the conveyer is that indirect excitons drift towards the minima of the conveyer potential and are then carried by the conveyer as it propagates along the QW plane. The results are compared to experimental work where a conveyer was created by a set of electrodes at ac voltages. Moving potential lattices for excitons and polaritons realised by surface acoustic waves have been studied by others previously [6, 85]. The advantage, however, of the electrostatic conveyer is that its velocity is controllable by the frequency of the ac voltages applied to the electrodes. In contrast, surface acoustic waves are restricted to the sound velocity. For the considered system, the surface acoustic wave velocity is $3\,\mu$m/ns whereas an electrostatic conveyer velocity of up to two times greater has been achieved. Similar experiments have also been done in atomic physics where a gas of cold atoms was transported by a magnetic conveyer [86] and single atom transport has been achieved using counter-propagating laser beams [87].

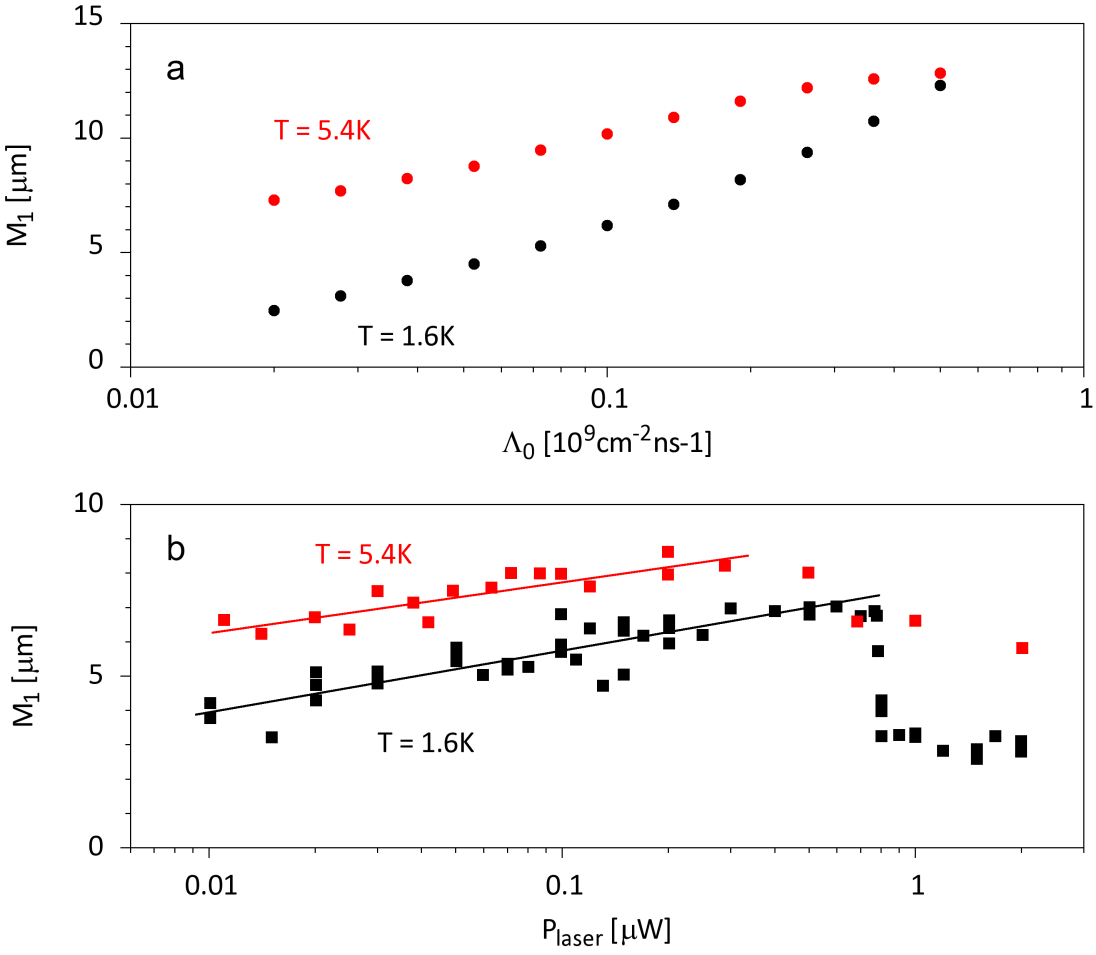

Figure 3.4: Effectiveness of exciton transport via the ramp at different temperatures as quantified by the first moment of the PL signal M_1. (a) Simulation results for varying the exciton generation rate and (b) experimental results for varying the laser excitation power.

Schematically, the conveyer consists of electrodes positioned parallel to each other on the sample surface above the QWs. A dc bias is applied to the electrodes so that photo excited excitons are of the indirect type. An additional ac voltage is applied to the electrodes but with a phase delay between each electrode. This creates a roughly sinusoidal exciton potential which propagates along the QW plane.

3.5.1 MODEL

The following equation was used to model in-plane transport of indirect excitons subject to the applied conveyer potential, V_{conv}

$$\frac{\partial n_{\text{x}}}{\partial t} = \nabla \cdot [D_{\text{x}} n_{\text{x}} + \mu_{\text{x}} n_{\text{x}} \nabla (u_0 n_{\text{x}} + V_{\text{conv}})] + \Lambda - \frac{n_{\text{x}}}{\tau}. \tag{3.17}$$

As in the previous section, D_{x} and μ_{x} are the diffusion coefficient and mobility given in equations (2.6) and (2.7) respectively. An example of the indirect exciton spatial PL pattern observed in experiments with and without the conveyer activated is shown in Fig. 3.5 below. From these, one can note that in the presence of the conveyer, the exciton cloud is greatly extended compared to when the conveyer is off. Also, it is seen from the previous calculations in this thesis that variations in temperature from the bath temperature are restricted only to the vicinity of the laser excitation spot. Therefore, it is reasonable to assume that the exciton gas outside the excitation spot will be in thermal equilibrium with the GaAs lattice. In this case the exciton temperature can be considered constant ($T = T_b$) in order to simplify calculations. To still be able to make a qualitative comparison with the experiment, the measured PL signal can be neglected from a few μm around the excitation spot where thermalisation effects are important. Neglecting the PL signal from this region is also done in the calculation of M_1 in simulations. Since a constant temperature is assumed, the lifetime can also be taken as constant. According to equation (3.4), the lifetime depends on exciton density, temperature and group velocity. However, it is only weakly density dependent and for low temperatures and moderate conveyer velocities, it is approximately $2\tau_r$ where τ_r is the intrinsic lifetime of the ground state exciton.

It can also be noted from the experimental observations that the motion of the exciton cloud during transport via the conveyer can be decoupled into motion

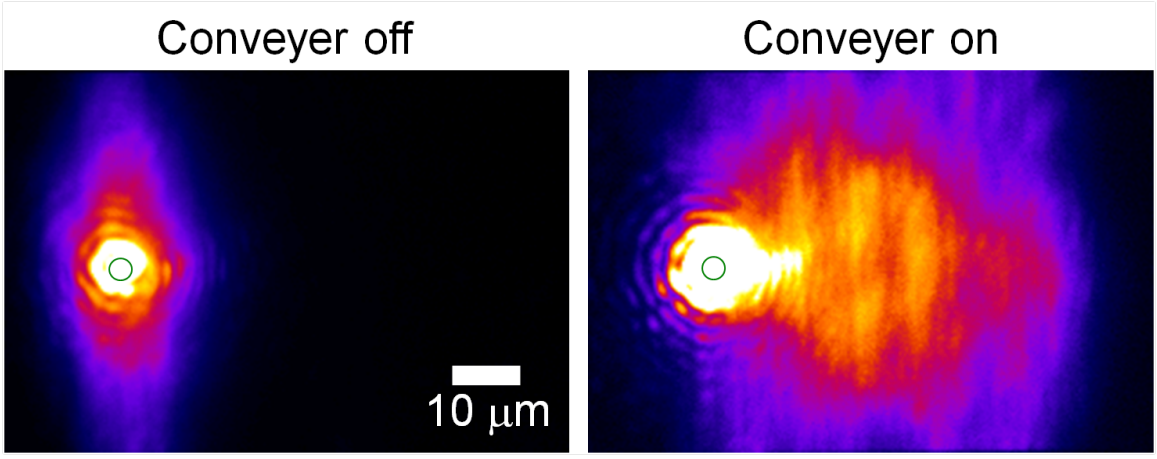

Figure 3.5: Experimental measurements of the spatial PL pattern with and without the propagating conveyer potential. In each case, the excitation spot is shown by the green circle.

along the direction of conveyer propagation (x-direction) and motion perpendicular to conveyer propagation (y-direction). In the x-direction, transport is predominantly driven by the external field whereas in the y-direction it is governed by diffusion and exciton-exciton repulsion and will have a profile similar to the analytic solutions given in (2.13) and (2.15). Hence the transport equation (3.17) need only be solved for the x-direction. This is done by taking $\partial/\partial y = 0$ so that $\nabla = \partial/\partial x$ and the exciton density n_{x} in this context is an average density over y.

For the considered experiment, the distance between the electrode centers is $2\,\mu$m and the conveyer periodicity is 7 electrodes giving a wavelength of $14\,\mu$m. The total conveyer length is $380\,\mu$m and its width is $80\,\mu$m. The electrodes are semi-transparent so as to allow observation of the spatial PL pattern. As in the case of the ramp experiment, the CQWs are positioned closer to the homogeneous bottom electrode to smooth the potential and suppresses the in-plane electric field near the electrode edges, which can otherwise cause exciton dissociation. The geometry of the experiment is shown in Fig. 3.6a and a plot of conveyer potential is shown in Fig. 3.6b. This experimental setup enabled control of the amplitude of the conveyer potential by adjusting the amplitude of the ac signal and the conveyer velocity is controlled by the ac frequency.

The conveyer potential is shown in Fig. 3.6b. This is calculated using equation (3.2) and is well approximated by

$$V_{\mathrm{conv}} = (1 + A_{\mathrm{elec}} \cos(k_{\mathrm{elec}} x + \delta_{\mathrm{elec}}))(V_g + V_0 \cos(k_{\mathrm{conv}} x - \omega t)). \tag{3.18}$$

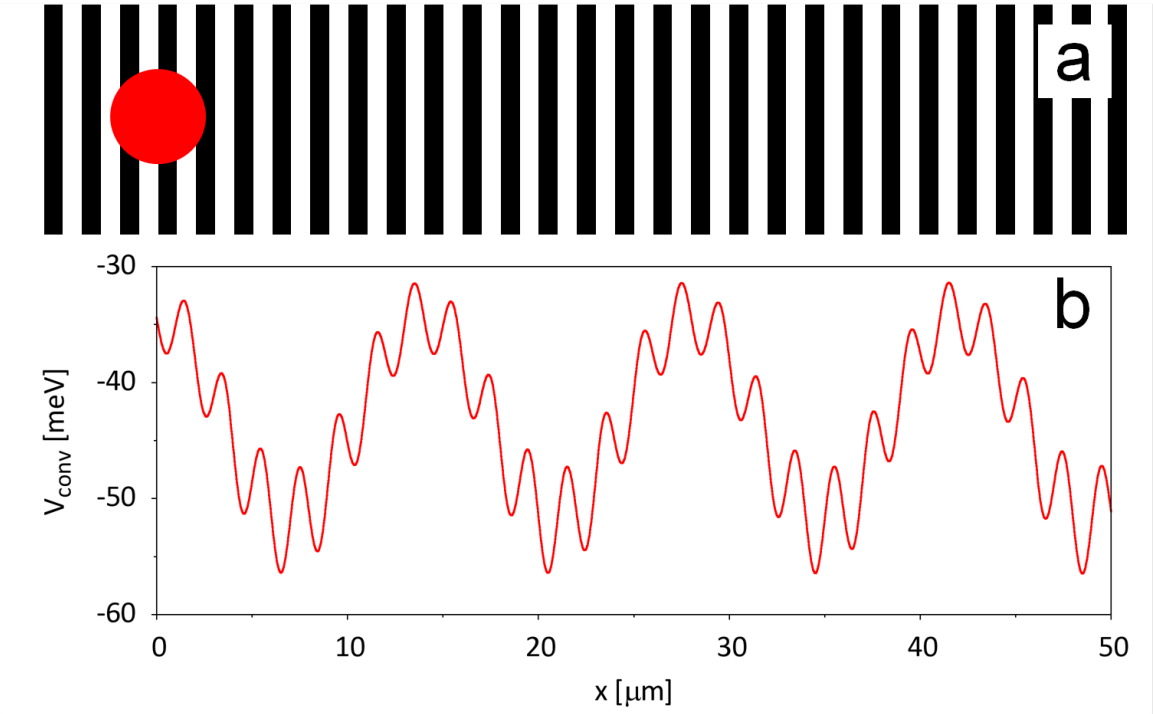

Figure 3.6: The geometry (a) and potential (b) of the electrostatic exciton conveyer. The laser excitation spot is shown by the red circle in (a).

The sinusoidal envelope of the conveyer potential with period $14\,\mu$m is modulated by ripples of period $2\,\mu$m ($k_{\rm conv} = 0.45\,\mu{\rm m}^{-1}$ and $k_{\rm elec} \approx \pi\,\mu{\rm m}^{-1}$). The ripples originate from the spacing between the conveyer electrodes. The amplitude of the ripples, $A_{\rm elec} = 0.0875$, can be decreased by decreasing the width and spacing of the conveyer electrodes. For CQWs placed $1\,\mu$m below the electrodes, the ripples almost completely vanish when the spacing between the centers of the electrodes is less than $0.5\,\mu$m. The dc bias term $V_g = -43.16\,$meV causes the regime where indirect excitons are dominant and controls the exciton lifetime. The conveyer amplitude V_0 was varied between $0-10\,$meV. The conveyer potential propagates with velocity $\nu_{\rm conv} = \omega/k_{\rm conv}$ where ω is the angular frequency of the ac voltages applied to the electrodes. The constant phase term $\delta_{\rm elec} = -1.53$ defines the position of the electrodes with respect to the center of the laser excitation spot.

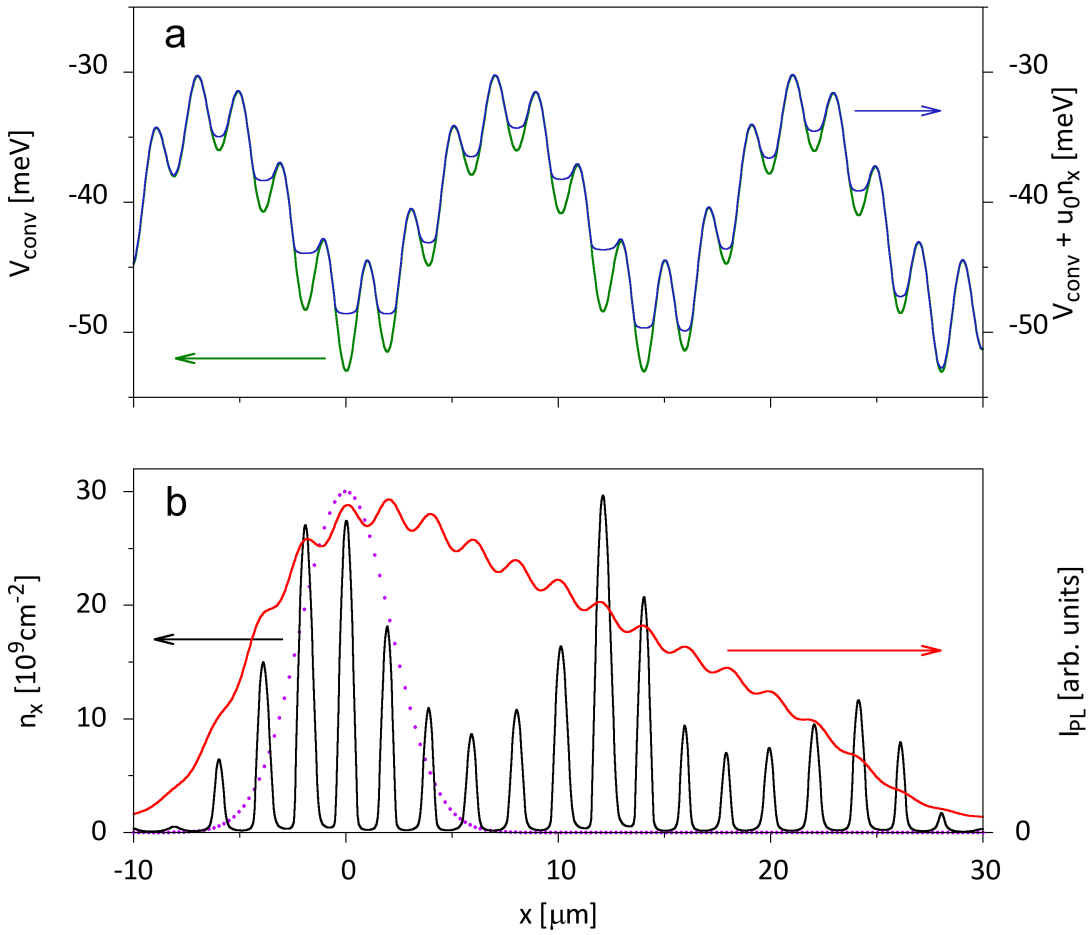

Figure 3.7: (a) The conveyer potential (green) and total effective exciton potential (blue). (b) The indirect exciton density (black) and time-integrated, spatially convoluted PL intensity (red). The laser profile is shown by the purple dotted line in (b).

3.5.2 RESULTS

The results of the simulations are presented in Fig. 3.7. The green curve in Fig. 3.7a shows a snapshot of the bare conveyer potential and the corresponding exciton density distribution is shown by the black curve in Fig. 3.7b. The amplitude and speed of the conveyer are $V_0 = 8\,\text{meV}$ and $\nu_{\text{conv}} = 0.7\,\mu\text{m/ns}$ respectively. The Gaussian profile of the laser excitation is shown by the dotted line in Fig. 3.7b. Indirect excitons accumulate in the minima of the conveyer potential and are transported along the QW plane. The conveyer potential is partially screened by the indirect exciton repulsive interaction. The screened conveyer potential is shown by the blue curve in Fig. 3.7a. Note that the ripples in the conveyer potential do not propagate since their positions are determined by the positions of the electrodes. However, the

energy of the ripples' minima oscillates in time as the conveyer propagates. Effectively, the excitons move from one minima to another in order to minimise potential energy. The density distribution in Fig. 3.7b shows that excitons are mainly situated in the minima of the ripples and the highest densities are found in the minima of the conveyer. The red curve in Fig. 3.7b shows the PL intensity, I_{PL} for comparison with experimental data. For the constant lifetime assumed here, the PL signal is proportional to the the exciton density. However, the PL profile shown here is time integrated over several periods of the conveyer to match conditions of the experiment which were performed without time resolution. Further, the PL profile is then spatially convoluted with a Gaussian of width $2\,\mu$m to obtain I_{PL}. This accounts for the limited spatial resolution of the imaging device used. The large extension of the exciton density in the positive x-direction reproduces well the observed PL images shown in Fig. 3.5.

The effectiveness of the conveyer is quantified by the average exciton transport distance via conveyer and is evaluated by the first moment M_1 of I_{PL}. In the evaluation of M_1, the PL signal from the region $|x| < 7\,\mu$m was excluded since in the experimental data, the emission in that region was found to have originated mainly from the bulk GaAs structure. The dependence of M_1 on the conveyer amplitude and velocity and the generation rate of excitons is discussed in following subsections and comparisons with the experimental data are made.

3.5.3 Conveyer amplitude and velocity dependence

Fig. 3.8 shows the simulated exciton transport distance via the conveyer, M_1, as a function of conveyer amplitude V_0 for different conveyer velocities. Each point on the plot corresponds to a different numerical simulation. For a shallow conveyer, M_1 is not affected by the conveyer's motion. This indicates that the excitons do not follow the moving lattice - they are localised to the disorder potential and ripples in the conveyer. They are dynamically delocalised in the lattice. For increasing conveyer amplitudes, the excitons start to follow the conveyer - they are dynamically localised in the lattice.

Fig. 3.8 also shows that the effectiveness of the conveyer decreases for increasing conveyer velocity. This is explained as follows. Excitons can only efficiently follow the moving conveyer potential when the conveyer velocity is less than the drift

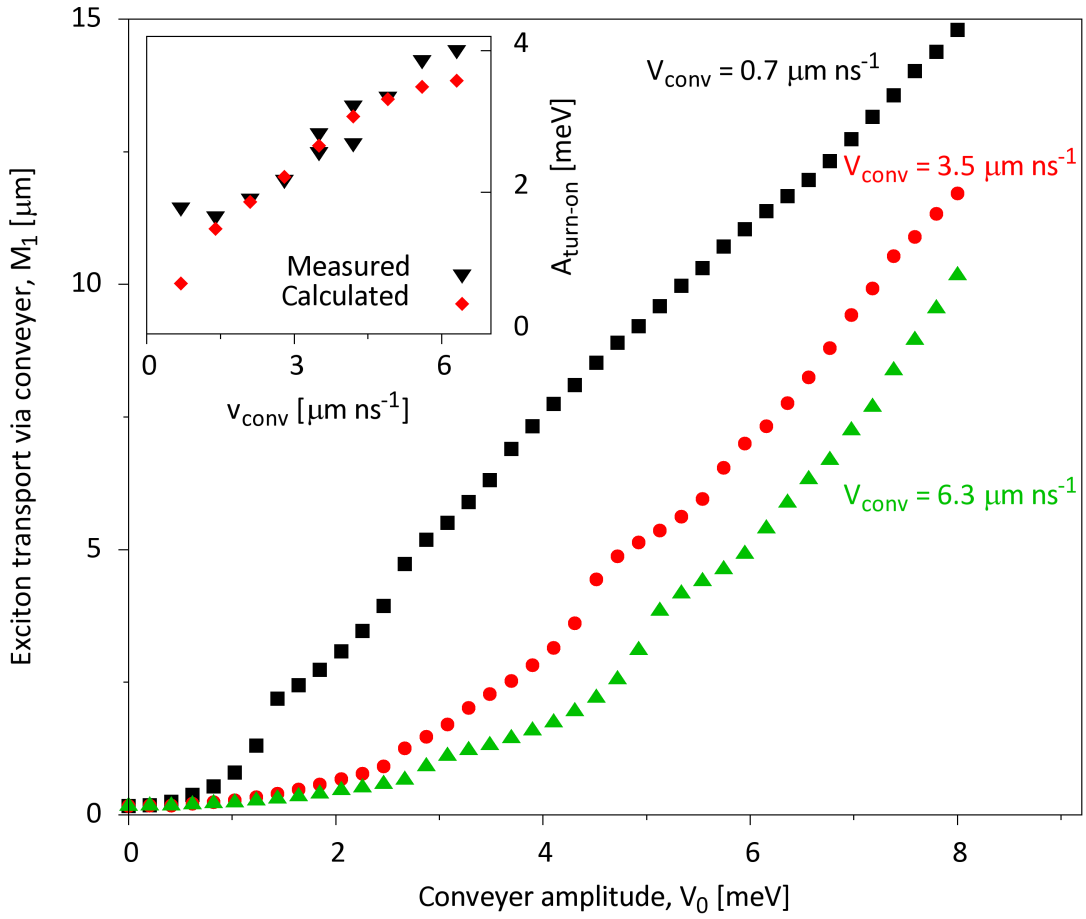

Figure 3.8: Simulated effectiveness of exciton transport via the conveyer against conveyer amplitude for various conveyer velocities. The inset shows the amplitude of the conveyer at the dynamical localisation-delocalisation transition, $A_{\mathrm{turn-on}}$, as a function of conveyer velocity for both simulation and experiment.

velocity of excitons caused by the conveyer potential. To clarify, for each conveyer amplitude, there is a characteristic time required for excitons to move to the minima of the conveyer potential. If this time is longer than the time period of the conveyer then excitons are unable to become dynamically localised in the moving lattice.

For low conveyer amplitudes, excitons are not localised to the minima of the moving conveyer potential. Therefore, they do not follow the conveyer. This is because the conveyer amplitude is less than either the interaction energy associated with the exciton dipole-dipole repulsion or the amplitude of the QW disorder potential. When the conveyer amplitude becomes larger than both the exciton interaction energy and the disorder amplitude, excitons can become localised in the minima of the moving conveyer potential. This results in exciton transport via the conveyer.

The transition between the two regimes, i.e. the dynamical localisation-delocalisation transition (DLDT), is of particular interest. It is the dynamical counterpart of the localisation-delocalisation for indirect excitons in static lattices [36]. The conveyer amplitude at the DLDT, $A_{\mathrm{turn-on}}$ is defined by the point at which a linear extrapolation of the high amplitude part of the curves in Fig. 3.8 intersects the x-axis. The inset in Fig. 3.8 shows $A_{\mathrm{turn-on}}$ as a function of the conveyer velocity for both the simulated and experimental data. In both cases, the data shows that $A_{\mathrm{turn-on}}$ increases with ν_{conv}. The exciton transport via the conveyer is less efficient for higher conveyer velocities.

For comparison, the experimentally measured conveyer velocity and amplitude dependence of M_1 are presented in Fig. 3.9 [39]. As is the case throughout this thesis, the parameters of the simulation have been chosen to match the conditions of the experiment from whence the data was obtained. The experimental data and theoretical simulations of exciton transport via conveyer are in qualitative agreement (compare Figs. 3.8 and 3.9). The discrepancy between the simulated and measured data for high conveyer amplitudes can be related to device imperfections. The experimental data shows the same DLDT which occurs for increasing conveyer amplitude. The simulated and measured conveyer amplitude at the DLDT, $A_{\mathrm{turn-on}}$, which are plotted together in the inset of Fig. 3.8 are in good agreement.

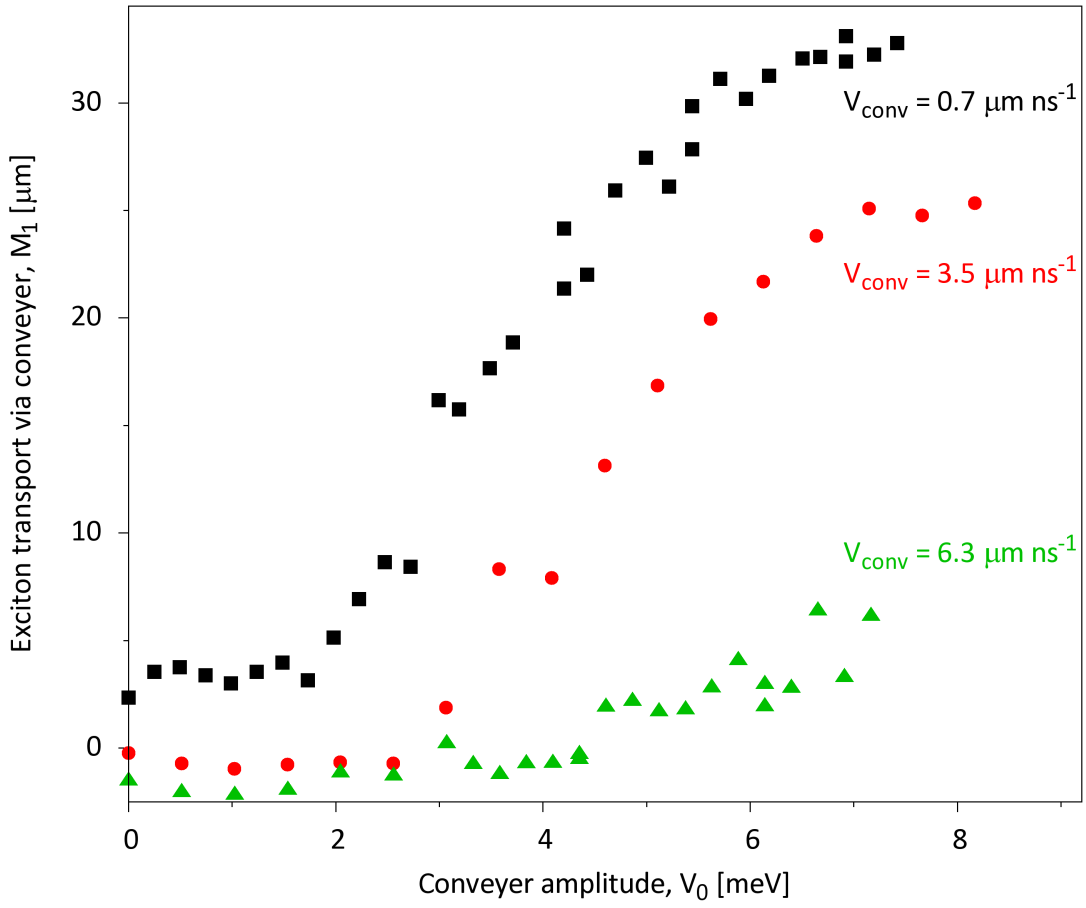

Figure 3.9: Measured effectiveness of exciton transport via the conveyer against conveyer amplitude for various conveyer velocities.

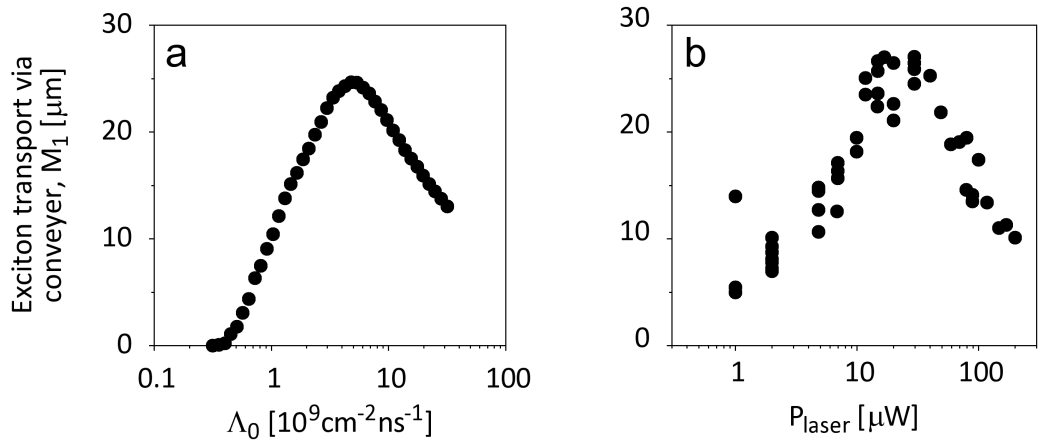

Figure 3.10: Effectiveness of the exciton transport via the conveyer, M_1, as a function of the exciton generation rate for simulations (a) and as a function of laser excitation power for experiments (b).

3.5.4 EXCITON DENSITY DEPENDENCE

In order to simplify the calculations for the analysis of the exciton density dependence, the conveyer potential was approximated by the following cosine function

$$V^*_{\rm conv} = \Delta + V_0 \cos(k_{\rm conv} x - \omega t). \tag{3.19}$$

Here, the ripples in the conveyer potential are removed. Instead, the effect of the ripples was included in the same way as the disorder potential. The position of the ripples is fixed, similar to the position of minima in the CQW disorder potential. The effect of the CQW disorder and conveyer ripples on exciton transport was approximated within the thermionic model for the diffusion coefficient discussed in chapter two. The modified diffusion coefficient, $D^*_{\rm x}$ is given by

$$D^*_{\rm x} = D^{(0)}_{\rm x} \exp\left[-\frac{U_0 + U_0^{(\rm ripple)}}{k_B T + u_0 n_{\rm x}}\right]. \tag{3.20}$$

Here $U_0^{(\rm ripple)}$ is the ripple amplitude obtained by simulations. $U_0^{(\rm ripple)}$ is nearly proportional to $V^*_{\rm conv}$ and, therefore, it is approximated by $U_0^{(\rm ripple)} = CV^*_{\rm conv}$ (C is a fitting constant). The simplification of calculations which results from the removal of the ripples from the conveyer potential enables simulations to be done at high exciton densities. For high densities, the ripples in the conveyer potential lead to numerical instabilities which originate from the non-linear drift term in equation (3.17). The

dependence of the effectiveness of conveyer transport on density dependence is presented in Fig. 3.10. For simulations, M_1 is plotted against the exciton generation rate and for the experimental data, M_1 is plotted against the laser excitation power, P_{laser}. Fig. 3.10 shows that excitons are only weakly affected by the conveyer at low densities. This is because at low densities, the excitons are localised to minima of the intrinsic disorder potential and ripples in the conveyer potential. The most efficient exciton transport is achieved at intermediate densities where excitons effectively screen the disorder and the ripples and follow the conveyer motion. Finally, exciton transport via the conveyer is less effective at higher densities as excitons screen the conveyer potential and travel in all directions, independent of the applied potential. The simulated density dependence of exciton transport via conveyer is in strong agreement with the experimental data.

3.6 SUMMARY

In this chapter, the transport of indirect excitons in externally applied electric potential landscapes was studied. An outline of the results previously published by various research groups was given and the motivation for this avenue of work was highlighted. It was shown how patterned electrodes on the sample surface result in indirect excitons experiencing an in-plane force. This force was included into the exciton transport equation. Specific forms of the exciton potential landscape included linear potential gradients (ramps) and propagating lattices (conveyers). Analytical and numerical studies showed how these potentials modify the exciton density distribution. Excitons travel towards the minima of the effective potential which is the sum of the external potential plus the dipole-dipole potential. In the case of the ramp, this leads to a strong accumulation of excitons at the bottom of the ramp. In conveyers, it leads to localisation of excitons in the minima of the lattice potential and exciton transport which follows the conveyer. The dynamical localisation-delocalisation transition was captured by the theoretical model of excitons in a conveyer potential. It was found that excitons are only effectively transported by the conveyer when the density is sufficient to screen in the QW disorder potential. For high conveyer velocities, the effectiveness of the conveyer diminishes as there is insufficient time for excitons to localise in potential minima. The screening of the conveyer potential for high exciton densities was also discussed. In all cases, calculations of the profile of the exciton PL pattern were found to be in good agreement with experimental data.

4 Fragmentation of the external exciton ring

Under optical excitation, CQWs are known to reveal fascinating features in the photoluminescence pattern originating from dipole orientated indirect excitons. The subject of this chapter is a feature known as the *external ring*. The appearance of the external ring has previously been attributed to macroscopic charge separation in the quantum well plane [88–91]. Here, a classical model of non-linear diffusion is used to account for the observed fragmentation of the external ring into a periodic array of islands [92]. The model incorporates the Coulomb interactions between electrons, holes and indirect excitons. Simulations show that at low temperatures, these interactions lead to pattern formation similar to the experimentally observed ring fragmentation. The fragmentation is found to persist to temperatures above the quantum degeneracy temperature of indirect excitons.

4.1 Background

Previous studies of the external ring [90, 91, 93] have shown that it forms at the interface between spatially separated electron-rich and hole-rich regions. This is due to a difference in the capture efficiency of the injected electrons and holes which results from their different masses. An abundance of holes builds around the laser spot as some fraction of electrons leaks to the electrodes. In the presence of an electric field, the doping in the electrode layers leads to a background electron concentration within the wells. The result is a pool of holes surrounded by a sea of electrons with

excitons forming at the boundary.

Perhaps the most remarkable feature of the indirect exciton PL pattern is that the external ring fragments into a periodic array of islands for temperatures below $\approx 3\,\mathrm{K}$ [8, 94, 95]. The transition to the fragmented ring state is as an abrupt, strictly low-temperature one. Superficially, this evidence suggests that some kind of novel quantum effects are at work. Since its discovery, the origin of the external ring has been the focus of much debate and different theoretical models have been used to explain the appearance of the external ring. One such model [96] explains the macroscopic ordering via a process of stimulated scattering of excitons into the ground state whilst another model [97] assumes a BEC present in the ring. Both of these works imply that fragmentation is a signature of quantum degeneracy. An alternative model explained the ring fragmentation in terms of attractive interactions between excitons [98–103]. In this framework, a ring of uniform density becomes unstable and the attractive interaction leads to droplet formation. However, measurements of the blue shift in the exciton emission [94] reveal clear evidence that the interaction is repulsive and that this mechanism cannot be responsible for the effect.

In this chapter, a model is presented to assess the importance of Coulomb interactions in the external ring. It is found that at low temperatures, these interactions lead to periodic modulation of the exciton density. Whilst spatial coherence measurements suggest a statistically degenerate exciton gas is present in the ring [13, 95, 104, 105], it is illustrated here that fragmentation can occur due to classical mechanisms and cannot unambiguously be taken as evidence of degeneracy.

Studies of the role of Coulomb interactions in this system have been attempted previously [106, 107] and have highlighted their effect on the appearance of the external ring. However, due to the computational complexity of the problem, these works have been limited to the case of one dimensional geometry or to a low density regime and are insufficient to capture fragmentation of the ring. However, in Ref. [107], it is shown that inclusion of Coulomb terms is necessary to explain the threshold dependence of the ring radius on excitation power and confirms the significance of the contribution made by the interactions included here.

Conceptually, it is found that at low temperatures, the diffusive nature of carrier transport diminishes. In this regime, carriers move under the action of strong electric fields provided mainly by the in-plane charge separation of electrons and holes. Under these conditions, a ring of uniform density is an unstable configuration and the

system naturally evolves to a fragmented ring as a process of energy minimization.

4.2 COUPLED TRANSPORT EQUATIONS FOR ELECTRONS, HOLES AND INDIRECT EXCITONS

Based on the approach used in [91, 93, 107, 108], the following set of coupled equations were used to model the creation, transport and decay of indirect excitons and free electrons and holes in CQWs:

$$\begin{aligned}
\frac{\partial n_{\mathrm{e}}}{\partial t} &= \nabla\left[D_{\mathrm{e}}\nabla n_{\mathrm{e}} + \mu_{\mathrm{e}} n_{\mathrm{e}} \nabla U_{\mathrm{e}}\right] + \frac{n_{\mathrm{e}}^{(0)} - n_{\mathrm{e}}}{\tau_{\mathrm{e}}} + \Lambda_{\mathrm{e}} - w n_{\mathrm{e}} n_{\mathrm{h}}, \\
\frac{\partial n_{\mathrm{h}}}{\partial t} &= \nabla\left[D_{\mathrm{h}}\nabla n_{\mathrm{h}} + \mu_{\mathrm{h}} n_{\mathrm{h}} \nabla U_{\mathrm{h}}\right] + \Lambda - w n_{\mathrm{e}} n_{\mathrm{h}}, \\
\frac{\partial n_{\mathrm{x}}}{\partial t} &= \nabla\left[D_{\mathrm{x}}\nabla n_{\mathrm{x}} + \mu_{\mathrm{x}} n_{\mathrm{x}} \nabla U_{\mathrm{x}}\right] + w n_{\mathrm{e}} n_{\mathrm{h}} - \frac{n_{\mathrm{x}}}{\tau_{\mathrm{x}}}.
\end{aligned} \tag{4.1}$$

The solution is the density distributions of electrons, holes and excitons (n_{e}, n_{h} and n_{x} respectively). The first and second terms inside each of the square brackets are the diffusion and drift currents respectively. $D_{\mathrm{e(h,x)}}$ and $\mu_{\mathrm{e(h,x)}}$ are the diffusion coefficients and mobilities. Each diffusion coefficient is assumed constant and the classical limit for the mobilities given in (2.8) is used; $\mu_{\mathrm{e(h,x)}} \approx D_{\mathrm{e(h,x)}}/(k_B T)$. Far from the laser induced heating at the excitation spot, the temperature of each species is defined by the lattice temperature, T_b. Therefore a constant temperature $T = T_b$ is used which greatly simplifies calculations. The potentials U_{e}, U_{h} and U_{x} include the Coulomb interaction potentials between each species. To capture the fragmentation of the ring in a numerical simulation, one has to solve equations (4.1) in the two-dimensional geometry with $\nabla = \partial/\partial x\, \hat{\mathbf{e}}_x + \partial/\partial y\, \hat{\mathbf{e}}_y$. This is because a fragmented ring lacks radial symmetry and is inhomogeneous in both x and y.

Equations (4.1) resemble the exciton transport equation from previous chapters. Here, the theory is extended to include free electrons and holes and their binding into indirect excitons. The remaining terms on the right hand side of equations (4.1) account for the creation and decay of each species. The homogeneous source term for electrons, which is due to a constant flux through the CQWs, acts to restore a background density, $n_{\mathrm{e}}^{(0)}$ in a characteristic time τ_{e}. Both $n_{\mathrm{e}}^{(0)}$ and τ_{e} depend on the applied electric field. To reduce the number of control parameters, control of the electric field was modeled by varying $n_{\mathrm{e}}^{(0)}$ and a fixed $\tau_{\mathrm{e}} = 50\,\mathrm{ns}$ was used which is

close to the experimentally determined value in Ref. [109]. $\Lambda(\mathbf{r})$ is the injection rate of unbound electron-hole pairs into the CQWs by the laser. The imbalance in the generation rate of electrons and holes can be incorporated by $\Lambda_e < \Lambda$. Without loss of generality, one can set $\Lambda_e = 0$ and compensate by reducing Λ. This removes the central bright spot from simulations where the inner ring is found.

The binding rate of free pairs into excitons is proportional to the overlap of the electron and hole densities. The fit parameter w is inversely proportional to the exciton formation time. Here we used $w = 10^3 \mathrm{cm}^2\mathrm{s}^{-1}$[110]. The term $w n_e n_h$ is a decay channel for electrons and holes and a source term for excitons. τ_x is the optical lifetime of excitons and is nearly constant with respect to n_x (See sec. 2.5). To simplify the model, a fixed $\tau_x = 50\,\mathrm{ns}$ was used and the effect of its dependence on temperature or electric field has not been explored. $D_x = 0.2\,\mathrm{cm}^2\mathrm{s}^{-1}$ was used for the exciton diffusion constant. This is consistent with the model used in chapter two where the effect of a QW disorder potential of $\approx 1\,\mathrm{meV}$ was included. The electron and hole diffusion constants are $D_e = 30\,\mathrm{cm}^2\mathrm{s}^{-1}$ and $D_h = 15\,\mathrm{cm}^2\mathrm{s}^{-1}$, comparable to experimentally measured values in [109].

4.3 COULOMB INTERACTIONS

The Coulomb interactions are included into equations (4.1) via the potentials U_e, U_h and U_x. For electrons and holes residing in adjacent quantum wells, one has

$$\begin{aligned} U_e &= n_e * V_0 - n_h * V_{d_z} + n_x * (V_0 - V_{d_z}), \\ U_h &= n_h * V_0 - n_e * V_{d_z} + n_x * (V_0 - V_{d_z}), \\ U_x &= (n_e + n_h + 2n_x) * (V_0 - V_{d_z}). \end{aligned} \tag{4.2}$$

The interaction potential $V_\alpha(\mathbf{r})$ with either $\alpha = 0$ or $\alpha = d_z$ is given by the Coulomb interaction,

$$V_\alpha(\mathbf{r}) = \frac{e^2}{4\pi\varepsilon_0\varepsilon_r\sqrt{|\mathbf{r}|^2 + \alpha^2}}. \tag{4.3}$$

In equation (4.2), '$*$' denotes the convolution which is written explicitly as

$$f * g = \int f(\mathbf{r} - \mathbf{r}')g(\mathbf{r}')d\mathbf{r}'. \tag{4.4}$$

Here, **r** is the in-plane coordinate. All calculations are made for $GaAs/Al_{0.33}Ga_{0.67}As$ CQWs studied in Ref.[7]. $d_z = 12\,\text{nm}$ was used for the separation between electron and hole layers and dielectric constant $\varepsilon_r = 12.9$. Macroscopic charge separation creates an in-plane potential gradient under which electrons and holes drift towards the ring position. The separation of opposite charges into adjacent wells leads to repulsion in the exciton-exciton interaction and also in the exciton-electron and exciton-hole interactions. The interactions make a significant contribution at low temperatures where transport due to Coulomb forces dominates over diffusive mechanisms.

4.4 NUMERICAL SOLUTION OF THE COUPLED TRANSPORT EQUATIONS WITH COULOMB INTERACTIONS

An explicit finite difference scheme similar to that discussed in 2.6.2 was used to evolve the density distributions according to equations (4.1). The finite difference approximation of ∇ and ∇^2 used here were modified to include derivatives in both the x and y directions. On each time step, the potentials were updated according to equations (4.2). The simulations were run until a steady state solution was achieved.

4.4.1 FAST CONVOLUTION ALGORITHM

To compute the potentials U_e, U_h and U_x given in equations (4.2), a discretized form of the two-dimensional integral given in equation (4.4) must be evaluated. Effectively, the potential of each species at each point on a grid of size $N \times N$ has a contribution from all other N^2 points. Therefore, the computation of equations (4.2) scales with N^4. Moreover, in a dynamical scheme, the potentials need to be re-evaluated on every time step as the density distributions evolve. It was found to be unfeasible to calculate the potentials directly and so a fast algorithm which makes use of the convolution theorem was used. The convolution theorem states that for two 'well behaved' distributions, f and g,

$$\hat{(f * g)} = \hat{f} \cdot \hat{g}, \tag{4.5}$$

where $\hat{f}$ denotes the Fourier transform of f. In two dimensions, this is given by

$$\hat{f}(p,q) = \int\int f(x,y)e^{-ipx}e^{-iqy}\,dx\,dy. \tag{4.6}$$

Using Fourier transforms, each convolution in equations (4.2) is performed in three steps:

1. Fourier transform both f and g to get $\hat{f}$ and $\hat{g}$.
2. Multiply together $\hat{f}$ and $\hat{g}$ which by the convolution theorem is equal to $(f \hat{*} g)$.
3. Inverse Fourier transform $(f \hat{*} g)$ to get $f * g$.

Although this appears to be a great deal more work than to just compute the convolutions directly, one can make use of fast Fourier transform libraries (e.g. FFTW). In two dimensions, the computation time of a fast Fourier transform scales with $(N \ln N)^2$ where the the discretized forms of the distributions f and g are $N \times N$ in size. This is a massive reduction in the scale of the computation from N^4 to almost N^2. For each simulation, the time independent functions $\hat{V}_0$ and $\hat{V}_d$ can be calculated once and stored. Then, on each time step, fast Fourier transforms of the densities n_e, n_h and n_x are computed and fast inverse Fourier transforms are used to obtain the potentials U_e, U_h and U_x.

4.4.2 Geometry and boundary conditions

In this study, two different excitation geometries were used. Firstly, a Gaussian profile for $\Lambda(\mathbf{r})$ was focused on the center of the grid. In this case the electron density is fixed to $n_\mathrm{e}^{(0)}$ and the hole and exciton densities to zero at a circular boundary well beyond the ring position. In the second case, a line excitation was studied so as to further understand the physical mechanism that leads to ring fragmentation. In this geometry the laser is focused not to a single point but to a narrow line extended across the entire sample. This causes the appearance of two parallel *external lines* in the indirect exciton PL pattern, either side of the laser. On the boundaries parallel to the excitation, the same fixed density conditions were used as in the point excitation geometry. On the boundaries perpendicular to the line excitation, periodic boundary conditions were used to simulate an infinitely extended excitation. In both of these

cases, the simulations use initial conditions of uniform density $n_{\mathrm{e}} = n_{\mathrm{e}}^{(0)}$ and $n_{\mathrm{h}} = n_{\mathrm{x}} = 0$.

Regardless of the excitation geometry, one has to account for the infinite sea of electrons present in the CQW plane and its effect on charge transport. Discretizing equations (4.1) onto a grid of finite size only accounts for the free electron gas within the simulation boundaries. This was dealt with by calculating the folowing background potentials,

$$\begin{aligned} U_b^{(\mathrm{e})} &= n_{\mathrm{e}} * V_0, \\ U_b^{(\mathrm{h})} &= -n_{\mathrm{e}} * V_{d_z}, \\ U_b^{(\mathrm{x})} &= n_{\mathrm{e}} * (V_0 - V_{d_z}), \end{aligned} \tag{4.7}$$

with n_{e} equal to $n_{\mathrm{e}}^{(0)}$ everywhere. On each time step, these background potentials were added to the respective interaction potentials. The result is that in the absence of any laser excitation, the simulated electron density remains at a constant ($n_{\mathrm{e}}^{(0)}$) in both space and time.

4.5 RESULTS

Fig. 4.1 shows the spatial density distributions satisfying equations (4.1) and (4.2). An optical pump of FWHM 10 μm is focused at the origin with peak generation rate of $2\times10^{10}\mathrm{cm}^{-2}\mathrm{ns}^{-1}$. Background electron density was $n_{\mathrm{e}}^{(0)} = 0.5 \times 10^{9}\mathrm{cm}^{-2}$. The density of electrons (a), holes (b) and indirect excitons (c) show a periodic modulation along the ring. Additionally, a slight modulation of the ring radius is seen which is not observed in experiments. Fig. 4.1d and Fig. 4.1e show cross sections along the line $y = 0$ for the density distributions and potentials respectively. The pump profile is shown by black dots in Fig. 4.1d. In-plane charge separation causes an E-field of $\approx 2\,\mathrm{eVcm}^{-1}$ driving electrons and holes to the ring position thus enhancing the generation rate of excitons.

A feature of the experimental data which is well reproduced by the model is the dependence of the ring fragmentation on the lattice temperature. Fragmentation is observed only below a critical temperature [8, 94]. This has been interpreted as the indirect exciton degeneracy temperature where the statistics cross from the classical to the quantum regime [96]. In the model, the lattice temperature T appears in the

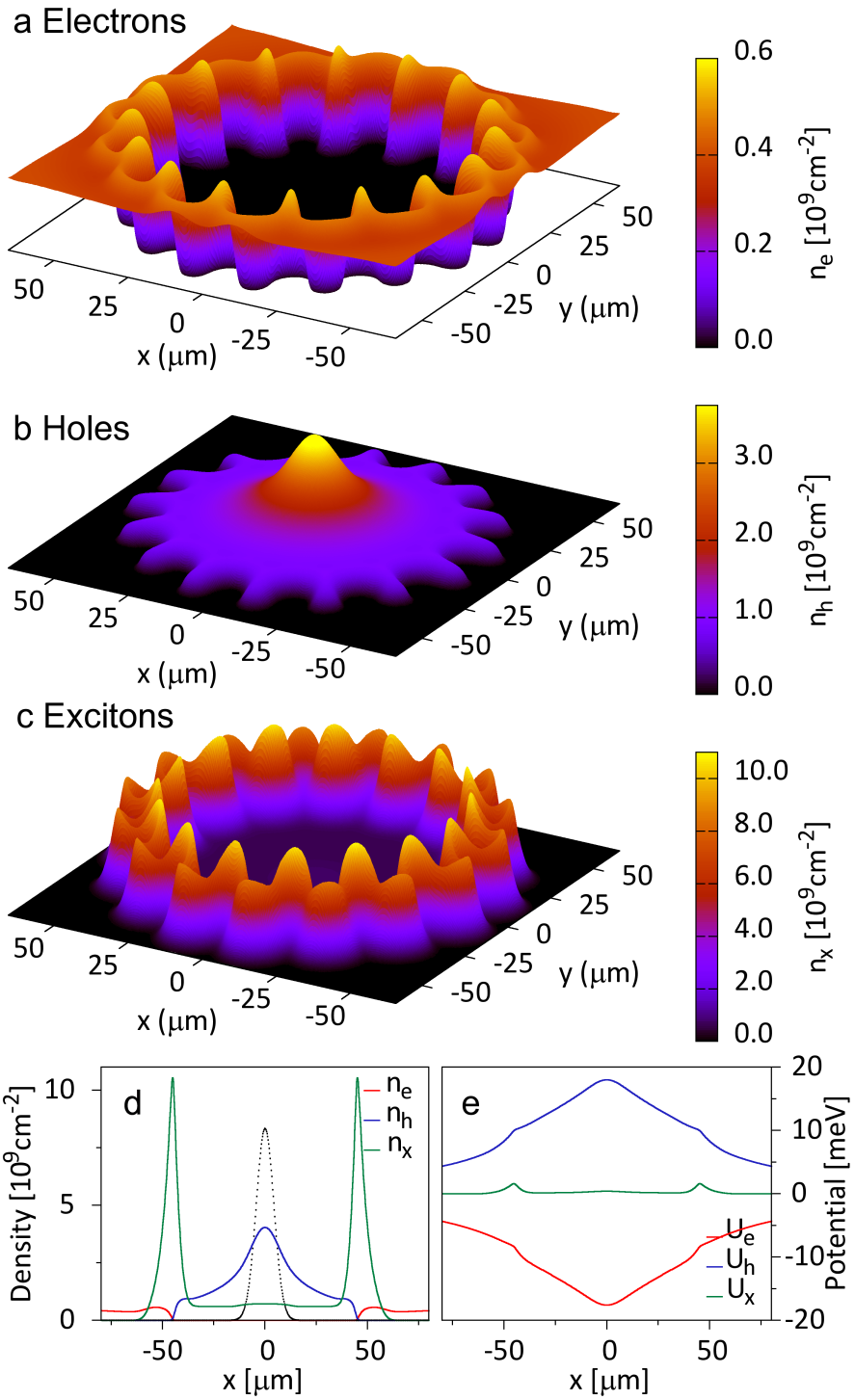

Figure 4.1: Spatial density distributions of electrons (a), holes (b) and indirect excitons (c) in the external ring. Cross-sections along $y = 0$ are shown for densities in (d) and potentials in (e). The excitation profile is shown by the black dotted line in (d).

denominator of the interaction terms which, as a result, become greater in magnitude than the diffusive terms for $\nabla U_i > k_\mathrm{B}T(\nabla n_i)/n_i$ where $i = \mathrm{e}, \mathrm{h}, \mathrm{x}$.

The temperature dependence of the simulated external ring is presented in Fig. 4.2. The inset in Fig. 4.2a shows the exciton density profile at the ring position, r_ring for various temperatures indicated by arrows in the main panel. The ring position is defined as the location of maximum exciton density for each angle θ about the excitation spot. Ring fragmentation appears with decreasing temperature as the drift currents dominate over the diffusive currents. This is illustrated in the main panel where the average contrast between the peaks and dips along the ring is plotted against T. The ring contrast is quantified by $\langle (I_\mathrm{PL}^\mathrm{max} - I_\mathrm{PL}^\mathrm{min})/I_\mathrm{PL}^\mathrm{max} \rangle$ where $I_\mathrm{PL}^\mathrm{max}$ is the maximum density on each island of the fragmented ring and $I_\mathrm{PL}^\mathrm{min}$ is the minimum density between each peak. The model captures the temperature dependence of the pattern formation observed in experiments [8, 94]. The onset of fragmentation is abrupt and a critical temperature can be identified. This temperature is deceivingly low and could be misinterpreted as the degeneracy temperature. The critical temperature varies with exciton density which can be controlled by adjusting Λ and $n_\mathrm{e}^{(0)}$ simultaneously whilst maintaining a fixed average radius. Each curve corresponds to a different value of $n_\mathrm{e}^{(0)}$ with Λ chosen to give a radius of $50\,\mu$m. The seemingly noisy data in Fig. 4.2a is a consequence of the state of the ring evolving to configurations with different numbers of islands. The *degenerate* solutions have slightly different contrasts and the effect is most pronounced at the highest density.

Fig. 4.2b shows the spatially averaged density in the ring against temperature for different values of $n_\mathrm{e}^{(0)}$. The dashed line marks the average density at each critical temperature. Also shown is the line $T = T_0$ where T_0 is the exciton degeneracy temperature repeated here for clarity:

$$T_0 = \frac{\pi\hbar^2 n_\mathrm{x}}{2M_\mathrm{x}k_\mathrm{B}}. \tag{4.8}$$

The model predicts that fragmentation can occur both below and well above T_0. At the highest densities examined, an increase in exciton density is observed as the temperature is further reduced beyond the onset of fragmentation. In PL experiments, this manifests itself as an increase in the blue shift in the exciton spectrum which has been observed in Ref. [94]. In that work, the blue shift was found to also increase with temperature when above the critical temperature. The model would be consistent with this if the temperature dependent τ_x described in [45] was used.

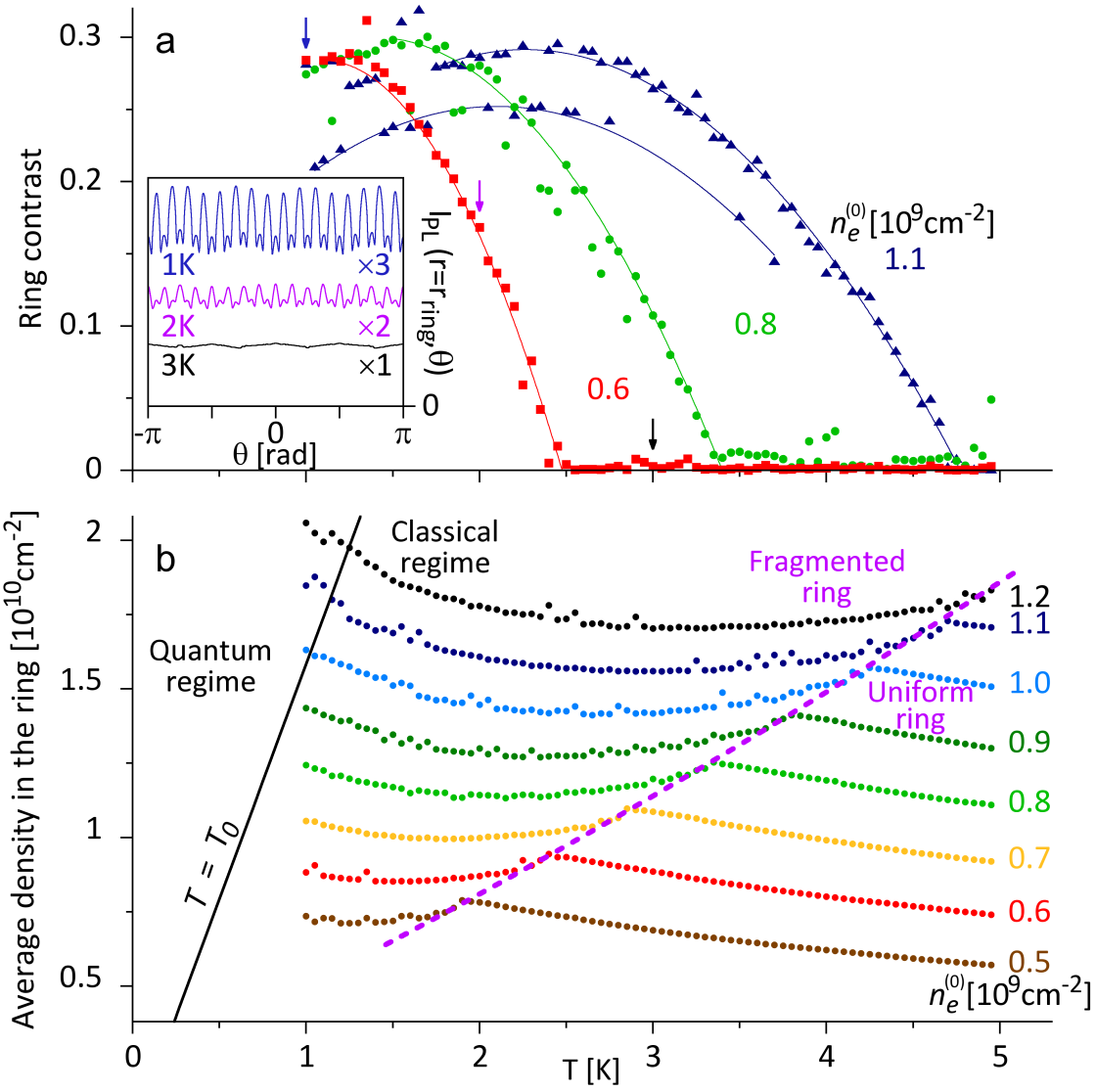

Figure 4.2: Ring contrast (a) and average density (b) in the external ring against temperature for various $n_e^{(0)}$. The generation rate is adjusted to give a fixed ring radius. The inset in (a) shows profiles along the external ring corresponding to simulations indicated by the arrows on the red curve in the main panel. The solid line in (b) shows crossing between classical and quantum regimes. The dashed line shows the transition between a uniform and fragmented ring.

Due to doping, there is an abundance of free electrons in the layers surrounding the CQWs. Arguably, these electrons may accumulate around the excitation spot to screen the in-plane potentials U_e and U_h which would suggest that Coulomb interactions are not prominent enough to be responsible for the fragmentation of the ring. However, on comparison of available experimental data, an alternative picture presents itself. Ring fragmentation is seen in the work of Butov *et al.*[8], but not in the work by Snoke *et al.*[7], where it is estimated that a much greater density of free electrons is present in the layers adjacent to the CQWs. From this, one can deduce that in the former there are insufficient free electrons to screen the Coulomb interactions and prevent ring fragmentation. The detailed effect of a free electron gas in the adjacent layers is beyond the scope of this work and its effect on pattern formation is an open question.

To further understand the physical mechanism that leads to ring fragmentation, it is instructive to examine the case of a line excitation. In this geometry the laser is focused to a narrow infinitely extended line and leads to the appearance of two parallel *external lines* in the indirect exciton PL pattern, either side of the laser.

In Fig. 4.3, results are presented for this situation. The laser has a Gaussian profile in the y direction and is homogeneous in the x direction. Periodic boundaries along the lines $x = \pm 128\mu$m are used to simulate an infinitely extended line. The background electron density was $n_\mathrm{e}^{(0)} = 10^9\,\mathrm{cm}^{-2}$. Unlike the external ring in the point excitation geometry, the external line does not spontaneously fragment. Instead, a small perturbation is needed to observe the effect. This is included by adding a random disorder potential to either U_e, U_h or U_x. The density distributions in Figs. 4.3b and 4.3a are from simulations with and without a disorder perturbation via the electron potential U_e, respectively. The amplitude of the disorder potential used, $A_\mathrm{rand} = 1\,\mu$eV is orders of magnitude smaller than the fluctuations in U_e along the external line and the correlation length of the disorder (2μm) is a few times less than the period of density modulation. This confirms that the density modulation is not correlated to the disorder but disorder is required to evolve the state of the line from the metastable solution shown in Fig 4.3a to the stable solution shown in Fig 4.3b. In the circular geometry, the numerical discretization of equations (4.1) and (4.2) onto a rectangular grid provides some implicit distortion that triggers the fragmentation.

Fig. 4.3c shows the exciton density at the line position with and without disorder. A consequence of fragmentation is the reduction in the exciton density and,

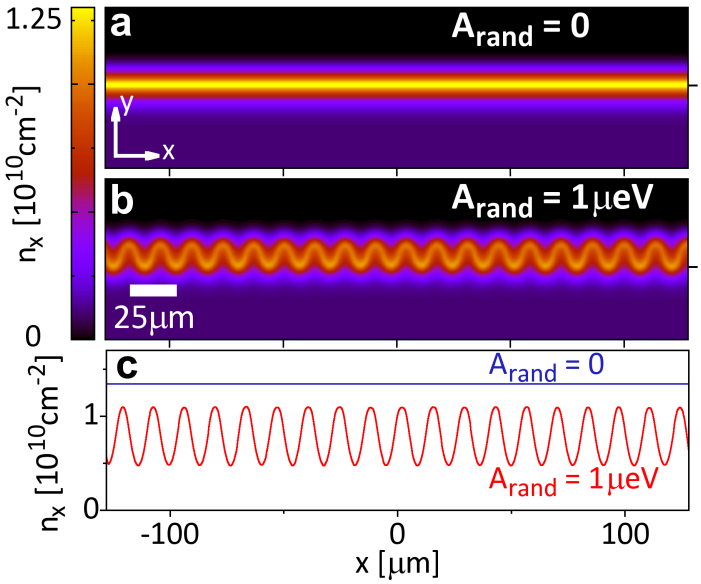

Figure 4.3: Exciton density distribution due to a line excitation with (b) and without (a) a random disorder potential for $T = 1\,\mathrm{K}$. The profile along the external line for these two cases is shown in (c).

therefore, a lowering of the energy density associated with the dipole repulsion between excitons. It can be concluded that in the simulations, the external line buckles into a wavy line in order to redistribute excitons over a larger area and reduce the energy density. It was found that any non-zero perturbation triggers an energy minimization process, leading to fragmentation of the line.

4.6 SUMMARY

In summary, the model presented provides insight into the role of Coulomb interactions in the formation of the external ring in the indirect exciton PL pattern. In this chapter it was demonstrated that within a classical framework, periodic modulation of the exciton density on macroscopic length scales can occur. In the classical picture, fragmentation is a process of redistributing charges to minimize the potential energy associated with dipole repulsion. Strong similarities were found with the available experimental data. In particular, the calculated temperature dependence of the ring contrast is in strong agreement.

5 Conclusions

This chapter contains a summary of the results and conclusions presented this thesis. Possible avenues of future research extending from these ideas are also discussed.

5.1 The inner ring and PL-jump in the exciton emission pattern

The inner ring in the exciton emission pattern was described in chapter two. Its appearance was explained in terms of laser induced heating within the vicinity of the excitation spot. The heating leads to suppression of the optical decay rate of indirect excitons and manifests itself as a dip in PL intensity and hence the apparent ring around the excitation spot. Simulations of the inner ring was performed using a model based on the creation, transport, thermalisation and optical decay of indirect excitons in CQWs. The presented results showed in detail the space-time evolution of the exciton density, temperature, diffusion constant and optical lifetime following activation of the laser excitation. Comparison with available experimental data showed a quantitative agreement with the theory for specific fitting parameters of the model.

The dependence of the inner ring contrast on the laser excitation energy was studied. In agreement with experimental observations, it was found that increasing the energy of photons injected into the CQWs leads to increased contrast of the inner ring. The simulations confirmed that in exciton PL experiments, the inner ring contrast enables direct observation of the exciton temperature. This is a vital tool

for finding the optimum conditions to create a cold and dense exciton gas.

The dynamics of the inner ring following termination of the laser excitation were studied. The simulations quantitatively reproduce the dynamics of the PL-jump as observed in experiments. The PL-jump feature was attributed to rapid cooling of a dense exciton gas following the abrupt deactivation of the heating source formerly provided by the laser. The contrast of the PL-jump was found to follow closely the laser profile and hence the temperature profile of the exciton gas.

5.2 Control of exciton transport via applied electrostatic potentials

In chapter three, the model described in chapter two was extended to include the effect on exciton transport of externally applied in-plane electric fields. Simulations were performed in the context of an experiment where indirect excitons were created on a ramp potential. In agreement with the experimental data, the modeling showed a shift of the exciton cloud in the direction corresponding to the low energy, bottom end of the ramp. The temperature and excitation density dependence of the effectiveness of exciton transport down the ramp were described in terms CQW disorder. At high temperatures, excitons are not easily localised by the disorder potential and are efficiently transported by the ramp. At low densities, excitons are localised to minima of the disorder potential. However, their accumulation to these minima causes screening of the disorder potential. For higher densities, the additional excitons move freely through the screened in-plane disorder potential leading to improved transport via the ramp.

The dynamics of exciton transport via an electrostatic conveyer was also studied in this chapter. To facilitate an extensive numerical study of exciton transport in a propagating lattice potential, some simplifications were made to the theoretical model compared to that used in previous sections. It was found that excitons transport to the minima of the conveyer potential and are then carried along the QW plane by the conveyer. Combined with the experimental evidence, the numerical studies provided a deep insight into the transport dynamics of excitons. It was found that the dependence of the average exciton transport distance via the conveyer on conveyer velocity and amplitude and exciton density are all well explained using

only a drift-diffusion equation. Even the more complex features of the experimental data like the dynamical localisation-delocalisation transition are contained with the simplified model of exciton transport used.

5.3 Fragmentation of the external ring in the exciton emission pattern

The external ring in the indirect exciton emission pattern was studied in chapter four. A model based on the creation, transport and decay of three species, namely electrons, hole and excitons was employed to model the appearance of the external ring. As concluded by others in previous studies, it was demonstrated that the external ring appears at the interface between electron-rich and hole-rich regions. The electrons and holes bind forming excitons which are subsequently observed by their optical decay. In the study presented, the full set of Coulomb interactions between all three species was included into the drift terms of the respective transport equations. The transport equations were then solved dynamically in a two dimensional geometry. It was found that the intricate interactions between electrons, holes and excitons leads to an instability in the external ring. Triggered by any non-zero perturbation, the system reorganizes itself into a more energy efficient configuration which involves a modulation of the exciton density along the ring.

Multiple repetitions of the simulation for different temperatures, background electron densities and laser powers showed that the model reproduces qualitatively the main features of the external ring shown in previous experimental studies. In particular, the temperature dependence of the ring contrast is in strong agreement. The model predicts that ring fragmentation is a low temperature phenomenon occurring abruptly when the system is cooled below a critical temperature. Through studying the density dependence of the external ring fragmentation, it was found that the fragmented state can appear both above and below the indirect exciton quantum degeneracy temperature. This is in contrast to previous explanations of the origin of fragmentation which argue that it is a signature of novel quantum effects and possibly exciton BEC.

5.4 Future work

The physics of CQW excitons described in this thesis is rich in its complexity. Many interesting non-linear features have been discussed and a deep insight gained. A natural progression for the direction of indirect exciton research is to begin to harness these unique features to create some technological advancement. Some such progress in this area has already been made in the form optical and optoelectronic transistors [83, 84]. However, the system discussed in this thesis is one that is particularly suited to a low temperature regime where exciton condensation is expected. It would be of interest to examine different materials and CQW structures where excitons are stable at room temperature and to understand how the physics translates to this regime. For example, the creation of a fast room temperature optical transistor would have a significant impact on the wider society because of its potential for application in optical communications which is a ubiquitous technology of the modern world.

Appendix A Derivation of the quantum mass action law

The quantum mass action law is derived by analyzing a Boltzmann kinetic equation for the scattering of free electrons and holes into excitons and vice versa. The collision integrand in the kinetic equation is proportional to

$$\left[N^{\mathrm{e}}_{\mathbf{l}} N^{\mathrm{h}}_{\mathbf{k}} (N^{\mathrm{x}}_{\mathbf{p}} + 1) - (1 - N^{\mathrm{e}}_{\mathbf{l}})(1 - N^{\mathrm{h}}_{\mathbf{k}}) N^{\mathrm{x}}_{\mathbf{p}}\right] \delta(E^{\mathrm{e}}_{\mathbf{l}} + E^{\mathrm{h}}_{\mathbf{k}} - E^{\mathrm{x}}_{\mathbf{p}} + E_b), \tag{A.1}$$

with $N^{\mathrm{e(h,x)}}_{\mathbf{p}}$ and $E^{\mathrm{e(h,x)}}_{\mathbf{p}}$ the occupation number and energy of a particle with in-plane momentum $\mathbf{p}$, respectively and E_b is the exciton binding energy. Equating equation (A.1) to zero corresponds to the steady state Boltzmann equation which is relevant when the distribution of electron-hole pairs in the unbound and bound exciton states is in equilibrium. By direct substitution, one finds that the solution of the collision integrand (A.1) equal to zero is given by the Fermi-Dirac distribution for electrons and holes and the Bose-Einstein distribution for excitons.

$$N^{\mathrm{e(h)}}_{\mathbf{p}} = \frac{1}{\exp[(E^{\mathrm{e(h)}}_{\mathbf{p}} - \mu_{\mathrm{e(h)}})/(k_B T)] + 1}, \tag{A.2}$$

$$N^{\mathrm{x}}_{\mathbf{p}} = \frac{1}{\exp[(E^{\mathrm{x}}_{\mathbf{p}} - \mu_{\mathrm{x}})/(k_B T)] - 1}. \tag{A.3}$$

The distribution functions are solutions provided that there is the following relationship between chemical potentials, $\mu^{(i)}$, of electrons, holes and excitons ($i = \mathrm{e}, \mathrm{h}, \mathrm{x}$ respectively),

$$\mu^{(\mathrm{x})} - E_b = \mu^{(\mathrm{e})} + \mu^{(\mathrm{h})}. \tag{A.4}$$

The chemical potential of each species is evaluated by summing the occupation number over all possible momentum states to acquire the density:

$$n_{\mathrm{x}} = \frac{4}{(2\pi\hbar)^2}\sum_{p} N_p^{\mathrm{x}} = \frac{4}{(2\pi\hbar)^2}\int_{-\pi}^{\pi} d\theta \int_0^{\infty} dp \frac{p}{\exp[(p^2/2m - \mu^{(\mathrm{x})})/(k_{\mathrm{B}}T)] - 1}, \quad \text{(A.5)}$$

$$n_{\mathrm{e(h)}} = \frac{2}{(2\pi\hbar)^2}\sum_{p} N_p^{\mathrm{e(h)}} = \frac{2}{(2\pi\hbar)^2}\int_{-\pi}^{\pi} d\theta \int_0^{\infty} dp \frac{p}{\exp[(p^2/2m - \mu^{(\mathrm{e(h)})})/(k_{\mathrm{B}}T)] + 1}. \quad \text{(A.6)}$$

Evaluating the integrals (A.5) and (A.6) reveals the chemical potentials,

$$\mu^{(\mathrm{x})} = k_{\mathrm{B}}T \ln(1 - e^{-T_0/T}), \quad \text{(A.7)}$$

$$\mu^{(\mathrm{e(h)})} = k_{\mathrm{B}}T \ln(e^{T_0^{\mathrm{e(h)}}/T} - 1), \quad \text{(A.8)}$$

where the quantum degeneracy temperature of electrons (holes) with effective mass $m_{\mathrm{e(h)}}$ is given by

$$T_0^{\mathrm{e(h)}} = \frac{\pi\hbar^2}{m_{\mathrm{e(h)}}k_{\mathrm{B}}} n_{\mathrm{e(h)}}. \quad \text{(A.9)}$$

By substituting the chemical potentials (A.7) and (A.8) into the relationship (A.4), one arrives at the following equation for the equilibrium exciton density, $n_{\mathrm{x}}^{(\mathrm{eq})}$,

$$n_{\mathrm{x}}^{(\mathrm{eq})} = \frac{k_{\mathrm{B}}M_{\mathrm{x}}T}{2\pi\hbar^2} \ln[1 - e^{-E_b/k_{\mathrm{B}}T}(e^{T_0^{\mathrm{e}}/T} - 1)(e^{T_0^{\mathrm{h}}/T} - 1)]. \quad \text{(A.10)}$$

Equation (A.10) is the quantum mass action law which describes the equilibrium balance between the concentrations of excitons and free electron-hole pairs.

Appendix B Derivation of the exciton optical lifetime

The intrinsic radiative lifetime, τ_r of a ground state QW exciton with zero in-plane momentum depends only on the choice of materials, QW structure and the electric field applied in the growth direction. However, to include the fact that only low energy excitons with momentum inside the light cone may decay optically one must evaluate the density of optically active excitons. This is done by summing the product of the exciton occupation number and the photon density of states over the range $0 \leq p \leq p_\gamma$ where p is the in-plane exciton momentum and p_γ marks the edge of the light cone. Hence the density of optically active in-plane transverse polarized QW excitons is given by,

$$n_{\text{opt}}^{(T)} = \frac{1}{2}\frac{g}{(2\pi\hbar)^2}\sum_p N_p^{\text{x}}\rho_\gamma^{(T)}(p) \tag{B.1}$$

N_p^{x} is the Bose-Einstein occupation number given in equation (A.3). The photon density of states $\rho_\gamma^{(T)}$ is given by [111],

$$\rho_\gamma^{(T)}(p) = \frac{p_\gamma}{\sqrt{p_\gamma^2 - p^2}}\theta(p_\gamma - p). \tag{B.2}$$

Here, p_γ is the momentum corresponding to the point at which the exciton and photon dispersion intersect. It is related to E_γ by $E_\gamma = p_\gamma^2/2M_{\text{x}}$. The step function $\theta(x)$ includes the fact that only excitons with momentum inside the light cone (i.e. $p < p_\gamma$) can decay optically. It is given by

$$\theta(x) = \begin{cases} 1 & \text{if } x > 0, \\ 0 & \text{if } x < 0. \end{cases} \tag{B.3}$$

Equation (B.1) can be evaluated in integral form as

$$n_{\rm opt}^{(T)} = \frac{1}{2}\frac{g}{(2\pi\hbar)^2}\int_{-\pi}^{\pi} d\phi \int_0^{p_\gamma} p\,dp \frac{1}{e^{-\mu^{(\rm x)}/k_{\rm B}T} e^{p^2/2M_{\rm x}k_{\rm B}T} - 1}\frac{p_\gamma}{\sqrt{p_\gamma^2 - p^2}}. \tag{B.4}$$

By making the substitution $z^2 = 1-(p/p_\gamma)^2$ and using the expression for the chemical potential $\mu^{(\rm x)}$ given by equation (A.7), this reduces to

$$n_{\rm opt}^{(T)} = \frac{E_\gamma n_{\rm x}}{k_{\rm B}T_0}\int_0^1 \frac{dz}{Ae^{-z^2E_\gamma/k_{\rm B}T} - 1}, \tag{B.5}$$

where $A(T_0, T) = e^{E_\gamma/k_{\rm B}T}/(1 - e^{-T_0/T})$. Following the same method, the density of optically active in-plane longitudinal polarized excitons, $n_{\rm opt}^{(L)}$ can be evaluated by replacing $\rho_\gamma^{(T)}$ with $\rho_\gamma^{(L)}$ which is given by [111],

$$\rho_\gamma^{(L)}(p) = \frac{\sqrt{p_\gamma^2 - p^2}}{p_\gamma}\theta(p_\gamma - p). \tag{B.6}$$

Finally, the decay rate is the product of the intrinsic decay rate and the fraction of excitons which are optically active. Or, in terms of the lifetime, this is

$$\begin{aligned}\frac{1}{\tau_{\rm opt}} &= \frac{1}{2\tau_r}\frac{n_{\rm opt}^{(T)} + n_{\rm opt}^{(L)}}{n_{\rm x}} \\ &= \frac{1}{2\tau_r}\frac{E_\gamma}{k_{\rm B}T_0}\int_0^1 \frac{1+z^2}{Ae^{-z^2E_\gamma/k_{\rm B}T} - 1}dz.\end{aligned} \tag{B.7}$$

To evaluate the exciton lifetime dependence on the exciton in-plane group velocity ν_g as discussed in Sec. 3.3, one must re-evaluate $n_{\rm opt}^{(T)}$ and $n_{\rm opt}^{(L)}$ for a macroscopic shift in the momentum along one of the in-plane coordinates. Equation (B.1) becomes

$$n_{\rm opt}^{(T)} = \frac{1}{2}\frac{g}{(2\pi\hbar)^2}\sum_p N_{p+p_g}^{\rm x}\rho_\gamma^{(T)}(p) \tag{B.8}$$

where $p_g = M_{\rm x}\nu_g$. Using the substitution $y = (M_{\rm x}\nu_g^2)/(2E_\gamma)$, the expression for $\tau_{\rm opt}$ reduces to

$$\frac{1}{\tau_{\rm opt}} = \frac{E_\gamma}{4\pi\tau_r k_{\rm B}T_0}\int_{z_{\rm a}}^1 dz\int_0^{2\pi} d\phi \frac{1+z^2}{A\exp[E_\gamma(1 - z^2 + y - 2\sqrt{y(1-z^2)}\cos\phi)/k_{\rm B}T] - 1}. \tag{B.9}$$

References

[1] L. V. Keldysh and A. N. Kozlov, "Collective properties of excitons in semiconductors," *Sov. Phys. JETP*, vol. 27, p. 521, 1968.

[2] L. L. Chase, N. Peyghambarian, G. Grynberg, and A. Mysyrowicz, "Evidence for Bose-Einstein condensation of biexcitons in CuCl," *Phys. Rev. Lett.*, vol. 42, p. 1231, 1979.

[3] J. L. Lin and J. P. Wolfe, "Bose-Einstein condensation of paraexcitons in stressed Cu2O," *Phys. Rev. Lett.*, vol. 71, p. 1222, 1993.

[4] M. H. Anderson, J. R. Ensher, M. R. Matthews, C. E. Wieman, and E. A. Cornell, "Observation of Bose-Einstein condensation in a dilute atomic vapor," *Science*, vol. 269, p. 198, 1995.

[5] J. Kasprzak, M. Richard, S. Kundermann, A. Baas, P. Jeambrun, J. M. J. Keeling, F. M. Marchetti, M. H. Szymańska, R. André, J. L. Staehli, V. Savona, P. B. Littlewood, B. Deveaud, and L. S. Dang, "BoseEinstein condensation of exciton polaritons," *Nature*, vol. 443, p. 409, 2006.

[6] E. A. Cerda-Méndez, D. N. Krizhanovskii, M. Wouters, R. Bradley, K. Biermann, K. Guda, R. Hey, P. V. Santos, D. Sarkar, and M. S. Skolnick, "Polariton condensation in dynamic acoustic lattices," *Phys. Rev. Lett.*, vol. 105, p. 116402, 2010.

[7] D. Snoke, S. Denev, Y. Liu, L. Pfeiffer, and K. West, "Long-range transport in excitonic dark states in coupled quantum wells," *Nature*, vol. 418, p. 754, 2002.

[8] L. V. Butov, A. C. Gossard, and D. S. Chemla, "Macroscopically ordered state in an exciton system," *Nature*, vol. 418, p. 751, 2002.

[9] A. T. Hammack, L. V. Butov, L. Mouchliadis, A. L. Ivanov, and A. C. Gossard, "Kinetics of indirect excitons in an optically-induced trap in GaAs quantum wells," *Phys. Rev. B*, vol. 76, p. 193308, 2007.

[10] Z. Vörös, D. W. Snoke, L. Pfeiffer, and K. West, "Trapping excitons in a two-dimensional in-plane harmonic potential: Experimental evidence for equilibration of indirect excitons," *Phys. Rev. Lett.*, vol. 97, p. 016803, 2006.

[11] L. V. Butov, C. W. Lai, A. L. Ivanov, A. C. Gossard, and D. S. Chemla, "Towards Bose-Einstein condensation of excitons in potential traps," *Nature*, vol. 417, p. 47, 2002.

[12] J. P. Eisenstein and A. H. MacDonald, "BoseEinstein condensation of excitons in bilayer electron systems," *Nature*, vol. 432, p. 694, 2004.

[13] A. A. High, J. R. Leonard, A. T. Hammack, M. M. Fogler, L. V. Butov, A. V. Kavokin, K. L. Campman, and A. C. Gossard, "Spontaneous coherence in a cold exciton gas," *Nature*, vol. 483, p. 584, 2012.

[14] A. A. High, J. R. Leonard, M. Remeika, L. V. Butov, M. Hanson, and A. C. Gossard, "Condensation of excitons in a trap," *Nano Lett.*, vol. 12, p. 2605, 2012.

[15] D. Semkat, S. Sobkowiak, G. Manzke, and H. Stolz, "Comment on "condensation of excitons in a trap"," *Nano Lett.*, vol. 12, p. 5055, 2012.

[16] L. Mouchliadis, C. W. Lai, and A. L. Ivanov, "Electric current induced anti-traps for indirect excitons," *Superlattices and Microstructures*, vol. 41, p. 392, 2007.

[17] L. Mouchliadis and A. L. Ivanov, "Anti-trapping of indirect excitons by a current filament," *J. Phys.: Cond. Matt.*, vol. 19, p. 295215, 2007.

[18] M. Fox, *Optical Properties of Solids*. Oxford University Press, 2001.

[19] Z. Vörös, R. Balili, D. W. Snoke, L. Pfeiffer, and K. West, "Long-distance diffusion of excitons in double quantum well structures," *Phys. Rev. Lett.*, vol. 94, p. 226401, 2005.

[20] L. V. Butov, "Cold exciton gases in coupled quantum well structures," *J. Phys.: Cond. Matt.*, vol. 19, p. 295202, 2007.

[21] D. W. Snoke, "Coherence and optical emission from bilayer exciton condensates," *Adv. Cond. Matt. Phys.*, vol. 2011, p. 938609, 2011.

[22] X. Zhu, P. B. Littlewood, M. S. Hybertsen, and T. M. Rice, "Exciton condensate in semiconductor quantum well structures," *Phys. Rev. Lett.*, vol. 74, p. 1633, 1995.

[23] R. Rapaport, G. Chen, and S. Simon, "Nonlinear dynamics of a dense two-dimensional dipolar exciton gas," *Phys. Rev. B*, vol. 73, p. 033319, 2005.

[24] A. L. Ivanov, "Quantum diffusion of dipole-oriented indirect excitons in coupled quantum wells," *Europhys. Lett.*, vol. 59, p. 586, 2002.

[25] Z. Vörös, D. W. Snoke, L. Pfeiffer, and K. West, "Direct measurement of exciton-exciton interaction energy," *Phys. Rev. Lett.*, vol. 103, p. 016403, 2009.

[26] B. Laikhtman and R. Rapaport, "Exciton correlations in coupled quantum wells and their luminescence blue shift," *Phys. Rev. B*, vol. 80, p. 195313, 2009.

[27] K. Cohen, R. Rapaport, and P. Santos, "Remote dipolar interactions for objective density calibration and flow control of excitonic fluids," *Phys. Rev. Lett.*, vol. 106, p. 126402, 2011.

[28] O. L. Berman, Y. E. Lozovik, D. W. Snoke, and R. D. Coalson, "Collective properties of indirect excitons in coupled quantum wells in a random field," *Phys. Rev. B*, vol. 70, p. 235310, 2004.

[29] R. Zimmermann, "Probing exciton condensation by speckled emission," *Solid State Commun.*, vol. 134, p. 43, 2005.

[30] S. Zimmermann, A. O. Govorov, W. Hansen, and J. P. Kotthaus, "Lateral superlattices as voltage-controlled traps for excitons," *Phys. Rev. B*, vol. 56, p. 13414, 1997.

[31] A. T. Hammack, N. A. Gippius, S. Yang, G. O. Andreev, L. V. Butov, M. Hanson, and A. C. Gossard, "Excitons in electrostatic traps," *J. Appl. Phys.*, vol. 99, p. 066104, 2006.

[32] A. A. High, A. K. Thomas, G. Grosso, M. Remeika, A. T. Hammack, A. D. Meyertholen, M. M. Fogler, L. Butov, M. Hanson, and A. C. Gossard, "Trapping indirect excitons in a GaAs quantum-well structure with a diamond-shaped electrostatic trap," *Phys. Rev. Lett.*, vol. 103, p. 087403, 2009.

[33] G. J. Schinner, E. Schubert, M. P. Stallhofer, J. P. Kotthaus, D. Schuh, A. K. Rai, D. Reuter, A. D. Wieck, and A. O. Govorov, "Electrostatically trapping indirect excitons in coupled $In_xGa_{1-x}As$ quantum wells," *Phys. Rev. B*, vol. 83, p. 165308, 2011.

[34] A. Gärtner, L. Prechtel, D. Schuh, A. W. Holleitner, and J. P. Kotthaus, "Micropatterned electrostatic traps for indirect excitons in coupled gaas quantum wells," *Phys. Rev. B*, vol. 76, p. 085304, 2007.

[35] A. A. High, A. T. Hammack, L. V. Butov, L. Mouchliadis, A. L. Ivanov, M. Hanson, and A. C. Gossard, "Indirect excitons in elevated traps," *Nano Lett.*, vol. 9, p. 2094, 2009.

[36] M. Remeika, J. C. Graves, A. T. Hammack, A. D. Meyertholen, M. M. Fogler, L. Butov, M. Hanson, and A. C. Gossard, "Localization-delocalization transition of indirect excitons in lateral electrostatic lattices," *Phys. Rev. Lett.*, vol. 102, p. 186803, 2009.

[37] A. Gärtner, D. Schuh, and J. P. Kotthaus, "Dynamics of long-living excitons in tunable potential landscapes," *Physica E*, vol. 32, p. 195, 2006.

[38] M. Remeika, M. M. Fogler, L. V. Butov, M. Hanson, and A. C. Gossard, "Two-dimensional electrostatic lattices for indirect excitons," *Appl. Phys. Lett.*, vol. 100, p. 061103, 2012.

[39] A. G. Winbow, J. R. Leonard, M. Remeika, Y. Y. Kuznetsova, A. A. High, A. T. Hammack, L. Butov, J. Wilkes, A. A. Guenther, A. L. Ivanov, M. Hanson, and A. C. Gossard, "Electrostatic conveyer for excitons," *Phys. Rev. Lett.*, vol. 106, p. 196806, 2011.

[40] J. R. Leonard, M. Remeika, M. K. Chu, Y. Y. Kuznetsova, A. A. High, L. V. Butov, J. Wilkes, M. Hanson, and A. C. Gossard, "Transport of indirect excitons in a potential energy gradient," *Appl. Phys. Lett.*, vol. 100, p. 231106, 2012.

[41] A. Gärtner, A. W. Holleitner, J. P. Kotthaus, and D. Schuh, "Drift mobility of long-living excitons in coupled GaAs quantum wells," *Appl. Phys. Lett.*, vol. 89, p. 052108, 2006.

[42] A. A. High, E. E. Novitskaya, L. V. Butov, and A. C. Gossard, "Control of exciton fluxes in an excitonic integrated circuit," *Science*, vol. 321, p. 229, 2008.

[43] X. P. Vögele, D. Schuh, W. Wegscheider, J. P. Kotthaus, and A. W. Holleitner, "Density enhanced diffusion of dipolar excitons within a one-dimensional channel," *Phys. Rev. Lett.*, vol. 103, p. 126402, 2009.

[44] A. L. Ivanov, C. Ell, and H. Haug, "Phonon-assisted boltzmann kinetics of a bose gas: Generic solution for $T \leq T_c$," *Phys. Rev. E*, vol. 55, p. 6363, 1997.

[45] A. L. Ivanov, L. E. Smallwood, A. T. Hammack, S. Yang, L. V. Butov, and A. C. Gossard, "Origin of the inner ring in photoluminescence patterns of quantum well excitons," *Europhys. Lett.*, vol. 73, p. 920, 2006.

[46] A. L. Ivanov, "Thermalization and photoluminescence dynamics of indirect excitons at low bath temperatures," *J. Phys.: Condens. Matter*, vol. 16, p. S3629, 2004.

[47] J. Wilkes, L. Mouchliadis, E. A. Muljarov, A. L. Ivanov, A. T. Hammack, L. V. Butov, and A. C. Gossard, "Dynamics of the inner ring in photoluminescence of GaAs/AlGaAs indirect excitons," *J. Phys.: Conf. Series*, vol. 210, p. 012050, 2010.

[48] A. T. Hammack, L. V. Butov, J. Wilkes, L. Mouchliadis, E. A. Muljarov, A. L. Ivanov, and A. C. Gossard, "Kinetics of the inner ring in the exciton emission pattern in gaas coupled quantum wells," *Phys. Rev. B*, vol. 80, p. 155331, 2009.

[49] Y. Y. Kuznetsova, J. R. Leonard, L. V. Butov, J. Wilkes, E. A. Muljarov, K. L. Campman, and A. C. Gossard, "Excitation energy dependence of the exciton inner ring," *Phys. Rev. B*, vol. 85, p. 165402, 2012.

[50] M. Alloing, A. Lemaître, and F. D. E. Galopin, "Nonlinear dynamics and inner-ring photoluminescence pattern of indirect excitons," *Phys. Rev. B*, vol. 85, p. 245106, 2012.

[51] L. Smallwood, *Thermalization, Diffusion and Photoluminescence of Statistically-Degenerate Indirect Excitons in Coupled Quantum Wells.* PhD thesis, Cardiff University, 2006.

[52] L. E. Smallwood and A. L. Ivanov, "Photoluminescence and in-plane diffusion of indirect excitons," *Phys. Stat. Sol. (c)*, vol. 2, p. 3932, 2005.

[53] L. V. Butov, A. Imamoglu, A. V. Mintsev, K. L. Campman, and A. C. Gossard, "Photoluminescence kinetics of indirect excitons in GaAs/AlGaAs coupled quantum wells," *Phys. Rev. B*, vol. 59, p. 1625, 1999.

[54] M. Alloing, A. Lemaître, and F. Dubin, "Quantum signature blurred by disorder in indirect exciton gases," *Europhys. Lett.*, vol. 93, p. 17007, 2011.

[55] M. Stern, V. Garmider, V. Umansky, and I. Bar-Joseph, "Mott transition of excitons in coupled quantum wells," *Phys. Rev. Lett.*, vol. 100, p. 256402, 2008.

[56] M. Stern, V. Garmider, E. Segre, M. Rappaport, V. Umansky, Y. Levinson, and I. Bar-Joseph, "Photoluminescence ring formation in coupled quantum wells: excitonic versus ambipolar diffusion," *Phys. Rev. Lett.*, vol. 101, p. 257402, 2008.

[57] M. Stern, V. Garmider, E. Segre, M. Rappaport, V. Umansky, and I. Bar-Joseph, "Stern et al. reply:," *Phys. Rev. Lett.*, vol. 104, p. 179702, 2010.

[58] A. L. Ivanov, E. A. Muljarov, L. Mouchliadis, and R. Zimmermann, "Comment on "photoluminescence ring formation in coupled quantum wells: excitonic versus ambipolar diffusion"," *Phys. Rev. Lett.*, vol. 104, p. 179701, 2010.

[59] S. Schmitt-Rink, D. S. Chemla, and D. A. B. Miller, "Linear and nonlinear optical properties of semiconductor quantum wells," *Adv. Phys.*, vol. 38, p. 89, 1989.

[60] L. Mouchliadis, *Transport and Coherence Properties of Indirect Excitons in Coupled Quantum Wells.* PhD thesis, Cardiff University, 2008.

[61] A. L. Ivanov, P. B. Littlewood, and H. Haug, "Bose-einstein statistics in thermalization and photoluminescence of quantum-well excitons," *Phys. Rev. B*, vol. 59, p. 5032, 1999.

[62] A. V. Soroko and A. L. Ivanov, "Phonon-assisted relaxation kinetics of statistically degenerate excitons in high-quality quantum wells," *Phys. Rev. B*, vol. 65, p. 165310, 2002.

[63] A. V. Soroko, A. L. Ivanov, and L. V. Butov, "Thermalization and photoluminescence kinetics of statistically-degenerate indirect excitons in gaas/algaas coupled quantum wells," *Phys. Stat. Sol. (a)*, vol. 190, p. 719, 2002.

[64] P. Stenius and A. L. Ivanov, "Relaxation kinetics of quasi two-dimensional excitons coupled to a bath of bulk acoustic phonons," *Solid State Commun.*, vol. 108, p. 117, 1998.

[65] A. L. Ivanov, P. B. Littlewood, and H. Haug, "Bose-Einstein statistics in photoluminescence of quantum well excitons," *J. Luminescence*, vol. 87, p. 189, 2000.

[66] P. B. Littlewood, A. L. Ivanov, and H. Haug, "Photoluminescence kinetics of statistically degenerate quantum well excitons," *Phys. Stat. Sol. (a)*, vol. 178, p. 423, 2000.

[67] K. Sivalertporn, L. Mouchliadis, A. L. Ivanov, R. Philp, and E. A. Muljarov, "Direct and indirect excitons in semiconductor coupled quantum wells in an applied electric field," *Phys. Rev. B*, vol. 85, p. 045207, 2012.

[68] K. Sivalertporn, L. Mouchliadis, A. L. Ivanov, R. Philp, and E. A. Muljarov, "http://cqwexciton.cf.ac.uk."

[69] J. Crank, *The Mathematics of Diffusion*. Oxford University Press, 1980.

[70] L. V. Butov, A. L. Ivanov, A. Imamoglu, P. B. Littlewood, A. A. Shashkin, V. T. Dolgopolov, K. L. Campman, and A. C. Gossard, "Stimulated scattering of indirect excitons in coupled quantum wells: Signature of a degenerate bose-gas of excitons," *Phys. Rev. Lett.*, vol. 86, p. 5608, 2001.

[71] R. Rapaport, G. Chen, S. Simon, O. Mitrofanov, L. Pfeiffer, and P. M. Platzman, "Electrostatic traps for dipolar excitons," *Phys. Rev. B*, vol. 72, p. 075428, 2005.

[72] R. Rapaport, G. Chen, and S. Simon, "Analysis of trapped quantum degenerate dipolar excitons," *Appl. Phys. Lett.*, vol. 89, p. 152118, 2006.

[73] G. Chen, R. Rapaport, L. N. Pffeifer, K. West, P. M. Platzman, S. Simon, Z. Vörös, and D. Snoke, "Artificial trapping of a stable high-density dipolar exciton fluid," *Phys. Rev. B*, vol. 74, p. 045309, 2006.

[74] A. Gärtner, D. Schuh, A. W. Holleitner, and J. P. Kotthaus, "Loading indirect excitons into an electrostatic trap formed in coupled GaAs quantum wells," *Physica E*, vol. 40, p. 1828, 2008.

[75] V. Negoita, D. W. Snoke, and K. Eberl, "Harmonic-potential traps for indirect excitons in coupled quantum wells," *Phys. Rev. B*, vol. 60, p. 2661, 1999.

[76] V. Negoita, D. W. Snoke, and K. Eberl, "Stretching quantum wells: A method for trapping free carriers in GaAs heterostructures," *Appl. Phys. Lett.*, vol. 75, p. 2059, 1999.

[77] Z. Vörös, D. W. Snoke, L. Pfeiffer, and K. West, "Equilibration of two-dimensional excitons in an in-plane harmonic potential," *Phys. Stat. Sol. (c)*, vol. 3, p. 2461, 2006.

[78] D. W. Snoke, Y. Liua, Z. Vörös, L. Pfeiffer, and K. West, "Trapping long-lifetime excitons in a two-dimensional harmonic potential," *Solid State Comm.*, vol. 134, p. 37, 2005.

[79] A. T. Hammack, M. Griswold, L. V. Butov, L. E. Smallwood, A. L. Ivanov, and A. C. Gossard, "Trapping of cold excitons in quantum well structures with laser light," *Phys. Rev. Lett.*, vol. 96, p. 227402, 2006.

[80] M. Alloing, A. Lemaître, E. Galopin, and F. Dubin, "On-demand confinement of semiconductor excitons by all-optical control," *arXiv:*, p. 1202.3301v1, 2012.

[81] K. Kowalik-Seidl, X. P. Vögele, F. Seilmeier, D. Schuh, W. Wegscheider, A. W. Holleitner, and J. P. Kotthaus, "Forming and confining of dipolar excitons by quantizing magnetic fields," *Phys. Rev. B*, vol. 83, p. 081307(R), 2011.

[82] G. Grosso, J. Graves, A. T. Hammack, A. A. High, L. V. Butov, M. Hanson, and A. C. Gossard, "Excitonic switches operating at around 100K," *Nature. Photon.*, vol. 3, p. 577, 2009.

[83] A. A. High, A. T. Hammack, L. V. Butov, M. Hanson, and A. C. Gossard, "Exciton optoelectronic transistor," *Opt. Lett.*, vol. 32, p. 2466, 2007.

[84] Y. Y. Kuznetsova, M. Remeika, A. A. High, A. T. Hammack, L. V. Butov, M. Hanson, and A. C. Gossard, "All-optical excitonic transistor," *Opt. Lett.*, vol. 35, p. 1587, 2010.

[85] J. Rudolph, R. Hey, and P. V. Santos, "Long-range exciton transport by dynamic strain fields in a GaAs quantum well," *Phys. Rev. Lett.*, vol. 99, p. 047602, 2007.

[86] W. Hänsel, J. Reichel, P. Hommelhoff, and T. W. Hänsch, "Magnetic conveyor belt for transporting and merging trapped atomic clouds," *Phys. Rev. Lett.*, vol. 86, p. 608, 2001.

[87] S. Kuhr, W. Alt, D. Schrader, M. Müller, V. Gomer, and D. Meschede, "Deterministic delivery of a single atom," *Science*, vol. 293, p. 278, 2001.

[88] R. Rapaport, G. Chen, D. Snoke, S. H. Simon, L. Pfeiffer, K. West, Y. Liu, and S. Denev, "Mechanism of exciton emission ring pattern in doped quantum wells," *Phys. Stat. Sol. (a)*, vol. 201, p. 655, 2004.

[89] G. Chen, R. Rapaport, S. Simon, L. Pfieffer, and K. West, "Dynamics of the in-plane charge separation front in a 2d electron-hole gas," *Phys. Rev. B*, vol. 71, p. 041301, 2005.

[90] D. Snoke, S. Denev, Y. Liu, L. Pfeiffer, and K. West, "Luminescence rings and charge separation in quantum well structures," *Solid State Commun.*, vol. 127, p. 187, 2003.

[91] L. V. Butov, L. S. Levitov, A. V. Mintsev, B. D. Simons, A. C. Gossard, and D. S. Chemla, "Formation mechanism and low-temperature instability of exciton rings," *Phys. Rev. Lett.*, vol. 92, p. 117404, 2004.

[92] J. Wilkes, E. A. Muljarov, and A. L. Ivanov, "Drift-diffusion model of the fragmentation of the external ring structure in the photoluminescence pattern emitted by indirect excitons in coupled quantum wells," *Phys. Rev. Lett.*, vol. 109, p. 187402, 2012.

[93] R. Rapaport, G. Chen, D. Snoke, S. H. Simon, L. Pfeiffer, K. West, Y. Liu, and S. Denev, "Charge separation of dense two-dimensional electron-hole gases: Mechanism for exciton ring pattern formation," *Phys. Rev. Lett.*, vol. 92, p. 117405, 2004.

[94] S. Yang, A. V. Mintsev, A. T. Hammack, L. V. Butov, and A. C. Gossard, "Repulsive interaction in the macroscopically ordered exciton state," *Phys. Rev. B*, vol. 75, p. 033311, 2007.

[95] S. Yang, A. T. Hammack, M. M. Fogler, L. V. Butov, and A. C. Gossard, "Coherence length of cold exciton gases in coupled quantum wells," *Phys. Rev. Lett.*, vol. 97, p. 187402, 2006.

[96] L. S. Levitov, B. D. Simons, and L. V. Butov, "Pattern formation as a signature of quantum degeneracy in a cold exciton system," *Phys. Rev. Lett.*, vol. 94, p. 176404, 2005.

[97] A. V. Paraskevov and T. V. Khabarova, "On the microscopic theory of the exciton ring fragmentation," *Phys. Lett. A*, vol. 368, p. 151, 2007.

[98] V. I. Sugakov, "Islands of exciton condensed phases in a two-dimensional system, the distribution of their sizes and coherence in position," *Solid State Comm.*, vol. 134, p. 63, 2005.

[99] A. A. Chernyuk and V. I. Sugakov, "Ordered dissipative structures in exciton systems in semiconductor quantum wells," *Phys. Rev. B*, vol. 74, p. 085303, 2006.

[100] V. I. Sugakov, "Instabilities and self-organization phenomena in high density exciton systems," *Phase Transitions*, vol. 75, p. 953, 2002.

[101] V. I. Sugakov, "Formation of an order in a system of exciton condensed phase islands in quantum wells," *Ukr. J. Phys.*, vol. 49, p. 1117, 2004.

[102] V. I. Sugakov, "Ordered structures of exciton condensed phases in the presence of an inhomogeneous potential," *J. Phys.: Condens. Matter*, vol. 21, p. 275803, 2009.

[103] V. I. Sugakov, "Formation of inhomogeneous structures of condensed phases of excitons in quantum wells," *Phys. Rev. B*, vol. 76, p. 115303, 2007.

[104] L. Mouchliadis and A. L. Ivanov, "First-order spatial coherence of excitons in planar nanostructures: A k-filtering effect," *Phys. Rev. B*, vol. 78, p. 033306, 2008.

[105] L. Mouchliadis and A. L. Ivanov, "First-order spatial coherence of indirect excitons in coupled quantum wells," *Phys. Stat. Sol. (c)*, vol. 6, p. 524, 2009.

[106] A. V. Paraskevov and S. E. Savel'ev, "Ring-shaped luminescence patterns in a locally photoexcited electron-hole bilayer," *Phys. Rev. B*, vol. 81, p. 193403, 2010.

[107] S. Denev, S. H. Simon, and D. W. Snoke, "Luminescence ring formation in quantum wells-a model with coulomb interaction," *Solid State Commun.*, vol. 134, p. 59, 2005.

[108] M. Haque, "Ring-shaped luminescence pattern in biased quantum wells studied as a steady-state reaction front," *Phys. Rev. E*, vol. 73, p. 066207, 2006.

[109] S. Yang, L. V. Butov, L. S. Levitov, B. D. Simons, and A. C. Gossard, "Exciton front propagation in photoexcited gaas quantum wells," *Phys. Rev. B*, vol. 81, p. 115320, 2010.

[110] C. Piermarocchi, F. Tassone, V. Savona, A. Quattropani, and P. Schwendimann, "Exciton formation rates in GaAs/AlGaAs quantum wells," *Phys. Rev. B*, vol. 55, p. 1333, 1997.

[111] L. C. Andreani, "Radiative lifetime of free excitons in quantum wells," *Solid State Commun.*, vol. 77, p. 641, 1991.